Experiments on the growth and form of icicles

by

Antony Szu-Han Chen

A thesis submitted in conformity with the requirements
for the degree of Doctor of Philosophy
Graduate Department of Physics
University of Toronto

Abstract

Experiments on the growth and form of icicles

Antony Szu-Han Chen

Doctor of Philosophy

Graduate Department of Physics

University of Toronto

2014

Icicles are a ubiquitous and picturesque feature of cold winter weather. Their familiar form emerges from a subtle interplay between the solidification dynamics of ice and the gravity-driven flow of the thin water film flowing over their evolving surface. The latent heat released by freezing is advected by the water film and ultimately carried away by the surrounding sub-zero air, which is also flowing. Like many processes far from equilibrium, icicle growth can exhibit nonlinear pattern formation. While scaling theory predicts that icicles converge to 'platonic', self-similar shapes, natural icicles often exhibit regular ripple patterns about their circumference, which are due to a morphological instability. This thesis presents a comprehensive experimental study of icicles that sheds new light on the dynamics of their growth and the origin of their form.

A table-top apparatus was designed and built for the controlled growth of icicles, under different conditions of temperature, water supply rate, ambient air motion, and water purity. Image analysis and Fourier methods were used to examine their morphology. Contrary to theoretical expectations, ripples do not appear on icicles made from pure water. Instead, ripples grow and travel on icicles made from salt solutions, even at very low concentrations. The addition of non-ionic surfactant or dissolved gases does not produce ripples, unless ionic impurities are also present. The ripple wavelength is independent of time and growth conditions. The ripple amplification rate and traveling velocity vary weakly with the ionic concentration, as do the tip and radial growth speeds of the icicle. While the tip and radial growth also depend on the ambient temperature

and input mass flux, the ripple dynamics is not correlated with extrinsic conditions. If the ambient temperature or input mass flux is sufficiently low, the tip growth only advances for a short period of time before it ceases. After cessation, the shape of the icicle deviates increasingly from self-similarity. The most self-similar icicles are made from pure water with the surrounding air gently stirred, whereas icicles made from impure water in still air tend to grow multiple tips.

Acknowledgements

First and foremost, none of this would have been possible without my supervisor Stephen Morris. Not only did he pay for all the equipment and material for this project and send me to research conferences regularly, he made himself available for consultation whenever it was possible, even on weeknights and weekends. He also gave me the freedom to tread my own path and was extremely patient when I was learning from my many mistakes. I was inspired by his creativity and enthusiasm, and his seemingly endless breadth of knowledge never ceased to amaze me. It had been a privilege to work with a brilliant physicist.

Next, I would like to thank my colleagues in the Experimental Nonlinear Physics group, all of whose brains and brawn I probably borrowed at one point or another. In particular, Mike Rogers showed me the ropes during my freshman years in the group and put up with my amateur questions, even when he was busy writing his thesis, and Peter Kruse generously treated me like one of his own students during his sabbatical visit. Throughout this work, I had productive discussions with many fellow scientists, and I received thoughtful comments and suggestions from my committee members Dick Bailey and Mathew Wells.

I would also like to acknowledge: the staff of the machine shop, electronic shop, physics store, and computing services, for their technical assistance over the years; Charles Ward and his students, for sharing their expertise on surface tension measurements and being so hospitable when I worked in their lab; Qinya Liu, for her tips on Fourier analysis; Takeshi Kobayashi and Etsuko Mieda, for their translation of Japanese literature; Krystyna Biel, for being an efficient graduate student whisperer; Teresa Baptista, for helping me locate Stephen when he was undergraduate chair; the Natural Sciences and Engineering Research Council of Canada, R. Blyth, Cray Inc., and the University of Toronto, for their financial support.

Throughout my education, I was fortunate enough to have met many excellent teachers and professors, who no doubt played a role in my pursuit and completion of this project. Finally, I would like to thank my family and friends for their love and support.

Contents

List of Tables

List of Figures

Chapter 1

Introduction

Icicles are a ubiquitous feature of cold winter weather (Fig. 1.1). They are a favourite subject of photographers and science enthusiasts alike, and their complex and beautiful morphologies are familiar to everyone, at least outside the tropics. On the other hand, the unwanted build-up of ice on the surfaces of power lines and airplane wings is a serious engineering hazard [1–3]. In all cases, ice is formed when latent heat is transferred from the growing surface to the surrounding air which is below freezing, and liquid water is typically present only as a thin flowing film over the ice-water interface. The growth and emergent form of ice structures result from a subtle interplay between the solidification dynamics of ice [4–7] and the flow of the thin liquid film over its evolving surface [8].

Icicles form when cool water (e.g. melted snow) continuously drips from an overhanging support (e.g. the edge of a roof) under subfreezing ambient conditions (Fig. 1.1(a)). The basic growth mechanism of icicles, illustrated in Fig. 1.2, is well-known [9–17]. The life of an icicle begins with a single pendant drop, either completely frozen or surrounded by a thin shell of ice. An icicle can grow as long as water continues to flow over its surface. The thin water film on the icicle surface is subject to gravitational and viscous forces, as well as surface tension at the water-air interface. At the ice-water interface, the water film is presumably at its freezing point; the rest of the water film is therefore supercooled, since its temperature must decrease towards the subfreezing air. The icicle grows laterally as latent heat is removed from the ice-water interface.

The tip of the icicle consists of thin, downward-growing ice crystals, within which

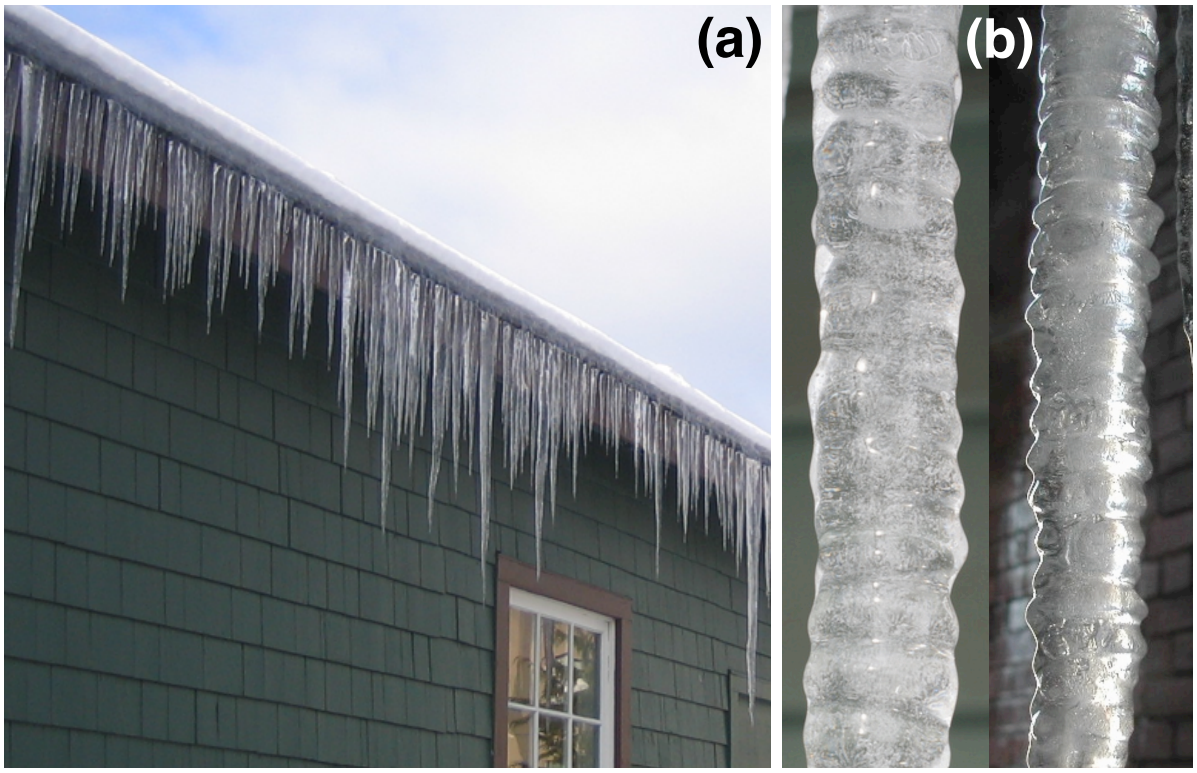

Figure 1.1: Natural icicles: (a) an array of icicles hanging from a rooftop on a cold Canadian winter day; (b) centimetre-scale ripples on the surface of two icicles.

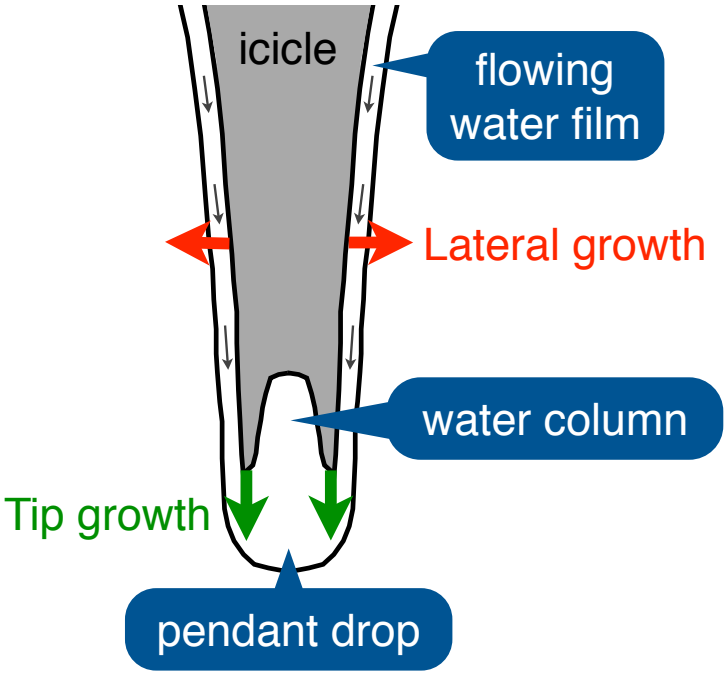

Figure 1.2: Schematic of a vertical cross-section of a growing icicle (not to scale).

incoming water can be drawn up by capillary action. This forms a narrow column of liquid water, up to a few centimetres in length, that can be held up against its weight by surface tension [12–15, 17]. The entrapped water can freeze internally; the internal ice-water interface advances downward [14] or, once the lateral growth has stopped, radially inward [13, 17]. Below this liquid core sits a pendant drop which periodically detaches from the tip. If dissolved air is present in the feed water, it comes out of solution as the water freezes, and air bubbles can be trapped within the icicle [11, 13, 15, 17]. The latent heat from the growing icicle is advected by the flowing water film and is ultimately carried away by the surrounding air, via advection-diffusion, evaporation, or radiation [18], or when the pendant drop falls off the icicle.

Besides the growth mechanism, another aspect of icicles that has been studied extensively is their crystalline structure [10, 11, 13, 19–24]. Early research, as summarized by Dorsey in Ref. [24], did not provide definitive answers to the questions of the size and orientation of icicle crystals. While Leydolt [19] and Hess [22] reported that icicles were single crystals with their c-axes, i.e. the principal axes perpendicular to their basal planes, pointing radially outward, McConnel and Kidd [21] observed that icicles consisted of many small crystals with irregular orientations. The most significant work on this subject was done by Laudise and Barns [10], who harvested about 60 natural icicles and examined their horizontal and vertical cross sections between crossed polarizers. A variation in crystal size, from less than 0.1 cm to more than 20 cm, was observed, and in no case was the c-axis found to be aligned with the icicle axis. They concluded that icicles are typically polycrystalline but may develop as single crystals if grown slowly and steadily under ideal conditions.

In spite of the well-known processes of heat and mass transport involved, there exist few quantitative models for the growth of icicles [14,16,25,26]. Makkonen [14] developed a numerical model for the radial and vertical growth of pure water icicles; he approximated the icicle as a circular cylinder and considered the heat balance at the walls and the bottom of the cylinder. Instead of this global approach, Szilder *et al.* [25] treated the icicle as a stack of infinitesimally thin cylindrical slices and studied the growth by solving the energy and mass conservation for each slice. Chung *et al.* [16] additionally included

salinity as a parameter, thus allowing for an understanding of the formation of saline water icicles. A few sets of growth experiments [13, 16, 17, 27] had been reported which verified some of the predictions in these theories. We have conducted the most extensive and carefully-controlled experimental study on the growth of distilled and saline water icicles. In this thesis, we present our data and compare it with past work.

While the models by Makkonen and Szilder *et al.* reproduced the familiar long and thin form of icicles, they did not derive an expression for the shape. Short *et al.* [26], who considered the problem from the perspective of a strict free-boundary approach, did. By coupling fluid dynamics, heat transfer in the water film and the surrounding air, and geometric principles, they derived an ordinary differential equation for the shape of an ideal, uniformly growing icicle. The solution of the ODE is distinct from a simple conical geometry; it is also parameter-free, which implies that icicles have a universal shape. Away from the tip, icicle shapes are predicted to be self-similar and follow the same asymptotic power law as that for the shape of stalactites [28, 29]. This theory had previously been compared to eight images of natural icicles whose conditions of formation were not controlled [26]. In this thesis, we perform the first direct test of the self-similarity theory under controlled laboratory conditions.

In reality, icicles often deviate in interesting ways from any ideal, self-similar shape. For example, they have been observed to bend or twist, grow thin spikes on their surface, or split near the tip [30, 31]. The most fascinating of such deviations is the formation of trains of uniform ripples around the circumference of the icicle [9, 11, 12, 16, 17, 30] (Fig. 1.1(b)). These ripples have a wavelength of around 1 cm and are visually similar in form to crenulations on stalactites [32]. They are due to a morphological instability that is not contained in any of the aforementioned growth models, but have been investigated by linear stability theory [33–39] and laboratory experiments [38, 40]. We have conducted the largest and most carefully-controlled experimental study of icicle ripples. In this thesis, we discuss our empirical results, which contradict all existing theories.

The thesis is organized as follows. Ch. 2 describes our icicle-growing apparatus and experimental methods. Ch. 3, 4, and 5 focus on the growth, shape, and ripples of icicles respectively. Ch. 6 summarizes the work and suggests future directions for this research.

Chapter 2

Experiment

2.1 Apparatus

To conduct controlled experiments on the growth and form of icicles, we designed and built a table-top icicle-making machine. A schematic and photographs of the final version are shown in Figs. 2.1 and 2.2 respectively. Icicles were grown below a sharpened support, made from a wooden dowel with a 1.25 inch diameter and suspended by stiff wires, inside a refrigerated box fixed on an optical bench. The box was made of four aluminum walls embedded with vertical copper pipes (Fig. 2.2(b)). It had dimensions of $38 \times 38 \times 107$ cm^3 and was insulated with 10 cm of commercial foam insulation (Fig. 2.2(a)). To minimize heat leak into the machine, plastic extensions were attached to the aluminum legs that held up the walls, and all gaps and holes were sealed with duct tape.

The wall temperature was controlled by a commercial bath (Neslab Digital Plus RTE-740), which circulated antifreeze through the pipes. The water supply was delivered through Tygon and copper tubing to a nozzle above the support using a peristaltic pump (Gilson Minipuls 3). A section of the copper tubing inside the machine was bundled with a much larger one in which antifreeze was circulated by a second bath (Neslab RTE-111). The temperature of the inlet nozzle was measured with a thermocouple and feedback controlled by means of a computer-controlled heater. To prevent freezing of the inlet pipe, the nozzle temperature was maintained slightly above 0 °C. The air inside the icicle-growing box was stirred by eight small computer case fans (Vantec TF8025): four

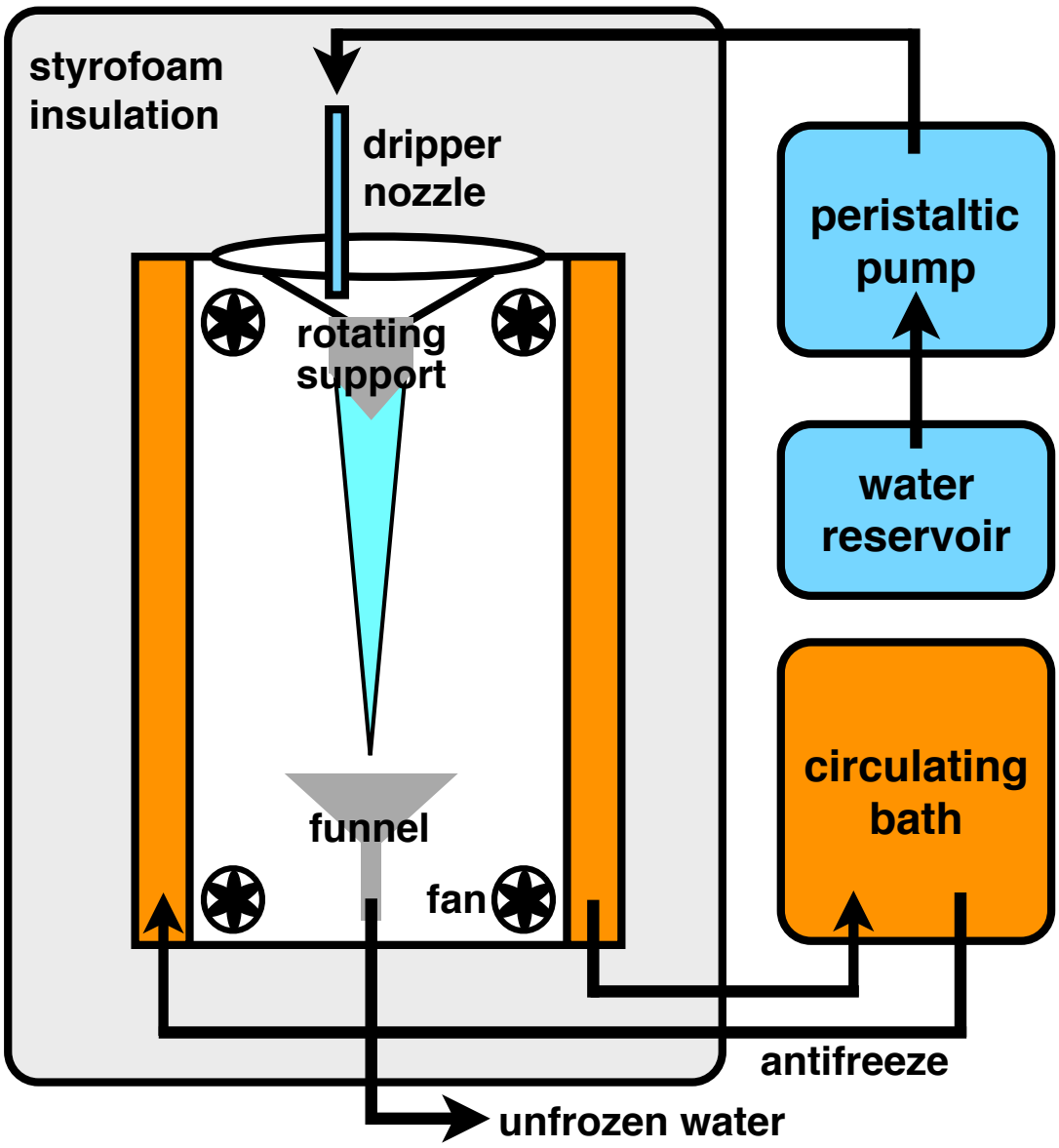

Figure 2.1: Schematic of the icicle-growing apparatus.

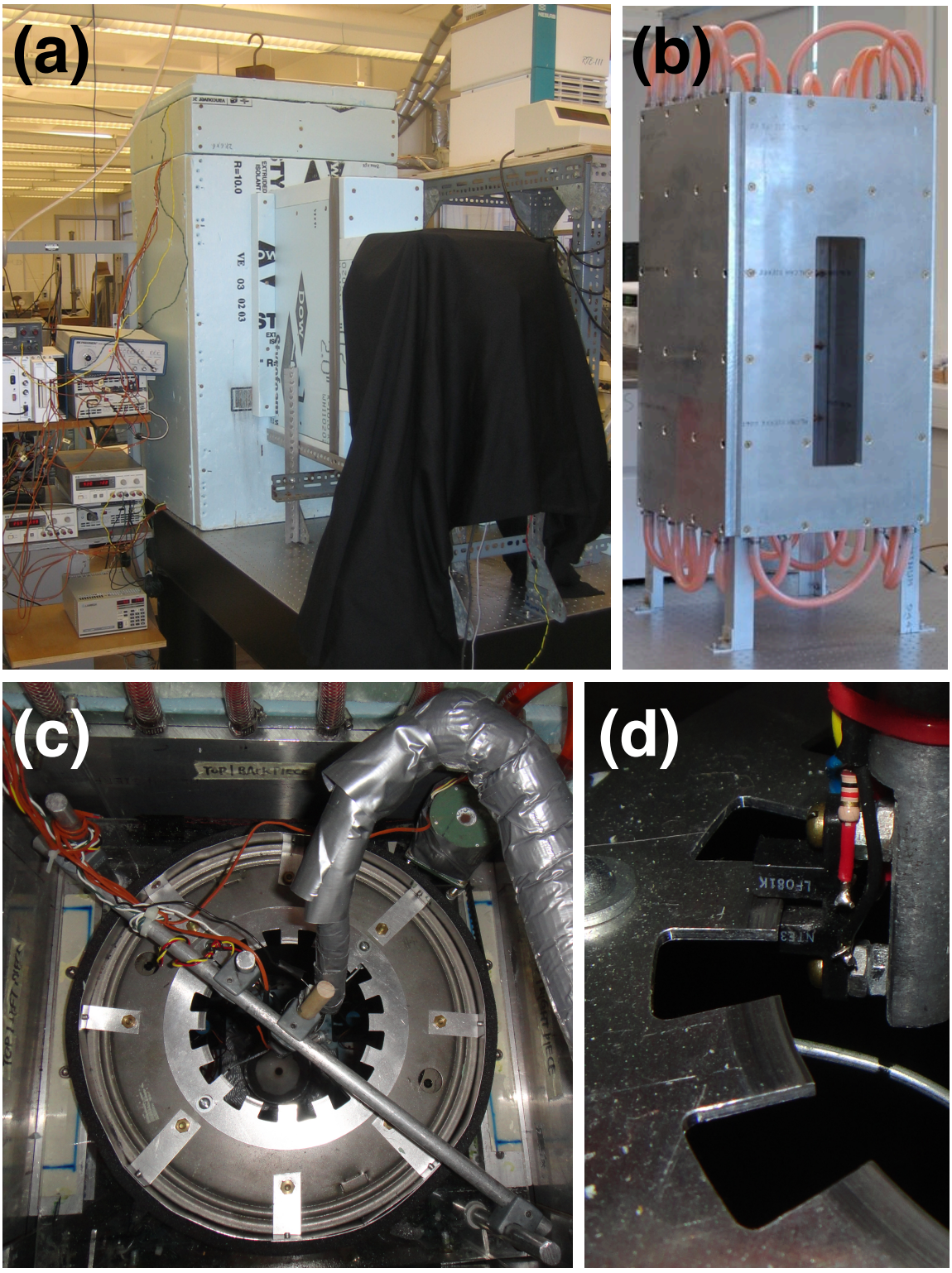

Figure 2.2: Images of the icicle-growing machine: (a) complete set-up of the apparatus; (b) aluminum cold plate walls; (c) bird's-eye view of the inside of the machine; (d) a tab passing through the photo-interrupter.

at the top corners pointed straight down, and four at the bottom corners pointed straight up. Water that dripped off the icicle was collected by an insulated warmed funnel and drained out of the machine.

The growing icicle was imaged by a computer-controlled digital single-lens reflex (DSLR) camera (Nikon D200) via a slot in the side of the box (Fig. 2.2(b)). The dimension of the slot was 63×12 cm^2. The optical path to the camera was 1.1 m and insulated with commercial foam (Fig. 2.2(a)). To avoid fogging, no windows were placed between the camera and the icicle. The icicle was illuminated by a distributed white light-emitting diode (LED) light source against a black cloth background.

Using a stepper motor, a timing belt, and a lazy susan bearing assembly (Fig. 2.2(c)), we rotated the support to encourage axisymmetry and to allow all sides of the icicle to be imaged. The nozzle was slightly off-axis from the rotating support, so the feed water could reach the entire periphery of the support over one rotation. To image reproducible views of the icicle, the rotational position of the support was indexed: tabs were machined around the inner circumference of the rotating ring, and a photo-interrupter was installed such that the camera could be triggered by LabVIEW to take a picture whenever a tab passed through its slot (Fig. 2.2(d)). We used a function generator to control the stepper motor and fixed the rotational period of the support at 4 minutes per revolution. The air motion produced by this slow rotation was negligible compared to that produced by the fans. Eight unique views of the icicle were imaged on each rotation.

2.2 Independent and dependent variables

With the experimental set-up described in Sec. 2.1, there are five parameters that can be controlled directly: the coolant temperature of the circulating bath, the rotational frequency of the peristaltic pump, the temperature along the water delivery passage, the input voltage of the fan, and the type of water supplied. These correspond to the following independent variables of our experiment: the ambient wall temperature, the mass flux of the feed water, the input water temperature, the volumetric flow of the surrounding air, and the composition or property of the feed water. In addition to taking

pictures of the icicle growth, we collected data for the following dependent variables: the temperature of the air, the relative humidity of the air, and the mass of the drip-off water.

We used LabVIEW and the National Instruments SCXI system for most of the data acquisition and control. Throughout the experiment, thermocouples were used to probe the temperatures of the wall, the inlet nozzle, and the air. Three thermocouples, with junctions located at 8 cm away from the wall and 7, 22, and 37 cm below the support, were used for the air temperature measurement. The masses of the water reservoir and the drip-off water were tracked using Ohaus electronic balances. The relative humidity in the air was monitored by an Omega RH sensor. Fig. 2.3 shows typical time-series data for these variables.

In Fig. 2.3, time zero corresponds to the start of the experiment, when the circulating bath was set to the desired temperature. To prevent icicles from forming just yet, the water supply rate was set to 6.4 g/min, and the inlet nozzle temperature was set to 20 °C. Using LabVIEW, we kept the inlet temperature at T_{set} by periodically identifying its actual value T_{actual} (Fig. 2.3(a)) and changing the voltage V applied to a power resistor attached to the nozzle accordingly (Fig. 2.3(d)): $\Delta(V^2) = \alpha \times R \times (T_{set} - T_{actual})$, where $\alpha = 0.01$ is an empirically chosen constant, and $R = 2.5\ \Omega$ is the resistance of the heater. Some time after the ambient temperature reached equilibrium (at a time of 3.7 hours for the run shown in Fig. 2.3), we refilled the water reservoir, drained the drip-off container, reset both the input mass flux and the nozzle temperature to their desired values, and initiated image acquisition.

In the remainder of this thesis, all measurements of temperature are defined to be the mean of the data during the time period in which image analysis is performed, i.e. from the initiation of icicle formation (at a time of 5.6 hours for the run shown in Fig. 2.3) to the end of the experiment. Similarly, the water supply rate is defined to be the negative of the slope of the reservoir mass time-series for this period, and the relative humidity is defined to be the midrange of the data during this period.

An Omega HHF92A digital anemometer was used to measure the volumetric air flow for various settings of the fan (Fig. 2.4(a)). Dividing the volume of the box by eight

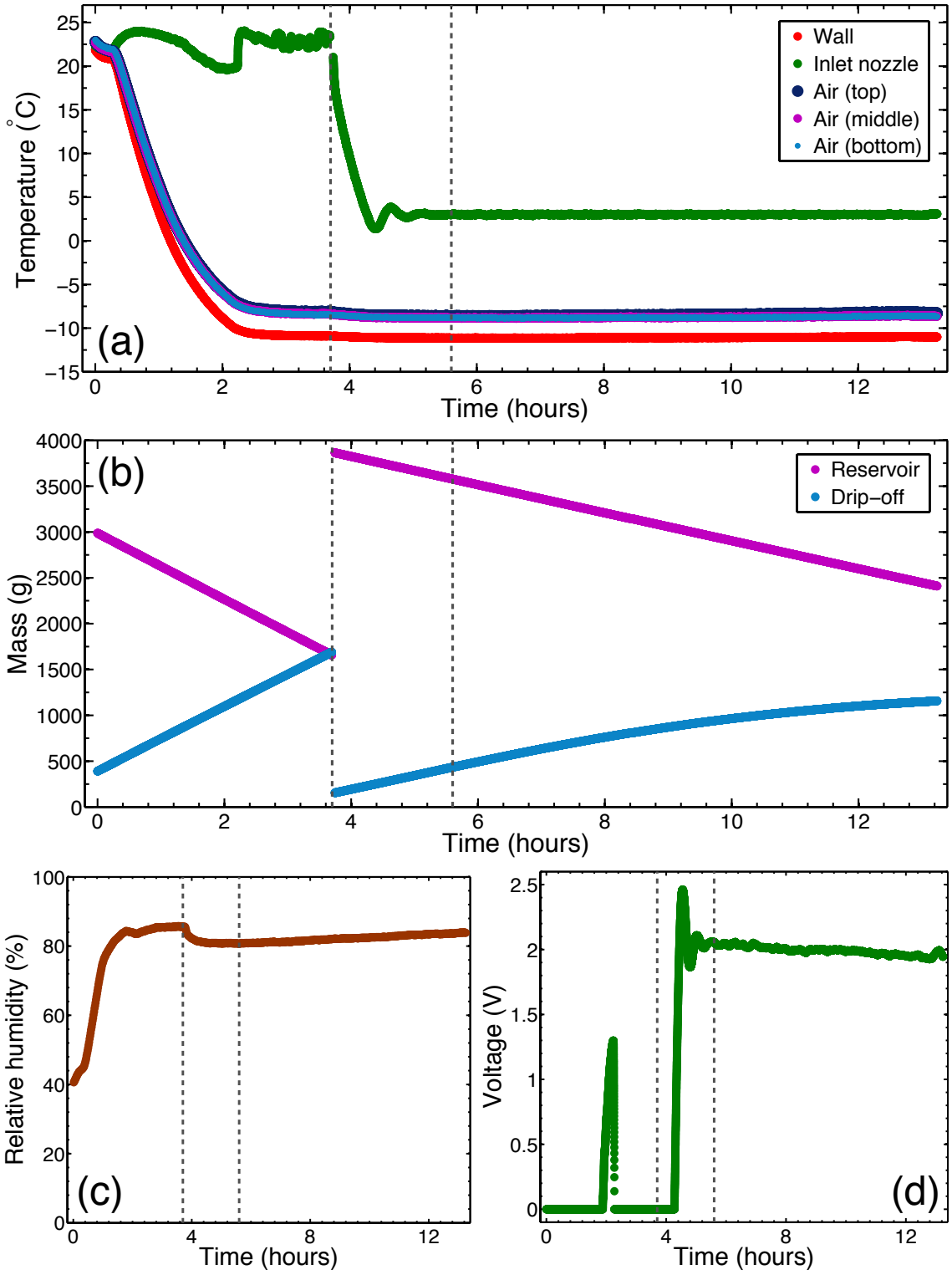

Figure 2.3: Typical time-series data for: (a) temperatures of the wall, inlet nozzle, and air; (b) masses of the containers with feed water and drip-off water; (c) relative humidity in the air; (d) voltage applied to the power resistor at the inlet nozzle. At $t = 0$, the ambient wall temperature was set to its desired value. The dashed line at $t = 3.7$ hours marks the time at which the water reservoir was refilled, the drip-off container was drained, and the input mass flux and inlet nozzle temperature were set to their desired values. The dashed line at $t = 5.6$ hours marks the initiation of icicle growth.

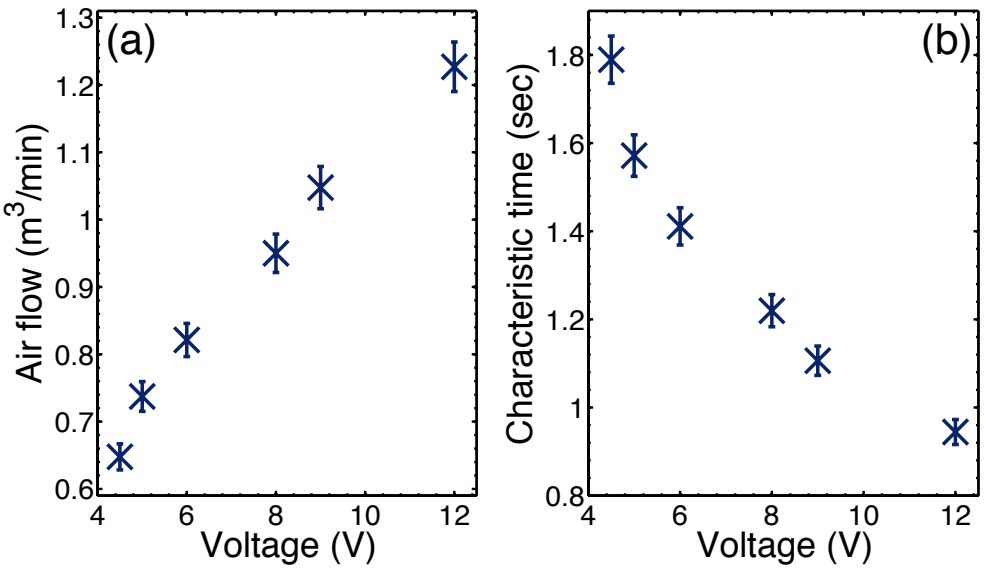

Figure 2.4: Air flow *vs.* input fan voltage: (a) volumetric air flux from each fan; (b) estimated time for all eight fans to circulate the air in the box once.

times this flux gives an estimate of the time it takes for the fans to circulate all of the air enclosed in the box once (Fig. 2.4(b)). Of course, in runs for which the fans were turned off, the forced air flow was 0. In all other cases, the air around the icicle may be regarded as well-stirred, save for a thin boundary layer near the icicle and near the walls of the box.

2.3 Water samples

Four main types of feed water were used: distilled water, Toronto tap water, salt solution, and surfactant solution. The distilled water was supplied in bulk by Canadian Springs ™. While it was much purer than tap water (Table 2.1), it was not near the limits of what purity could be achieved [41]. The salt solution was a mixture of distilled water and ACS reagent grade sodium chloride, supplied by Sigma-Aldrich. The surfactant solution was a mixture of distilled water and Triton X-100 (i.e. t-Oct-C_6H_4-$(OCH_2CH_2)_x$OH, x = 9-10), a non-ionic surfactant, also supplied by Sigma-Aldrich; it was made via dilution from a stock of 0.5 wt% Triton X-100. An Ohaus SP2001 balance was used for all mass measurements during sample preparation, except for the minute masses of added NaCl,

which was measured using a more precise Mettler AJ100 balance.

Table 2.1 shows the measured physical parameters for some of the water samples used. The conductivity and composition of the samples were analyzed by the ANALEST lab in the Department of Chemistry at the University of Toronto. Metal ion concentrations were determined by inductively coupled plasma atomic emission spectrometry, using Perkin Elmer Optima 7300DV. Anions were identified by ion chromatography, using Perkin Elmer Series 200, Alltech Eris 1000HP, Alltech 550 Conductivity Detector, and Phenomenex Star Ion 300 Column. Conductivities were measured using an Alltech 550 Conductivity Detector.

We measured the surface tension of distilled water, tap water, and surfactant solutions using the capillary tube method at room temperature. A glass capillary tube was immersed into each sample, and a cathetometer was used to identify the rise of the meniscus in the tube. The capillary rise is given by $\Delta h = 2\gamma/(\rho g r)$, where γ is the liquid-air surface tension, ρ is the liquid density, g is the acceleration due to gravity, and r is the inner radius of the capillary [42]; the contact angle between the liquid surface and the glass surface is assumed to be $0°$. Since g and r are both constant, we can estimate the surface tension of surfactant solutions by comparing the product $\rho \times \Delta h$ with that for distilled water.

As expected, the surface tension of distilled water is reduced with the addition of Triton X-100 (Fig. 2.5(a)). However, while our results follow the same trend as those obtained using the Wilhelmy plate [43, 44] and de Noüy ring [45] methods, there is a discrepancy between them (Fig. 2.5(a)). We attribute this discrepancy to adsorption effects in the capillary tube measurements: as surfactant molecules stick to the inner glass surface, the solution behaves as if it had a lower surfactant concentration. As will be seen in Ch. 5, this discrepancy does not affect the conclusions of our study. Fig. 2.5(b) shows the surface tension of salt solutions, calculated using Ref. [46]; it increases very weakly with NaCl concentration over the range used in our experiments.

The apparatus, methods, and samples discussed in this chapter serve as the basis for the experimental results presented in the next three chapters.

Sample	**Main impurities**	**Concentration**	**Conductivity**	**Surface tension**
Distilled water	Ca^{+2} K^{+} Na^{+} Ba^{+2}	0.037 mg/L 0.026 mg/L 0.014 mg/L 0.003 mg/L	2 μS/cm	0.072 N/m
Surfactant solution (0.02 wt%)	Triton X-100	200 mg/L	1.7 μS/cm	See Fig. 2.5(a)
Salt solution (0.008 wt%)	NaCl	80.0 mg/L	211 μS/cm	See Fig. 2.5(b)
Toronto tap water	Ca^{+2} Na^{+} Mg^{+2} K^{+} Si^{+2} Cu^{+2} SO_4^{-2} Cl^{-} NO_3^{-} F^{-} Zn^{+2}, V^{+2}, Ni^{+2}, Ba^{+2}, Fe^{+2}, Mn^{+2}	37.5 mg/L 10.7 mg/L 8.82 mg/L 1.66 mg/L 1.22 mg/L 0.46 mg/L 31.60 mg/L 25.11 mg/L 0.96 mg/L 0.41 mg/L < 0.2 mg/L	419 μS/cm	0.071 N/m

Table 2.1: Measured compositions, conductivities, and surface tension of selected water samples. The conductivities were measured at 35 °C.

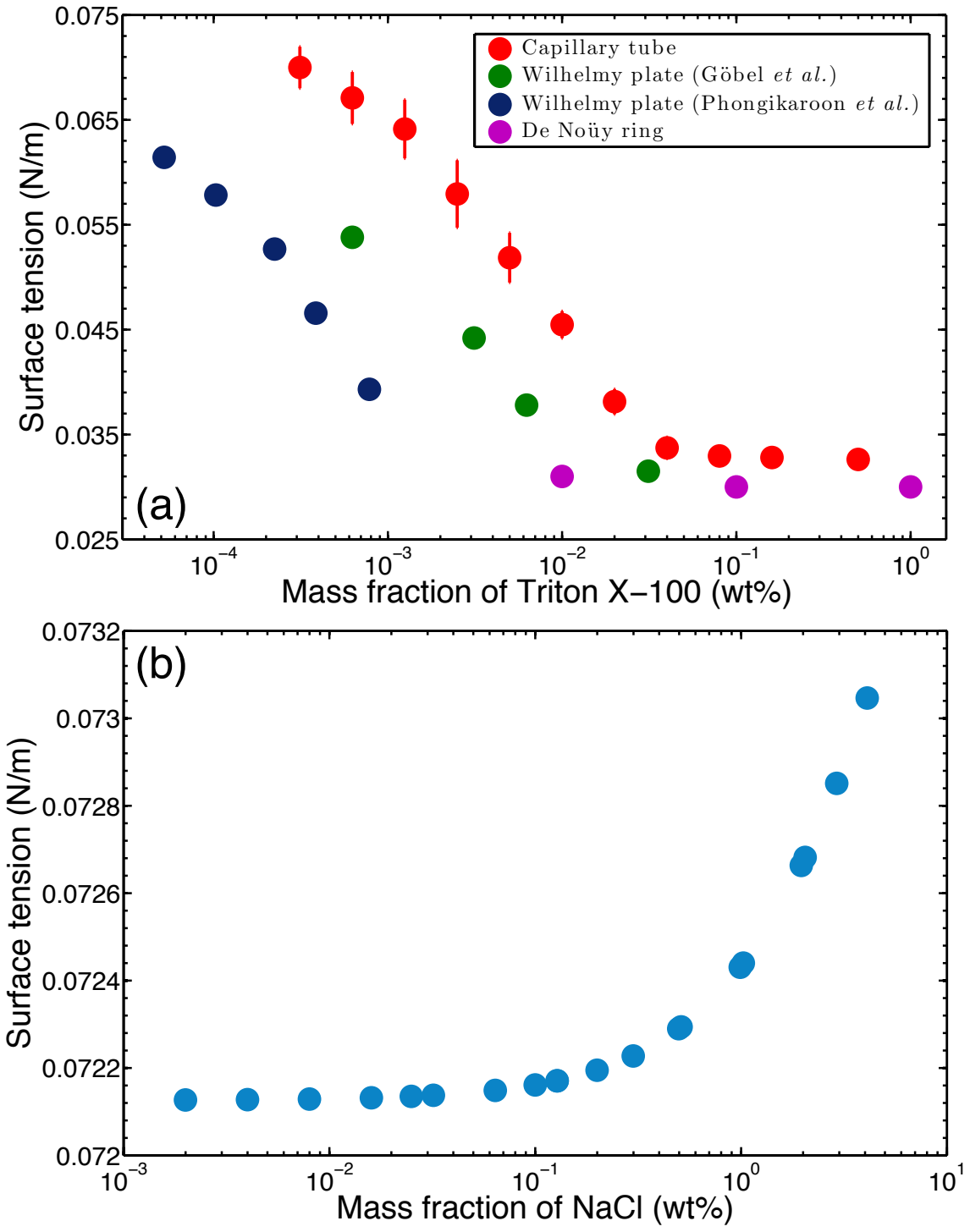

Figure 2.5: Surface tension *vs.* concentration for (a) Triton X-100 and (b) NaCl. In (a): the data using the capillary tube method is ours; the data using the Wilhelmy plate method is from Refs. [43] (Göbel *et al.*) and [44] (Phongikaroon *et al.*); the data using the de Noüy ring method is from Ref. [45]. The data in (b) is from Ref. [46]. All measurements were made at 25 ± 1 °C.

Chapter 3

Growth and cessation

In Ch. 1, the growth mechanism of icicles, which has been widely investigated [9–17], was described. However, there exist few quantitative models for the evolution of icicles [14,16, 25,26], and the few sets of reported laboratory experiments on icicle growth [13,16,17,27] were limited in their traversal of parameter space. Using the apparatus and methods described in Ch. 2, we have conducted an extensive, carefully-controlled experimental study on icicle growth. The primary objective of this chapter is to present our data on how the icicle length, radius, and mass evolve in time and depend on the various independent variables. A secondary goal of this chapter is to introduce a number of physical quantities that are relevant to icicle formation – these are also collected in Appendix A, and some will become important in later chapters.

This chapter begins with theoretical treatments of the thin water film flowing down the icicle surface (Sec. 3.1) and the heat transfer mechanisms that lead to its growth (Sec. 3.2). We then describe our edge detection algorithm, show time-series data for the length and radius of lab-grown icicles, and compare their growth rates under varying conditions (Sec. 3.3). Next, we determine the fraction of feed water that is consumed to form the icicle, as well as the relative importance of the different heat transfer mechanisms to the freezing (Sec. 3.4). We then investigate how icicle growth is affected by the addition of salt to the water source and present results on saline water icicles (Sec. 3.5). Finally, we consider the regime of icicle evolution in which the length no longer increases (Sec. 3.6); in this thesis, the discontinuation of tip growth is referred to as 'cessation.'

3.1 Thin-film flow

In this section, we consider the flow of the thin water film on the surface of an icicle [8,26]. Since the water film thickness is much smaller than the typical icicle radius, the ice-water interface can be approximated as a flat surface. Since the water film flow is much faster than the radial growth of icicles, the consumption of water from the thin film to make ice can be neglected.

The flow $\vec{u} = [u, v, w]$ of an incompressible Newtonian fluid of density ρ and kinematic viscosity ν is governed by the Navier-Stokes equations:

$$\frac{D\vec{u}}{Dt} = \frac{\partial \vec{u}}{\partial t} + (\vec{u} \cdot \nabla)\vec{u} = -\frac{1}{\rho}\nabla P + \nu \nabla^2 \vec{u} + \vec{g}, \tag{3.1}$$

$$\nabla \cdot \vec{u} = 0, \tag{3.2}$$

where t is time, P is pressure, and $\vec{g}$ is the acceleration due to gravity.

Using the coordinate system shown in Fig. 3.1, and assuming a steady flow solution $\vec{u} = [u(y), v(y), 0]$, Eq. 3.2 indicates that $\partial v/\partial y = 0$, i.e. v is constant. The no-slip condition implies $v = 0$ at $y = 0$, so $v = 0$ everywhere, i.e. $\vec{u} = [u(y), 0, 0]$. Substituting this into Eq. 3.1 gives:

$$0 = -\frac{1}{\rho}\frac{\partial P}{\partial x} + \nu \frac{d^2 u}{dy^2} + g\cos\theta, \tag{3.3}$$

$$0 = -\frac{1}{\rho}\frac{\partial P}{\partial y} + g\sin\theta. \tag{3.4}$$

Integrating Eq. 3.4 gives $P = \rho g y \sin\theta + f(x)$. At the free surface, y is equal to the water film thickness h, P is equal to the atmospheric pressure P_0, so $f(x) = P_0 - \rho g h \sin\theta$ and $P = P_0 + \rho g(y - h)\sin\theta$. Since P is independent of x, Eq. 3.3 becomes

$$\frac{d^2 u}{dy^2} = -\frac{g}{\nu}\cos\theta. \tag{3.5}$$

Integrating Eq. 3.5 twice and enforcing no-slip and stress-free boundary conditions at the ice-water and water-air interfaces respectively, i.e. $u = 0$ at $y = 0$ and $\nu du/dy = 0$ at

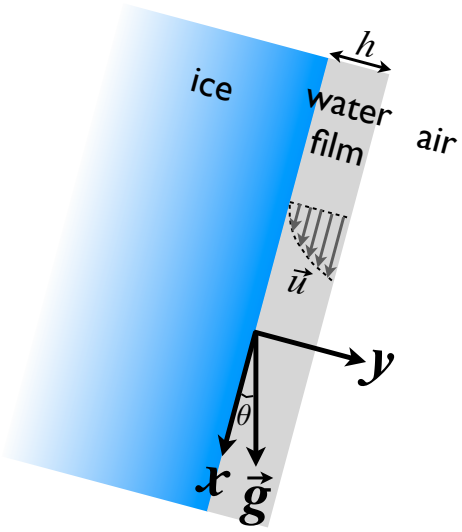

Figure 3.1: Coordinate system for thin-film calculations. This figure is exaggerated and not to scale; in particular, θ is close to 0 along most of the icicle.

$y = h$, we find a parabolic flow profile

$$u(y) = \frac{g}{2\nu} y(2h - y)\cos\theta. \tag{3.6}$$

If a cylindrical icicle has a radius R and the volumetric flow rate of its feed water is Q_0, then

$$\frac{Q_0}{2\pi R} = \int_0^h u dy = \frac{gh^3}{3\nu}\cos\theta. \tag{3.7}$$

Therefore, the thickness of the water film is given by

$$h = \left(\frac{3Q_0\nu}{2\pi g R\cos\theta}\right)^{1/3}. \tag{3.8}$$

We can also calculate the surface speed of the water film using Eq. 3.6:

$$u_s = u(y = h) = \frac{gh^2}{2\nu}\cos\theta. \tag{3.9}$$

While these give good estimates near the root (i.e. top) of the icicle, their validity diminishes towards the tip, where a pendant drop detaches periodically and the steady flow assumption is certainly violated. As the water flows down the icicle, some converts

into ice and some may evaporate, so the volumetric flux deviates further away from its input value Q_0.

3.2 Heat transfer

In this section, we consider the heat transfer at the tip and the walls of the icicle [4,14,25], which leads to its growth in length and radius respectively. Internal freezing of the icicle is not considered here. The heat balance at the surface of the pendant drop at the icicle tip is given by

$$J_C^T + J_F^T = J_{AD}^T + J_E^T + J_R^T, \tag{3.10}$$

where J_C^T is the heat flux associated with the cooling of the pendant drop before it falls off, and J_F^T is the flux of latent heat from the tip growth. The three terms on the right hand side are the heat flux due to advection-diffusion, evaporation, and thermal radiation at the tip. Similarly, the total heat flux associated with the lateral growth is given by

$$J_F = J_{AD} + J_E + J_R. \tag{3.11}$$

The subscripts in Eq. 3.11 have the same meanings as in Eq. 3.10. Here, since the water film is so thin, the temperature change across the film is assumed to be negligible, i.e. the heat flux through the ice-water interface is assumed to be the same as the heat flux through the water-air interface.

In Makkonen's model of icicle growth [14], the terms in Eq. 3.10 for tip growth are parameterized as follows:

$$J_{AD}^T = H^T \Delta T_A, \tag{3.12}$$

$$J_E^T = H_v^T \Delta \rho_v, \tag{3.13}$$

$$J_R^T = \sigma_B (T_{LA}^4 - T_A^4), \tag{3.14}$$

$$J_C^T = W_T c_L \Delta T_p / A_p, \tag{3.15}$$

$$J_F^T = L_f (dM_T/dt)/A_p, \tag{3.16}$$

where H^T is the convective heat transfer coefficient for the tip, ΔT_A is the difference between the temperature at the water-air interface T_{LA} and the ambient air temperature T_A, H_v^T is the evaporative heat transfer coefficient for the tip, $\Delta\rho_v$ is the difference between the water vapour densities at the water-air interface and in the air, σ_B is the Stefan-Boltzmann constant, W_T is the mass flux of water arriving at the tip, c_L is the specific heat of water, ΔT_p is the temperature change of the pendant drop from its formation to its detachment, A_p is the surface area of the pendant drop, L_f is the latent heat of fusion of water, and dM_T/dt is the mass growth rate of ice at the tip.

For the lateral growth, Makkonen [14] parameterized the terms in Eq. 3.11 as follows:

$$J_{AD} = H\Delta T_A, \tag{3.17}$$

$$J_E = H_v\Delta\rho_v, \tag{3.18}$$

$$J_R = \sigma_B(T_{LA}^4 - T_A^4), \tag{3.19}$$

$$J_F = L_f(1 - f_L)(dM/dt)/A_w, \tag{3.20}$$

where H and H_v are the convective and evaporative heat transfer coefficients for the walls, f_L is the liquid fraction of the growing ice surface, dM/dt is the mass growth rate of ice at the walls, and A_w is the surface area of the walls. An ice surface growing under a supercooled water film can do so dendritically, and some of the water can be trapped in the dendritic ice matrix [14, 47]; the $(1 - f_L)$ factor in Eq. 3.20 accounts for this "spongy ice" formation. Makkonen recently showed that f_L is a material parameter [48].

The convective heat transfer coefficients H^T and H can be written in terms of the Nusselt number Nu and the thermal conductivity of air Λ_A [4, 14]. Based on engineering data, the Nusselt number can be written as a phenomenological function of the Grashof number Gr for free convection [14, 49, 50], or of the Reynolds number Re for forced convection [4, 14, 51]. Gr involves the kinematic viscosity of air ν_A; Re depends on not only ν_A but also the wind speed u_A (see Table A.2).

Following Neufeld *et al.* [18], we use a simple scaling to relate the evaporative and

convective heat transfer coefficients:

$$H_v^T = (L_v/\rho_A c_A)H^T, \tag{3.21}$$

$$H_v = (L_v/\rho_A c_A)H, \tag{3.22}$$

where L_v is the latent heat of vaporization of water, ρ_A is the density of air, and c_A is the specific heat of air. Assuming vapour is saturated at the water-air interface:

$$\Delta\rho_v = \rho_{\text{sat}}(T_{LA}) - \mathcal{R}_{\mathcal{H}}\rho_{\text{sat}}(T_A); \tag{3.23}$$

$$\rho_{\text{sat}}(T) = \rho_{\text{sat}}(T_m)\frac{T_m}{T}\exp\left[-\frac{\mathcal{M}_L L_v}{\mathcal{R}}\left(\frac{1}{T} - \frac{1}{T_m}\right)\right]; \tag{3.24}$$

ρ_{sat} is the saturated vapour density, $\mathcal{R}_{\mathcal{H}}$ is the relative humidity, $T_m = 0\ ^\circ\text{C}$ is the freezing point of water, $\mathcal{M}_L$ is the molar mass of water, and $\mathcal{R}$ is the gas constant.

Makkonen [14] approximated the pendant drop as a hemisphere with radius R_p and formulated the remaining parameters associated with tip growth as follows:

$$W_T = W_0 - \frac{dM}{dt} - \frac{J_E A_w}{L_v}, \tag{3.25}$$

$$\Delta T_p = -\left(\frac{1}{0.16}\frac{dR}{dt}\right)^{\frac{1}{1.7}} + \left(\frac{1}{0.16}\frac{dL}{dt}\right)^{\frac{1}{1.7}}, \tag{3.26}$$

$$A_p = 2\pi R_p^2, \tag{3.27}$$

$$dM_T = \rho_I \cdot dV_T = \rho_I 2\pi R_p \delta_T \cdot dL, \tag{3.28}$$

where W_0 is the mass flux of water to the root, L and R are the length and radius of the icicle, ρ_I is the density of ice, V_T is the volume of ice grown at the tip, and δ_T is the thickness of the downward growing ice crystals at the tip. As described by Eq. 3.25, the mass flux decreases from the root to the tip as water freezes and evaporates along the walls. In Eq. 3.26, the temperature change of the pendant drop is given by the temperature of the water arriving at the tip subtracted by the mean temperature of the pendant drop. Makkonen approximated both of these using an empirical relationship

between the speed of ice growth and supercooling found by Hillig *et al.* [52]; each term has a unit of °C, and dR/dt and dL/dt are in cm/sec. Using the above expressions for A_p and dM_T, we can write Eq. 3.16 as:

$$J_F^T = \rho_I L_f \frac{\delta_T}{R_p} \frac{dL}{dt}. \tag{3.29}$$

To study the lateral growth, we shall depart from Makkonen's global approach of forcing a cylindrical form onto the icicle [14]. Instead, we use a local approach by considering thin horizontal slices of the icicle, à la Szilder *et al.* [25]:

$$dM_{\text{slice}} = \tilde{\rho_I} \cdot dV_{\text{slice}} = \tilde{\rho_I} \cdot dL \cdot d(\pi R^2) = \tilde{\rho_I} 2\pi R \cdot dL \cdot dR, \tag{3.30}$$

$$dA_{\text{slice}} = 2\pi R \cdot dL, \tag{3.31}$$

where $\tilde{\rho_I} = f_L \rho_L + (1 - f_L)\rho_I$, ρ_L is the density of water, and V_{slice} is the volume of ice grown on the walls of the slice. Replacing dM with dM_{slice} and A_w with dA_{slice}, Eq. 3.20 becomes:

$$J_F = \tilde{\rho_I} L_f (1 - f_L) \frac{dR}{dt}. \tag{3.32}$$

The analytical model presented here, which we have adapted from Refs. [14, 18, 25], will be used in Secs. 3.4 and 3.5 to estimate the relative importance of the various heat transfer mechanisms to the growth of our laboratory icicles.

3.3 Tip and lateral growth

In this section, we present experimental data for the tip and lateral growth of distilled water icicles. As mentioned in Ch. 2, high-resolution digital images were taken during the experiment. To analyze them, we first cropped each image to keep only the icicle; the top of the crop window was chosen to be at the bottom of the wooden dowel from which the icicle was grown. Next, we used MATLAB's Sobel algorithm to detect the edge of the icicle. The edge data $x(y)$ from each image was then transformed into a profile $R(z)$, where z was defined as the vertical distance away from the tip, and the radius R was

taken to be half the distance between the left and right edges of the icicle. Fig. 3.2 shows an example of this procedure being applied to a typical image.

To convert pixels into centimetres, we took a picture of a meterstick placed below the dowel, then we calculated a conversion factor by comparing the physical scale on the meterstick with the number of image pixels across that same length. The conversion factor varied slightly for different runs; it was on average 0.018 ± 0.001 cm/pixel, so a 36 cm icicle was about 2000 pixels long.

Fig. 3.3 shows time-series data, averaged over each rotation, for the length and radius of a representative sample of icicles grown under different conditions of ambient wall temperature and water supply rate. In both plots, time zero corresponds to the initiation of icicle growth. Here, the radius R_0 is always taken at the same height: 5 cm below the root of the icicle, i.e. $R_0 = R(L - 5 \text{ cm})$. More precisely, R_0 is the mean of the radius measurements between $z = L - 4.5$ cm and $z = L - 5.5$ cm. Radii at other parts of the icicle will be investigated in Sec. 3.6, while R along the entire length of the icicle will be treated in Ch. 4. In general, the time evolution of icicles can be split into two regimes: pre- and post-cessation. In the pre-cessation regime, the length of the icicle increases with time, and pendant drops are observed to continually drip off its tip. After icicle growth ceases at the tip, water is no longer observed to drip off the icicle.

To compare icicle growth under different conditions, we calculated a tip growth speed and a lateral growth speed for each run. To obtain the former, we performed a linear fit to $L(t)$ and extracted the slope of the best-fit line. For runs in which cessation occurred, the post-cessation data was excluded from the analysis. Similarly, we fit a line to the rising $R_0(t)$ data over the first 2 hours and defined the radial growth speed as its slope. These speeds are plotted in Figs. 3.4 and 3.5 against 4 independent variables: ambient wall temperature, water supply rate, input water temperature, and surrounding air flux due to each fan. The 4 panels within each figure have the same range on the vertical axis. In cases where multiple experiments were conducted under the same conditions, the averaged result is presented.

In general, the growth rates of the icicle length and radius both increase with decreasing ambient temperature (Figs. 3.4(a) and 3.5(a)). On the other hand, as the input mass

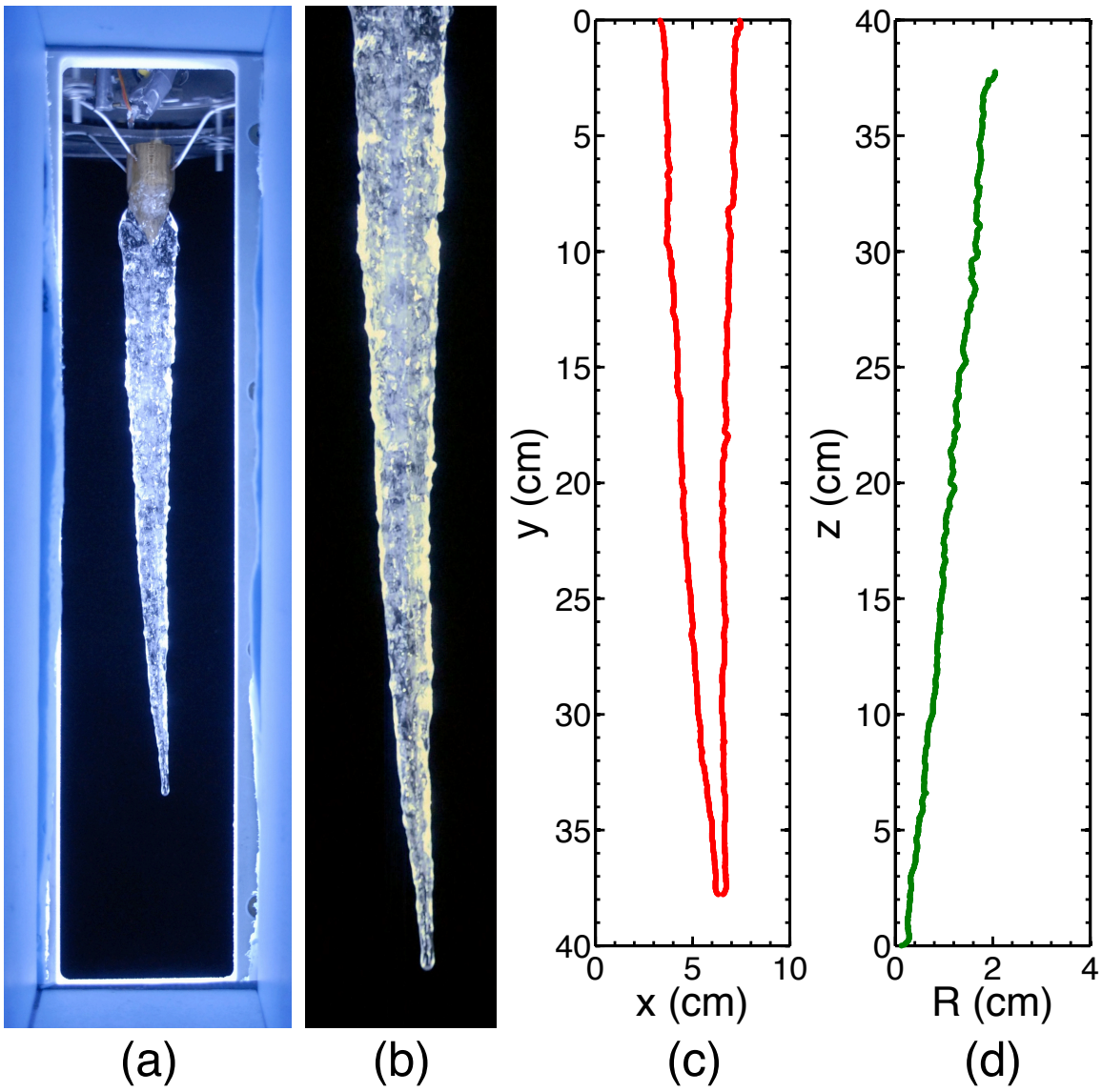

Figure 3.2: Application of the edge detection algorithm: (a) original image; (b) cropped image; (c) detected left and right edges $x(y)$; (d) icicle profile $R(z)$.

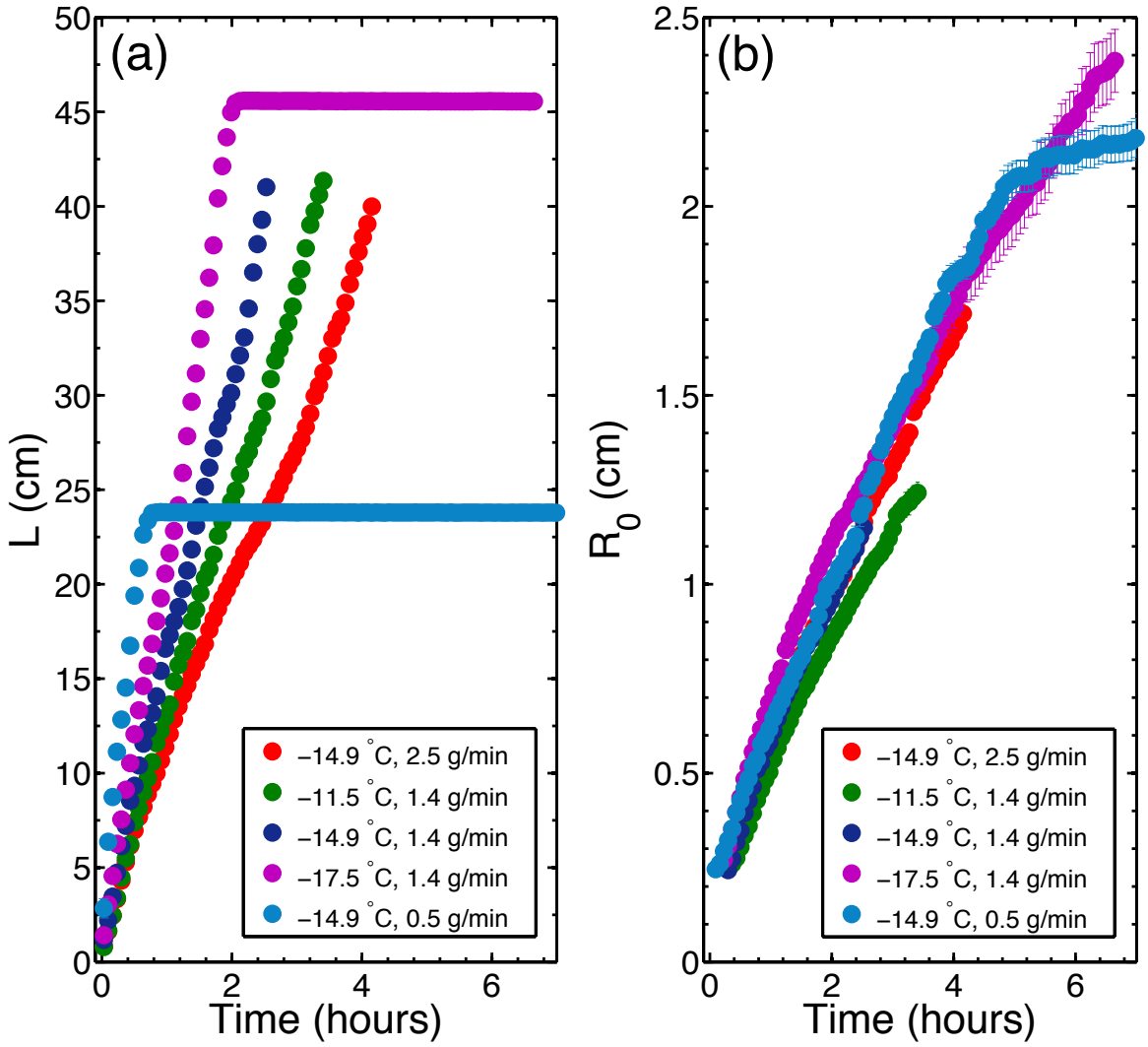

Figure 3.3: Time evolution of the (a) length and (b) radius of some distilled water icicles. The colour-coded circles in the two panels correspond to the same set of experiments. The legends show the ambient wall temperature and the water supply rate for each run. In all experiments, the input water temperature was 3.0 °C, and the surrounding air flux due to each fan was 0.95 m^3/min. The error bars indicate the standard errors from averaging over each rotation.

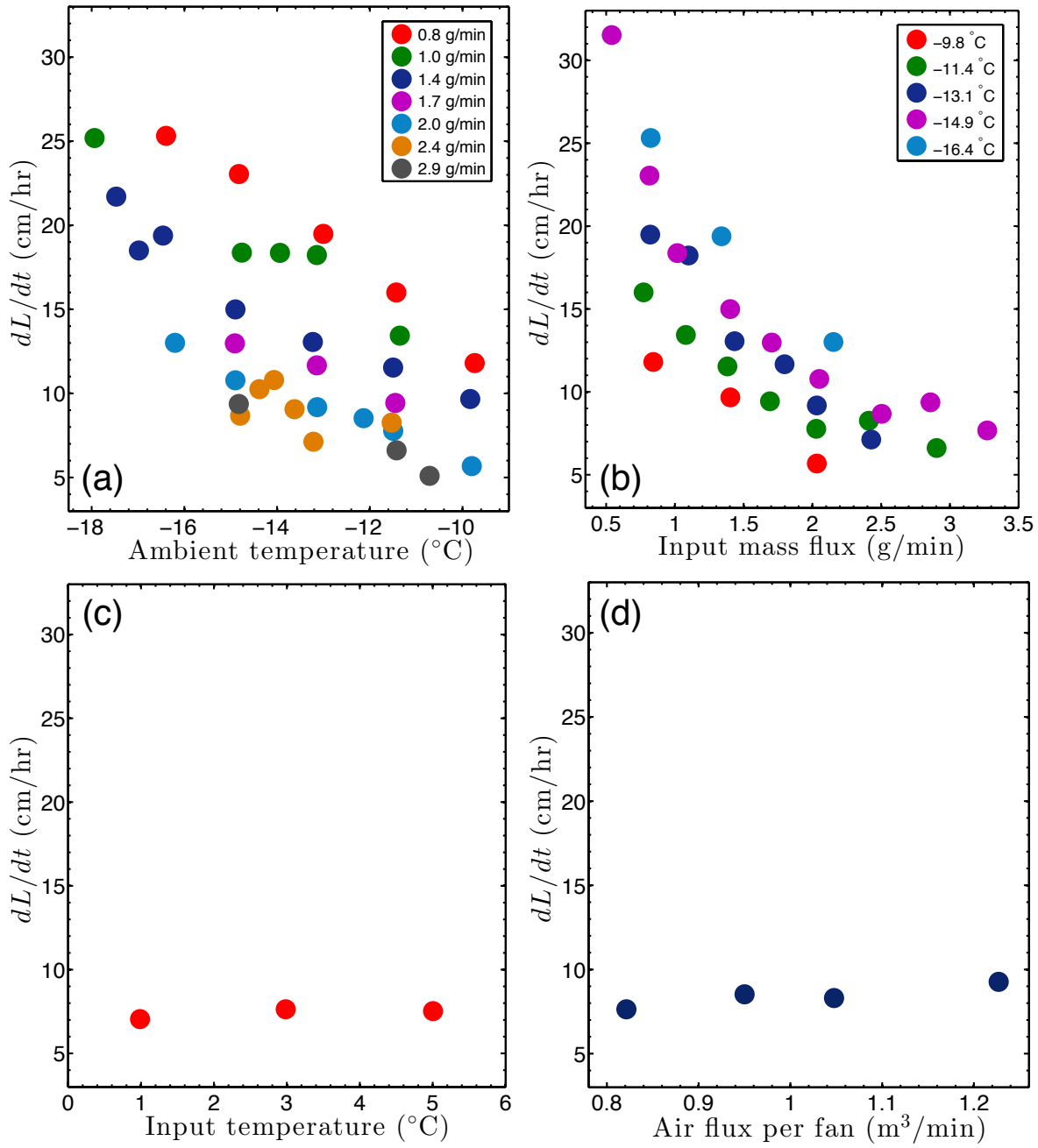

Figure 3.4: Tip growth speeds of distilled water icicles *vs.* extrinsic conditions. The fixed variables in each panel are: (a) water supply rate (as shown in the legend), input water temperature (3.0 °C for all experiments), and air flux per fan (0.95 m^3/min for all experiments); (b) ambient wall temperature (as shown in the legend), input water temperature (3.0 °C for all experiments), and air flux per fan (0.95 m^3/min for all experiments); (c) ambient wall temperature (−12.1 °C for all experiments), water supply rate (2.0 g/min for all experiments), and air flux per fan (0.82 m^3/min for all experiments); (d) ambient wall temperature (−12.1 °C for all experiments), water supply rate (2.0 g/min for all experiments), and input water temperature (3.0 °C for all experiments). Each colour corresponds to one set of experiments with the same values of the fixed variables.

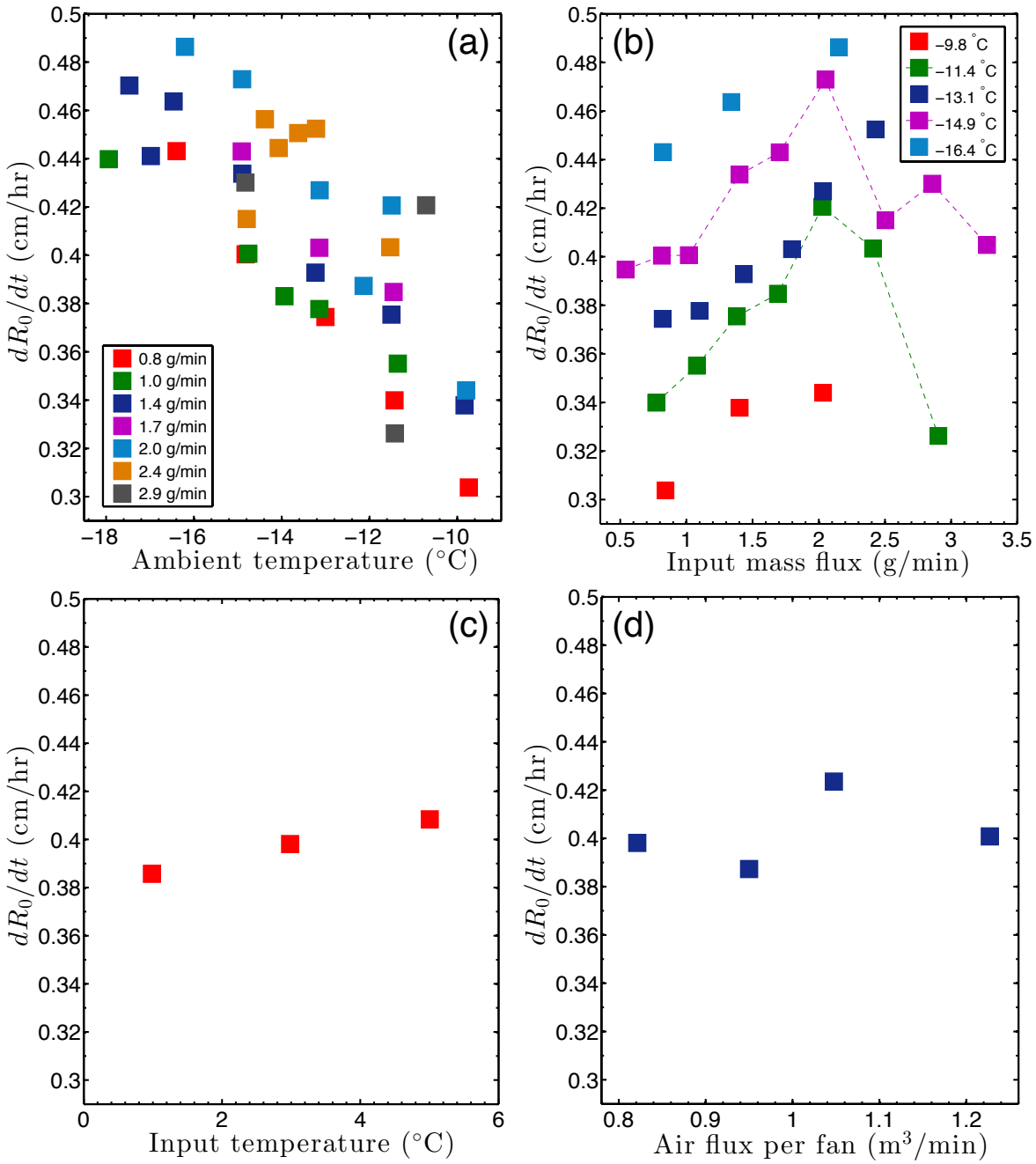

Figure 3.5: Radial growth speeds of distilled water icicles *vs.* extrinsic conditions. The fixed variables in each panel are: (a) water supply rate (as shown in the legend), input water temperature (3.0 °C for all experiments), and air flux per fan (0.95 m^3/min for all experiments); (b) ambient wall temperature (as shown in the legend), input water temperature (3.0 °C for all experiments), and air flux per fan (0.95 m^3/min for all experiments); (c) ambient wall temperature (−12.1 °C for all experiments), water supply rate (2.0 g/min for all experiments), and air flux per fan (0.82 m^3/min for all experiments); (d) ambient wall temperature (−12.1 °C for all experiments), water supply rate (2.0 g/min for all experiments), and input water temperature (3.0 °C for all experiments). Each colour corresponds to one set of experiments with the same values of the fixed variables.

flux is increased, the tip growth speed decreases (Fig. 3.4(b)), while the lateral growth speed increases (Fig. 3.5(b)). However, not all of these trends are observed for high water supply rates exceeding 2.0 g/min; in particular, the lateral growth speed decreases with increasing input mass flux in this domain (Fig. 3.5(b)). All of these correlations are in agreement with the model of Makkonen [14] and the experiments by Maeno *et al.* [13,17], except Makkonen found that the lateral growth speed is "only slightly affected" by input mass flux, and Maeno *et al.*, who tried various water supply rates between 0.2 and 1.8 g/min, concluded the lateral growth speed "maintains almost similar values." Finally, we find that the correlations of both growth speeds with input water temperature and surrounding air flux are much less significant than those with ambient temperature and input mass flux, at least in the parameter space that we explored (Figs. 3.4(c)-(d) and 3.5(c)-(d)).

3.4 Mass of water consumption

There are two objectives to this section. The first is to determine how much of the feed water freezes to form the icicle and how this percentage changes with time. The second is to compute the heat transfer coefficients at the tip and at the sides of the icicle; doing so will allow us to compare the contributions of the different heat transfer mechanisms that lead to its growth.

To begin, we plot time-series data for the mass of a representative sample of icicles and the cumulative mass of their drip-off water (Fig. 3.6). It is possible to do this, because we recorded the masses of the water reservoir and the drip-off container during the experiment. In both plots, time zero corresponds to the initiation of icicle growth, and the data has been averaged over every 4 minutes. The total mass of the water supplied M_S is set to 0 at $t = 0$ and increases linearly with time, since the input mass flux $W_0 = dM_S/dt$ is fixed during each experiment. The total mass of the drip-off water M_D is set to 0 at $t = 0$ and increases with time during icicle growth (Fig. 3.6(b)). The icicle mass M_I at each time is calculated by subtracting M_S by M_D; the small amount of water lost due to evaporation is not taken into account here. Obviously, M_I increases

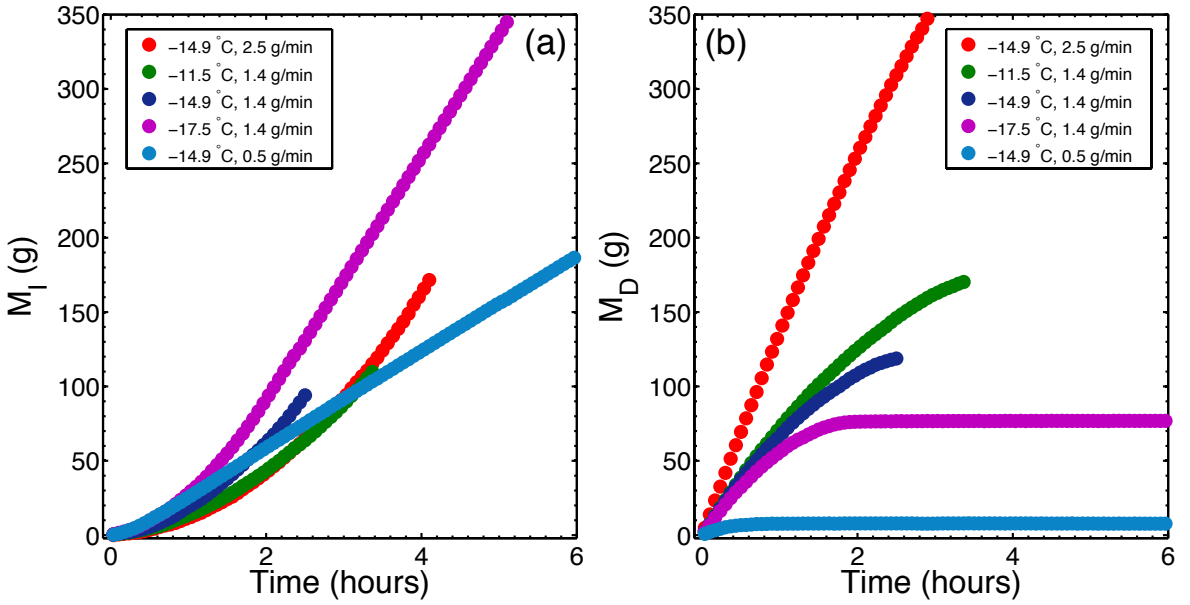

Figure 3.6: Time evolution of the mass of (a) some distilled water icicles and (b) their drip-off. The colour-coded circles in the two panels correspond to the same set of experiments. The legends show the ambient wall temperature and the water supply rate for each run. In all experiments, the input water temperature was 3.0 °C, and the surrounding air flux due to each fan was 0.95 m^3/min.

with time as the icicle grows (Fig. 3.6(a)).

In Fig. 3.7, we compare the mass growth rates at $t = 1$ hr under different conditions. More precisely, the rate is defined as the slope of the best-fit line to the $M_I(t)$ data between 50 and 70 minutes after the initiation of icicle growth. In general, since both dL/dt and dR_0/dt increase with decreasing ambient temperature (Figs. 3.4(a) and 3.5(a)), it is no surprise that the icicle mass grows faster at lower temperatures (Fig. 3.7(a)). On the other hand, dL/dt increases while dR_0/dt decreases as the input mass flux is decreased (Figs. 3.4(b) and 3.5(b)); the net result is that at $t = 1$ hr, the icicle mass grows faster if water is fed to its root more slowly (Fig. 3.7(b)). However, this is not true for all times. Under otherwise identical conditions, the post-cessation mass of an icicle made from a lower water supply rate (e.g. the cyan time-series in Fig. 3.6(a)) may increase more slowly than the pre-cessation mass of an icicle made from a higher water supply rate (e.g. the red time-series in Fig. 3.6(a)).

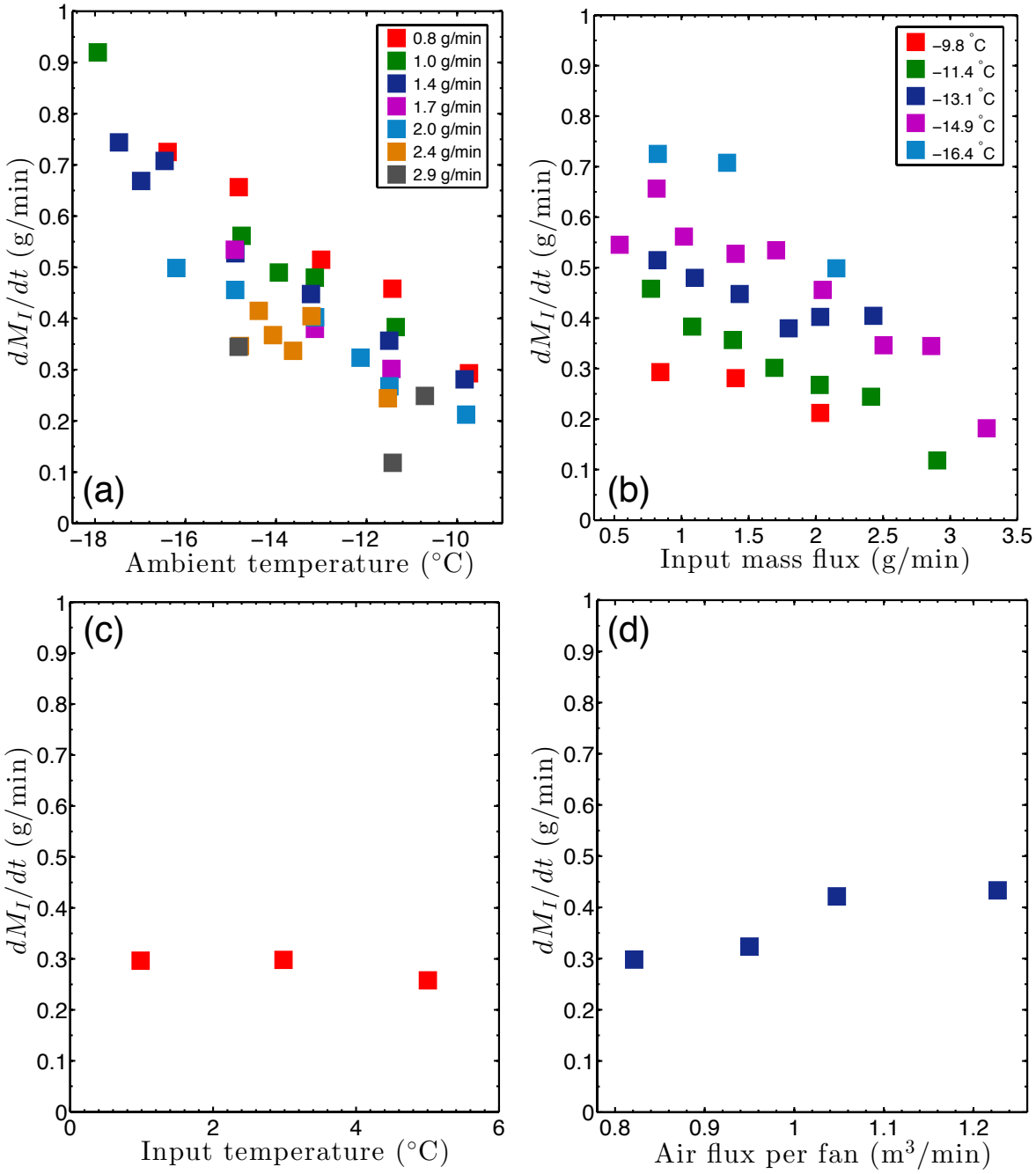

Figure 3.7: Mass growth rates of distilled water icicles *vs.* extrinsic conditions. The fixed variables in each panel are: (a) water supply rate (as shown in the legend), input water temperature (3.0 °C for all experiments), and air flux per fan (0.95 m^3/min for all experiments); (b) ambient wall temperature (as shown in the legend), input water temperature (3.0 °C for all experiments), and air flux per fan (0.95 m^3/min for all experiments); (c) ambient wall temperature (−12.1 °C for all experiments), water supply rate (2.0 g/min for all experiments), and air flux per fan (0.82 m^3/min for all experiments); (d) ambient wall temperature (−12.1 °C for all experiments), water supply rate (2.0 g/min for all experiments), and input water temperature (3.0 °C for all experiments). Each colour corresponds to one set of experiments with the same values of the fixed variables.

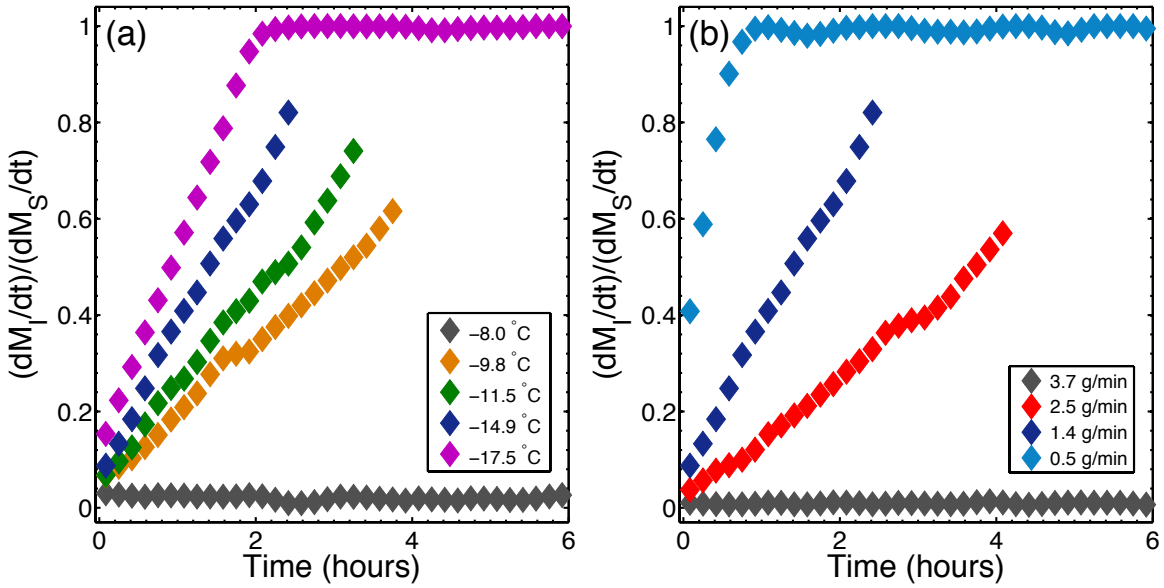

Figure 3.8: Time evolution of the mass flux ratio $\mathcal{R}_\mathcal{M}$ of some distilled water icicles. For the runs in (a), the water supply rate was 1.4 g/min, and the legend shows the ambient wall temperature. For the runs in (b), the ambient wall temperature was -14.9 °C, and the legend shows the water supply rate. In all experiments, the input water temperature was 3.0 °C, and the surrounding air flux due to each fan was 0.95 m^3/min.

A better way to compare the mass growth of icicles is to define a dimensionless ratio

$$\mathcal{R}_\mathcal{M} = \frac{dM_I/dt}{dM_S/dt}, \tag{3.33}$$

where the time derivatives are instantaneous mass fluxes. This ratio indicates how much of the feed water is frozen onto the icicle at a given time. Fig. 3.8 plots $\mathcal{R}_\mathcal{M}(t)$ for some typical runs. Some conditions are not favourable for icicle formation (e.g. the environment is too warm, the water supply rate is too high); in these cases, $\mathcal{R}_\mathcal{M} = 0$ at all times. In all other cases, as time increases and the icicle gets longer, more and more of the feed water gets consumed by the icicle, and less and less of it drips off. During growth, the fraction of the input water that freezes to form the icicle increases more rapidly for lower ambient temperatures (Fig. 3.8(a)) and lower water supply rates (Fig. 3.8(b)). $\mathcal{R}_\mathcal{M}$ reaches 1 at cessation and remains at 1 after cessation; this means once the length growth stops, all of the water supply is frozen onto the sides of the icicle before reaching the tip.

	Value		**Value**
ρ_L	1.000×10^3 kg/m^3	T_{LA}	273.15 K
ρ_I	0.917×10^3 kg/m^3	T_m	273.15 K
ρ_A	1.29 kg/m^3	$\rho_{\text{sat}}(T_m)$	4.85×10^{-3} kg/m^3
c_A	1.005×10^3 J/(kg·K)	$\mathcal{M}_L$	18.015×10^{-3} kg/mol
c_L	4.210×10^3 J/(kg·K)	$\mathcal{R}$	8.3145 J/(mol·K)
L_f	3.34×10^5 J/kg	f_L	0.26
L_v	2.50×10^6 J/kg	δ_T	7.5×10^{-5} m
σ_B	5.6704×10^{-8} W/(m^2·K^4)	R_p	2.45×10^{-3} m

Table 3.1: Parameter values in heat transfer calculations for distilled water icicles. The values of f_L, δ_T, and R_p are taken from Ref. [14].

Next, we shift our focus to the second goal of this section: to estimate how much the various heat transfer mechanisms are responsible for the increase in the mass of water consumption. To achieve this, we first determine the heat transfer coefficients empirically from our data. Using the model in Sec. 3.2, the convective heat transfer coefficient at the walls of the icicle can be expressed as

$$H = \frac{\tilde{\rho_I} L_f (1 - f_L)(dR/dt) - \sigma_B (T_{LA}^4 - T_A^4)}{\Delta T_A + (L_v \Delta \rho_v)/(\rho_A c_A)}, \tag{3.34}$$

and the convective heat transfer coefficient at the tip can be expressed as

$$H^T = \frac{W_T c_L \Delta T_p / A_p + \rho_I L_f (\delta_T / R_p)(dL/dt) - \sigma_B (T_{LA}^4 - T_A^4)}{\Delta T_A + (L_v \Delta \rho_v)/(\rho_A c_A)}. \tag{3.35}$$

To compute these, we use the values in Table 3.1, as well as the following experimental quantities: for advection-diffusion and evaporation, T_A is the measured air temperature (in Kelvin); for radiation, we let T_A be the temperature at the walls of the apparatus (in Kelvin); $\mathcal{R}_\mathcal{H}$, which appears in $\Delta\rho_v$, is the measured relative humidity; the radial and tip growth speeds are dR_0/dt and dL/dt as defined in Sec. 3.3; we approximate W_T as $W_0 - dM_I/dt$, where dM_I/dt is as defined earlier in this section – here, mass transport due to evaporation is accounted for, because we found M_I by subtracting M_S by M_D.

At the sides of our laboratory-grown icicles, the convective heat transfer coefficient has a mean of 12 ± 2 W/(m^2·K) (Fig. 3.9(a)). Since H is approximately constant across a broad range of conditions, the heat transfer model for the lateral growth of icicles in Sec. 3.2 is consistent with our data. Knowing H, we can compare the contributions of the different heat transfer mechanisms to the lateral growth using Eqs. 3.17-3.19. In Fig. 3.9(c), we plot the ratios J_{AD}/J_{total}, J_E/J_{total}, and J_R/J_{total}, where $J_{\text{total}} = J_{AD} + J_E + J_R$, over the range of parameter space we traversed. The dominant heat transfer mechanism controlling the lateral growth is advection-diffusion; the contributions due to evaporation and radiation are also significant but secondary.

The convective heat transfer coefficient at the tip is higher than that at the sides; it has a mean of 27 ± 3 W/(m^2·K) (Fig. 3.9(b)). Since H^T is approximately constant for a wide range of tip growth speeds, the heat transfer model for the length growth of icicles in Sec. 3.2 is consistent with our data. Using the values of H^T and Eqs. 3.12-3.14, we find the ratios $J^T_{AD}/J^T_{\text{total}}$, J^T_E/J^T_{total}, and J^T_R/J^T_{total}, where $J^T_{\text{total}} = J^T_{AD} + J^T_E + J^T_R$ (Fig. 3.9(d)). $J^T_{AD}/J^T_{\text{total}}$ and J^T_E/J^T_{total} are slightly higher than J_{AD}/J_{total} and J_E/J_{total}, while J^T_R/J^T_{total} is about a half of J_R/J_{total}. In Fig. 3.9(d), we also plot the ratios J^T_C/J^T_{total} and J^T_F/J^T_{total} using Eqs. 3.15 and 3.29. For a faster growing icicle, a higher fraction of J^T_{total} is associated with its tip growth, and a smaller fraction is associated with the pendant drop cooling.

3.5 Effect of salinity

So far, we have focused on icicles made from distilled water. However, the water sources for natural icicles often contain impurities; for example, marine icicles are formed from saline water. In this section, we investigate how icicle growth is affected when small amounts of salt are added to the feed water.

We begin by looking at how the model for the lateral growth of icicles in Sec. 3.2 is changed by the addition of salt. The theory summarized here is adapted from the work of Chung *et al.*, who developed a numerical model for the growth of saline water icicles [16]. Following Sec. 3.2, we treat the icicle as a stack of thin horizontal slices. However, it is no longer sensible to set the temperature at the sides of the different slices identically to

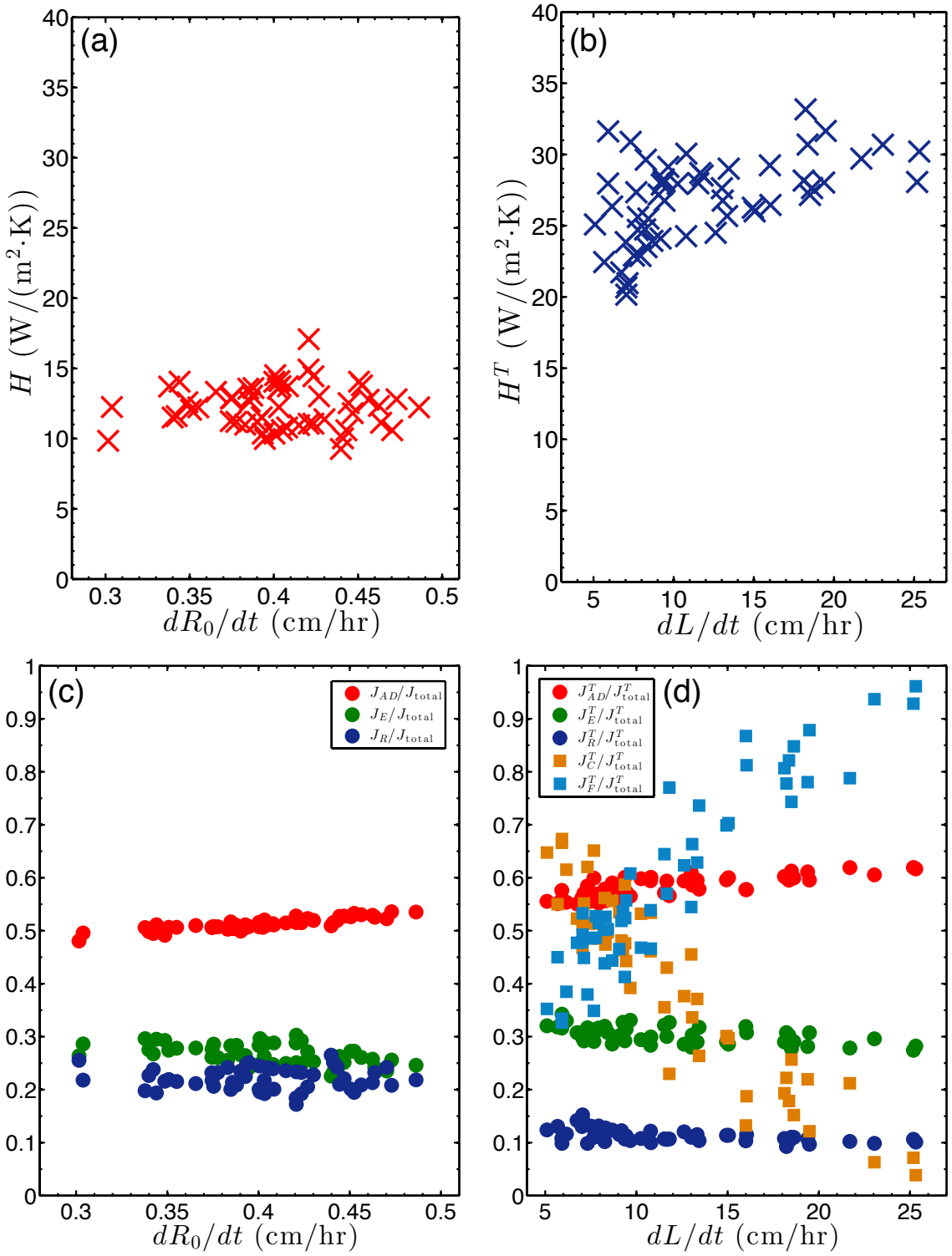

Figure 3.9: Convective heat transfer coefficients at (a) the sides and (b) the tip of distilled water icicles grown under various conditions. The contributions of advection-diffusion, evaporation, and radiation in the (c) radial growth, (d) pendant drop cooling and tip growth of these icicles.

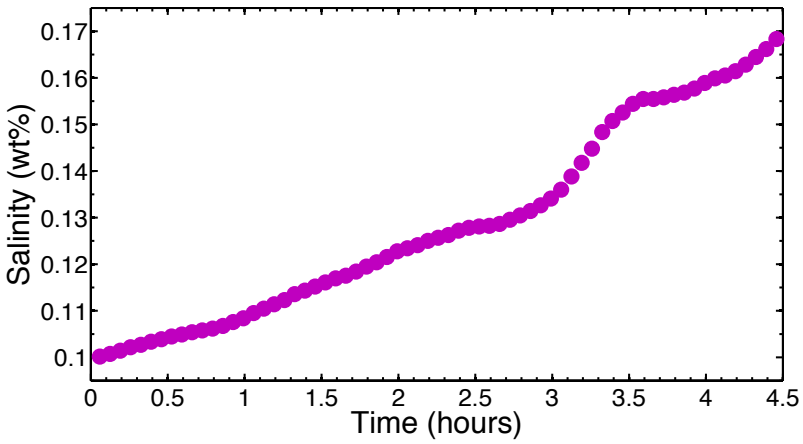

Figure 3.10: Time-series of the drip-off salinity of an icicle made from feed water with 0.1 wt% NaCl.

the freezing point of pure water. Since salt is rejected from ice as salt water freezes, the salinity of the water film should increase as it flows towards the tip. We confirmed this experimentally by tracking the 'instantaneous' salinity of the drip-off from a lab-grown salty water icicle. A Vernier salinity sensor was placed inside a small tilted beaker, which caught the drip-off water before it flowed into a larger container. Fig. 3.10 shows the drip-off salinity, which indeed increased during icicle growth. As a result of freezing point depression, not only must the icicle surface temperature be below 0 °C, it must also decrease towards the tip — i.e. each cylindrical slice now has a different T_{LA}.

Here, we consider only the part of the icicle near the root, where the salinity of the water film is close to the salinity of the feed water. As in the case of distilled water icicles, the conservation of energy and the various heat fluxes can be expressed by Eqs. 3.11, 3.17-3.19, and 3.32. The convective heat transfer coefficient also has the same expression as before, i.e. Eq. 3.34.

According to Chung *et al.* [16] and Makkonen [47], T_{LA} and $\Delta\rho_v$ for saline water icicles can be parameterized in the following way:

$$T_{LA} = -54.0S - 600S^3, \tag{3.36}$$

$$\Delta\rho_v = \rho^S_{\rm sat}(T_{LA}) - \mathcal{R}_{\mathcal{H}}\rho_{\rm sat}(T_A), \tag{3.37}$$

$$\rho^S_{\rm sat}(T) = (1 - 0.537S)\rho_{\rm sat}(T), \tag{3.38}$$

where T_{LA} has a unit of °C, S is the unitless mass fraction of salt in the water, ρ_{sat}^{S} is the saturated vapour density for saline water, and ρ_{sat} is the saturated vapour density for pure water as defined in Eq. 3.24. Moreover, L_v and ρ_L are now functions of salt concentration as well. Fig. 3.11 shows how T_{LA}, L_v, and ρ_L vary with salinity over the range covered in our experiments. This model assumes the temperature change across the thin water film is negligible, salt is uniformly distributed across the film, and all of the salt is rejected by freezing.

Next, we present experimental data for the growth of saline water icicles. Fig. 3.12 shows typical time-series for the length, radius, and mass of icicles grown from water with varying salt concentrations under the same conditions. L, R_0, M_I, and $\mathcal{R}_{\mathcal{M}}$ were all found using the same algorithms described in Secs. 3.3-3.4 for distilled water icicles. Like distilled water icicles, the lengths of saline water icicles initially increase linearly with time, and cessation is observed after a period of growth. However, as the salinity of the feed water increases, the transition to cessation becomes less sharp (Fig. 3.12(a)). This is in agreement with the work of Chung *et al.* [16], who computationally and experimentally studied icicles made from brine with a salinity of 3 wt%.

Chung *et al.* found that the addition of salt to the feed water decreases the length and mass growth rates of the resultant icicle [16]. We discovered that, in some cases, there also exists a range of salt concentration for which the icicle length and mass grow faster with increasing salinity (Fig. 3.12(a),(c),(d)). This occurs for very low salt concentrations of less than 1 wt% and is clearer under conditions of fast growth. Above this threshold, the growth rates decrease with increasing salinity (Fig. 3.12(a),(c),(d)). At sufficiently high salinities, freezing point depression can cause T_{LA} to become comparable to the ambient temperature; in this limit, the heat flux is low and the ice growth is slow.

These results are also evident from Fig. 3.13, in which we plot the tip and radial growth speeds of saline water icicles grown under various conditions. Here, dL/dt is the slope of the best-fit line to the initial linear regime of the length time-series. More precisely, this regime begins at $t = 0$ and ends when the slope decreases by more than 50 %. For consistency, the tip growth speeds of distilled water icicles in Sec. 3.3 were also obtained using the same algorithm. As defined for distilled water icicles, the dR_0/dt here

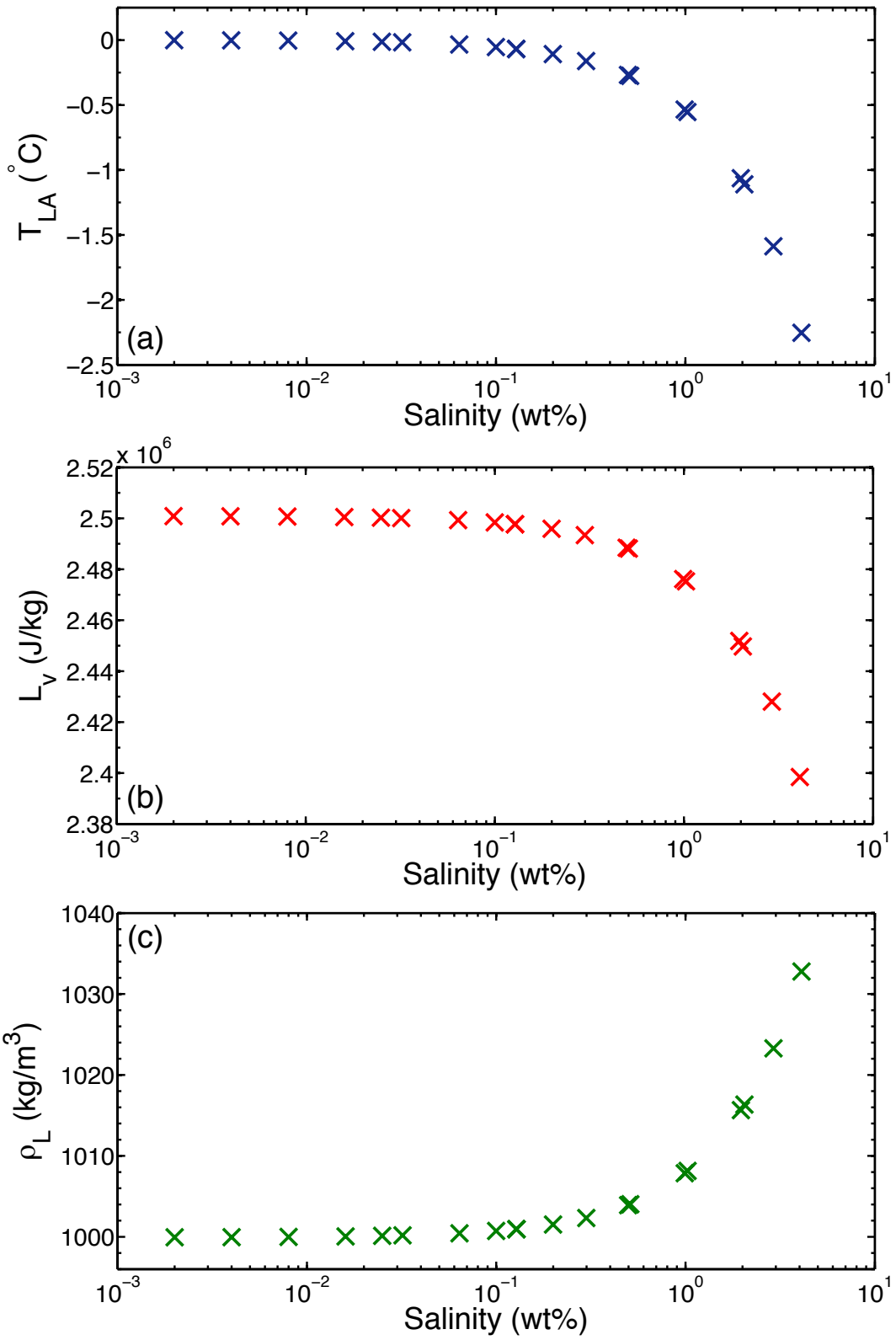

Figure 3.11: Saline water properties *vs.* NaCl concentration: the freezing temperature in (a) is estimated using Ref. [47]; the latent heat of vaporization in (b) and the density in (c) are calculated using Ref. [46] at 0 °C.

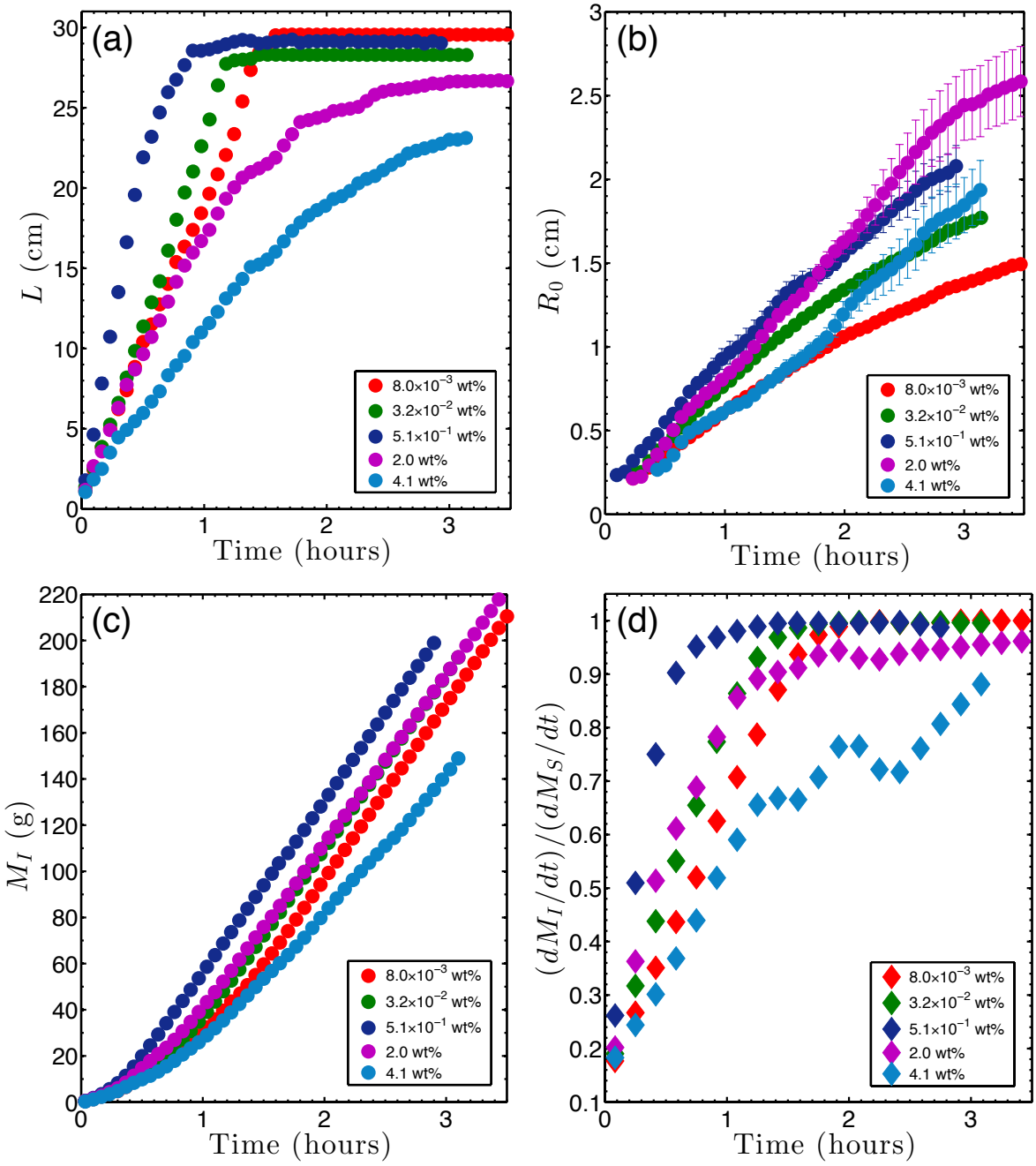

Figure 3.12: Time evolution of the (a) length, (b) radius, (c) mass, and (d) mass flux ratio $\mathcal{R}_{\mathcal{M}}$ of some saline water icicles. The colour-coded symbols in the four panels correspond to the same set of experiments. The legends show the NaCl concentration of the feed water in each run. In all experiments, the ambient wall temperature was -15.0 °C, the water supply rate was 1.3 g/min, the input water temperature was 2.2 °C, and the surrounding air flux due to each fan was 1.05 m^3/min.

is the slope of the best-fit line to the radius time-series at 5 cm below the root during the first 2 hours of growth. The salinity dependence of the radial growth speed follows a similar trend as that of the tip growth speed.

Using our model and data for saline water icicles, the contributions of the various heat transfer mechanisms to their radial growth can be determined. Assuming the phenomenological heat transfer coefficient H is unaffected by the salt added to the water source, we set it to be the mean of the H values found for distilled water icicles (Fig. 3.9(a)) and calculated the ratios J_{AD}/J_{total}, J_E/J_{total}, and J_R/J_{total} using Eqs. 3.17-3.19. The relative contributions of advection-diffusion, evaporation, and radiation to the radial growth of saline water icicles, plotted in Fig. 3.14(a), are comparable to those for distilled water icicles (Fig. 3.9(c)); they are also fairly constant across growth conditions. By holding H constant and using Eq. 3.34, we were able to estimate the fraction f_L of the liquid film that is incorporated into the "spongy" or "mushy" ice matrix. As shown in Fig. 3.14(b), $f_L = 0.26$, which was used in the model of distilled water icicles, is recovered for $S = 0$. f_L increases with salinity; this is in agreement with experiments by Wettlaufer *et al.* [53], who measured the solid fraction, i.e. $1 - f_L$, in the mushy layer of lab-grown sea ice.

3.6 Cessation of growth

In this section, we take a closer look at the cessation of icicle growth. In Sec. 3.3, we found that distilled water icicles can suddenly stop growing at the tip. In Sec. 3.5, we observed that the transition to cessation is less sharp for saline water icicles. In those sections, we identified a time t_L at which the initial linear growth of the icicle length ends. t_L was defined as the time at which the slope of $L(t)$ decreases by more than 50 %; the data before $t = t_L$ was used to calculate the linear tip growth speed dL/dt, while the data after $t = t_L$ was excluded in this calculation. However, since not all icicles undergo an abrupt cessation, t_L is not always equivalent to the time of cessation. Here, we define a cessation time t_C as the time at which the slope of $L(t)$ decreases to a value less than 1 cm/hr, which is one-fifth of the lowest dL/dt measured in the parameter space we traversed.

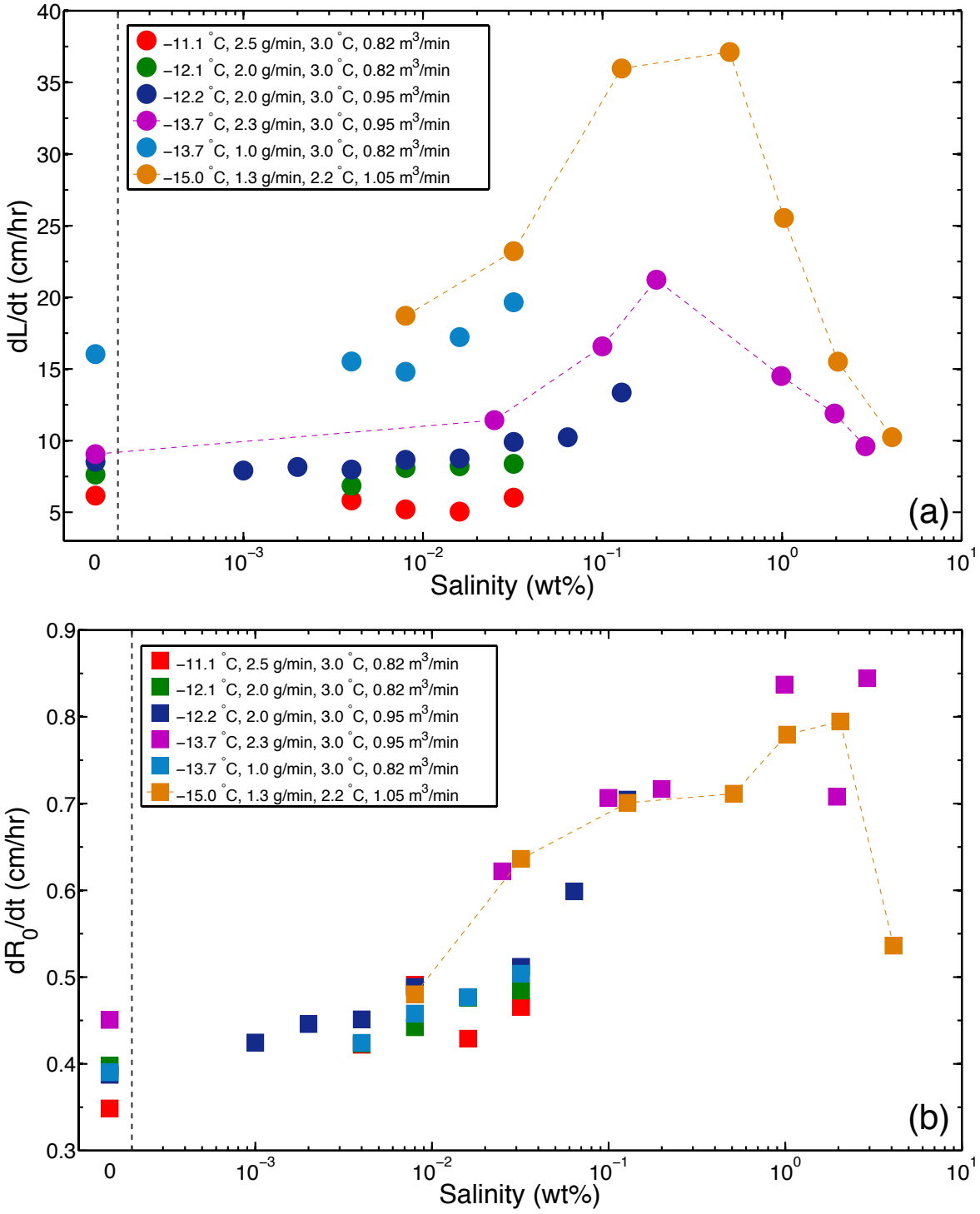

Figure 3.13: (a) Tip and (b) radial growth speeds of saline water icicles *vs.* feed water salinity. The fixed variables are: ambient wall temperature, water supply rate, input water temperature, and surrounding air flux due to each fan. Each colour corresponds to one set of experiments with the same values of the fixed variables. The legends show the values of the fixed variables for each set of experiments. The vertical dashed line in each panel is a scale break, to the right of which salinity is plotted on a log scale.

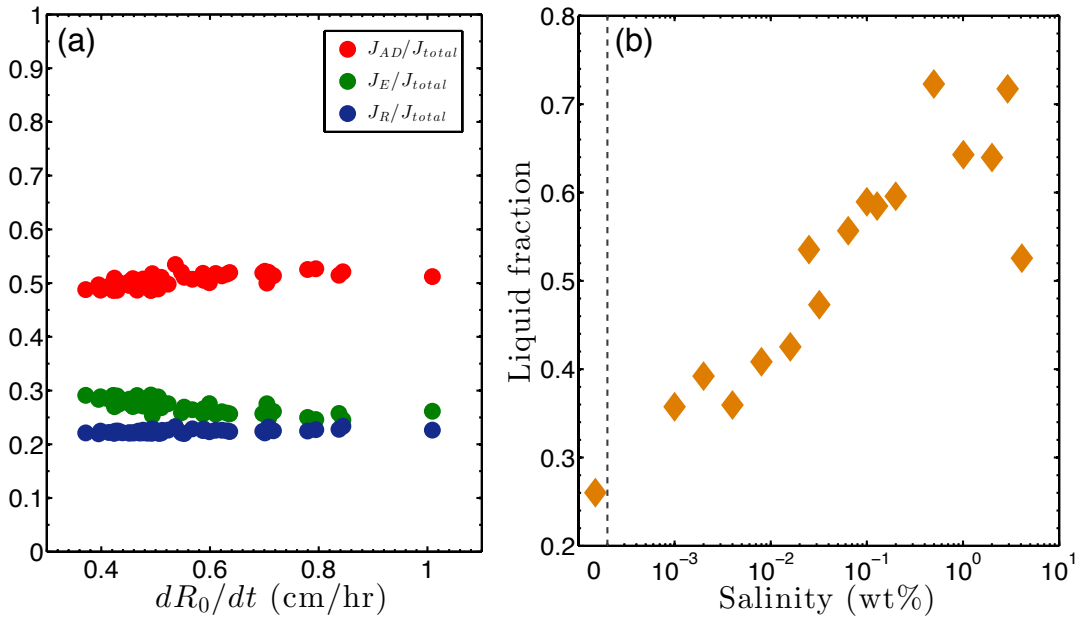

Figure 3.14: (a) The contributions of advection-diffusion, evaporation, and radiation in the radial growth of saline water icicles made under various conditions. (b) The liquid fractions of distilled and saline water icicles. The vertical dashed line in (b) is a scale break, to the right of which salinity is plotted on a log scale.

In Fig. 3.15, $t_C - t_L$ is shown for distilled and saline water icicles that meet the cessation criterion and hence have a well-defined t_C. As expected, this difference is largest for icicles made from the saltiest water. It is likely that all lab-grown icicles would eventually undergo cessation without experimental limitations, such as the height of the icicle machine. In the following discussion, we shall consider cessation in the context of our experiment — we say the growth of an icicle ceases if its speed of tip growth drops to a value below 1 cm/hr prior to exceeding the viewing window of our apparatus; an icicle does not undergo cessation if it grows beyond the bottom of the viewing window. Of course, for runs that were ended while the icicle was still growing steadily within the viewing window, no conclusions were made regarding their cessation.

The cessation of icicles was predicted by the models of Makkonen [14], Szilder *et al.* [25], and Chung *et al.* [16]. Fig. 3.16 shows typical time-series data for ceasing icicles from our experiments. As the addition of salt to the feed water causes the tip of the resultant icicle to make a more gradual transition from linear growth to cessation (Fig. 3.16(a)), its mass flux ratio $\mathcal{R}_{\mathcal{M}} = (dM_I/dt)/(dM_S/dt)$ also approaches 1 more

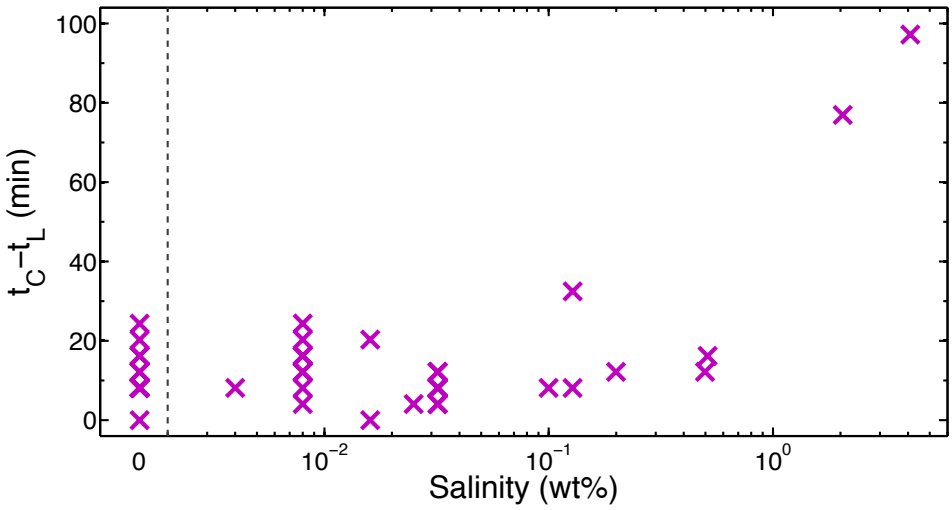

Figure 3.15: Transition time from linear tip growth to cessation. The icicles here were grown under different conditions. Since the length time-series was averaged over each rotation, the resolution of the time axis is the rotational period: 4 minutes. The vertical dashed line is a scale break, to the right of which salinity is plotted on a log scale.

slowly after a rapid initial rise (Fig. 3.16(c)). In other words, unlike distilled water icicles which consume all the incoming water once the length growth has slowed down noticeably, pendant drops may continue to drip from saline water icicles after the tip growth speed has decreased significantly. Fig. 3.16(b) shows the radius at various heights along the icicle. After cessation, the radial growth at a given height can continue for some period of time before decelerating and possibly coming to a halt; the latter occurs if all of the feed water freezes before making its way there. The further away from the root of the icicle, the sooner the radius stops growing.

Next, we check two hypotheses that Chung *et al.* [16] made about the cessation of saline water icicles. Firstly, they predicted that icicles made from salt water continued to drip after cessation. In Fig. 3.17, we plot the ratio of the drip-off mass flux to the water supply rate, i.e. $1 - \mathcal{R}_{\mathcal{M}}$, for a representative sample of icicles made from water of different salt concentrations. Here, time zero corresponds to the time of cessation t_C. While the two icicles made from water with salinities above 1 wt% continued to drip after their tip growth speed became less than 1 cm/hr, the fraction of input water that dripped off the other saline water icicles after their cessation was effectively zero.

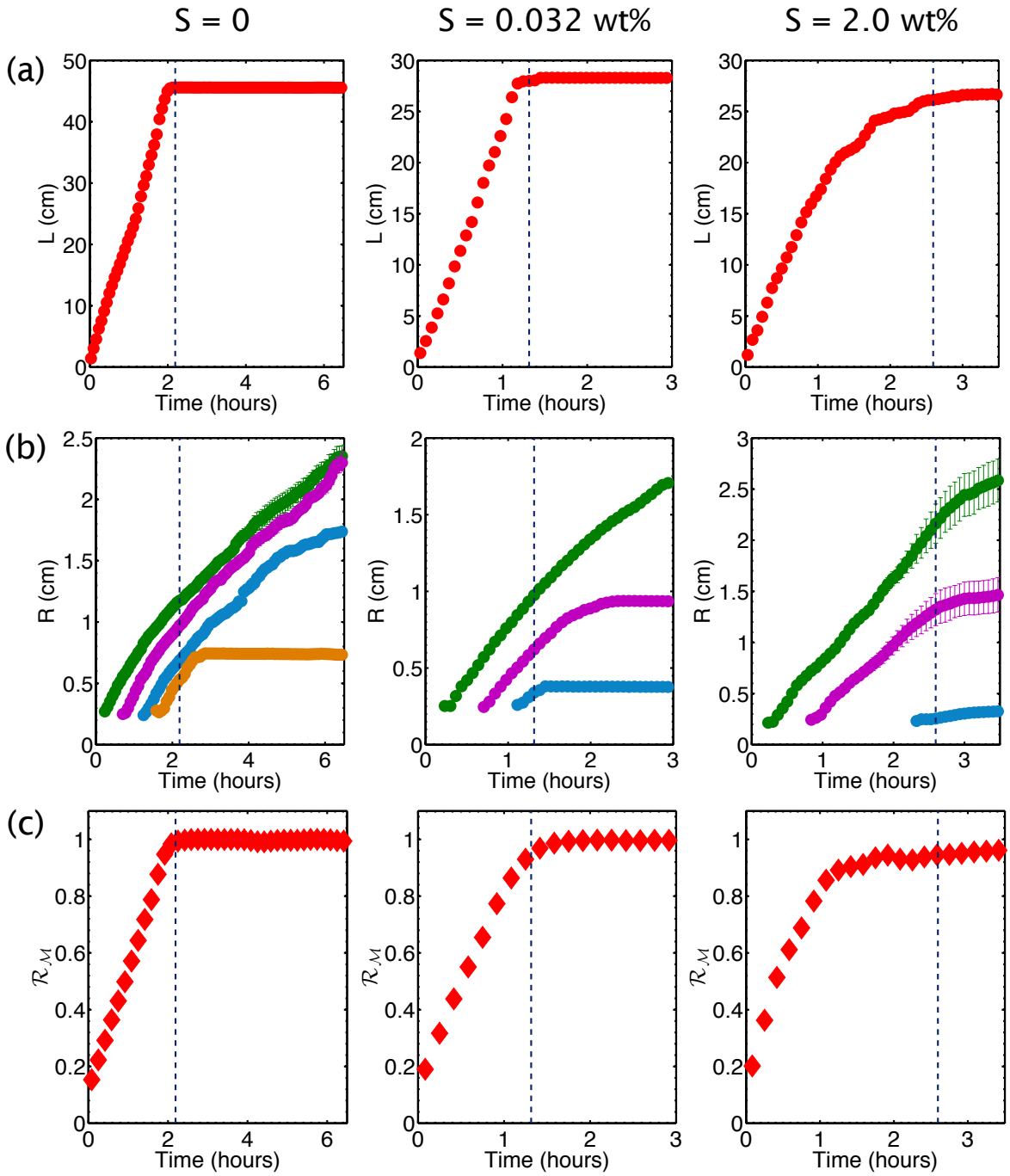

Figure 3.16: Time evolution of the (a) length, (b) radius, and (c) mass flux ratio $\mathcal{R}_\mathcal{M}$ of 3 ceasing icicles. The feed water salinity for each is shown at the top. For the distilled water icicle: the ambient temperature was -17.5 °C, the water supply rate was 1.4 g/min, the input water temperature was 3.0 °C, and the surrounding air flux due to each fan was 0.95 m^3/min. For the two saline water icicles: the ambient temperature was -15.0 °C, the water supply rate was 1.3 g/min, the input water temperature was 2.2 °C, and the surrounding air flux due to each fan was 1.05 m^3/min. In (b), the green, magenta, cyan, and brown circles correspond to the radius at 5, 15, 25, and 35 cm below the root respectively. The vertical dashed line in each plot marks the cessation time t_C.

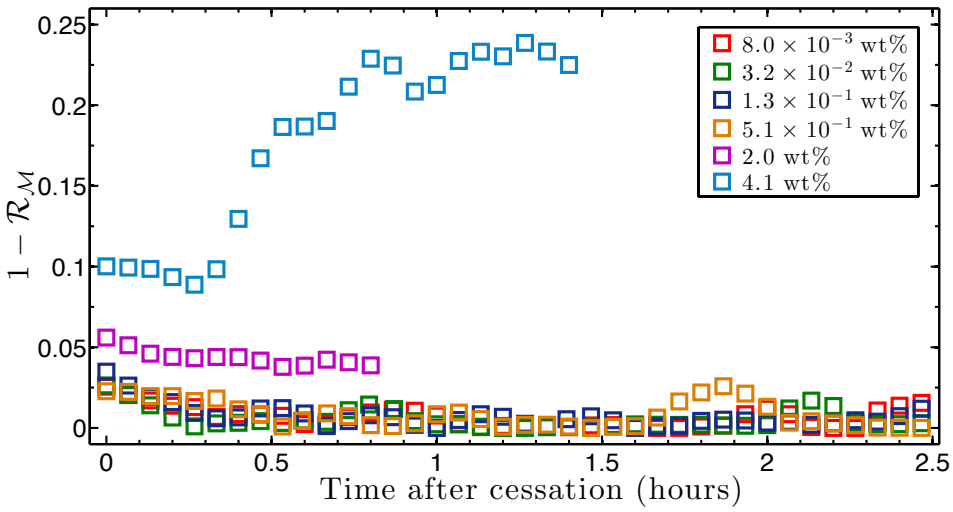

Figure 3.17: Ratio of drip-off to input mass flux after cessation. The legend indicates feed water salinities. The icicles here were grown under different conditions.

Secondly, Chung *et al.* claimed that saline water icicles undergo cessation when the tip temperature is equal to the ambient temperature. To test this, we probed the 'instantaneous' drip-off salinity S_D during several experiments, using the methods described in Sec. 3.5. Fig. 3.18 shows the results for three saline water icicles that underwent cessation. Before the initiation of icicle growth, the salinity of the drip-off water was equal to that of the feed water. Consistent with our observation in Sec. 3.5, S_D increased during icicle growth. Since t_C is defined as the time at which the length growth rate dips below 1 cm/hr, the drip-off salinity may continue to increase for a while after $t = t_C$. After cessation, there was an obvious drop in the rate of increase of S_D. In this regime, $1 - \mathcal{R}_{\mathcal{M}} \approx 0$ but $dS_D/dt \neq 0$ for these runs; this was likely due to evaporation of the last bit of drip-off water sitting inside the small tilted beaker after its influx had stopped.

For the three icicles in Fig. 3.18, which were made from 0.13, 0.20, and 0.50 wt% NaCl solutions, the maximum salinities prior to the drop in dS_D/dt were 0.25, 0.47, and 1.05 wt% respectively. By substituting these into Eq. 3.36, we estimated their tip temperature to be -0.14, -0.25, and $-0.57\,^{\circ}\mathrm{C}$. However, the air surrounding these icicles had a temperature of -9.7, -11.1, and $-11.0\,^{\circ}\mathrm{C}$. Therefore, these icicles stopped growing in length even though their tip temperature was significantly higher than their ambient temperature. While we have refuted the hypothesis of Chung *et al.*, it may hold true for

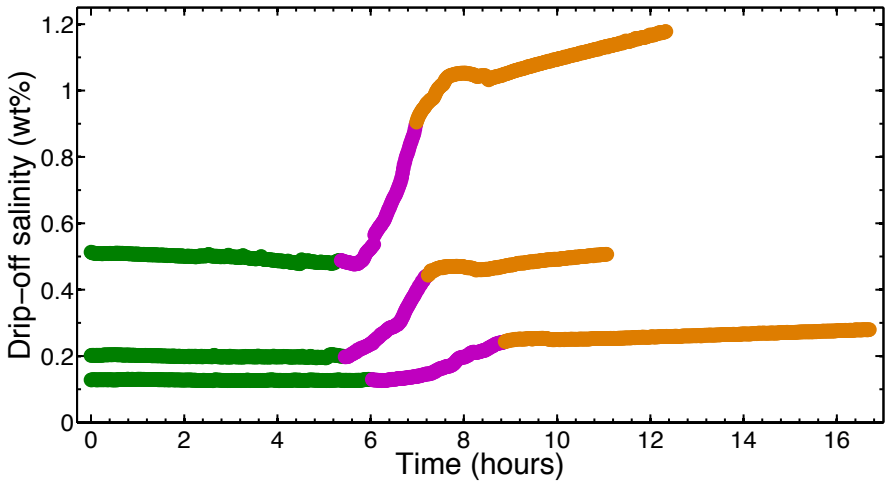

Figure 3.18: Drip-off salinities before, during, and after the growth of 3 icicles made from saline water of 0.13, 0.20, and 0.50 wt% under different conditions. The magenta segment begins when the icicle starts growing and ends when it undergoes cessation.

higher feed water salinities — more experiments are needed to check this.

Finally, we identify growth conditions that make cessation occur at an earlier time. Fig. 3.19 shows points in the parameter space of ambient temperature and input mass flux for which the growth of our laboratory icicles ceased. Cessation occurred more often when the water was supplied more slowly; in some cases, lowering the surrounding temperature encouraged cessation. Cessation was more frequently observed for saline water icicles than distilled water icicles. When salt was added to the feed water, some resultant icicles ceased to elongate under conditions of ambient temperature and input mass flux for which distilled water icicles continued to grow. The model of Szilder *et al.* for pure water icicles [25] predicted that the time of cessation decreases as the speed of tip growth increases. We confirmed this to be true for both distilled and saline water icicles (Fig. 3.20(a)). Moreover, we found that the cessation length of an icicle, $L(t_C) \neq L(t_L) \approx (dL/dt) \times t_L$, and dL/dt are also inversely correlated, though icicles made from water with salinities above 1 wt% deviated from this trend (Fig. 3.20(b)).

This concludes the chapter on the growth and cessation of icicles, in which we measured the tip and radial growth independently of each other. The icicle was treated as a stack of thin cylindrical slices, and its radial growth was only probed at selected heights. In the following chapter, we shift our focus to studying the global shape of icicles.

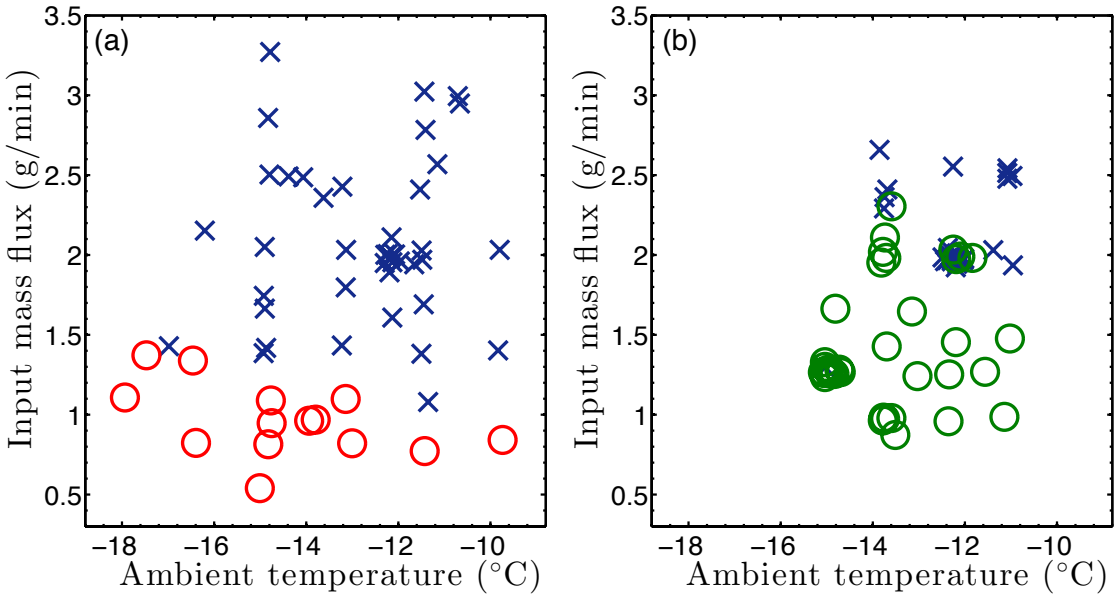

Figure 3.19: Cessation occurrences for (a) distilled and (b) saline water icicles in the parameter space of ambient wall temperature and water supply rate. The range of feed water salinity in (b) was 1.0×10^{-3} to 4.1 wt%. Circles indicate that cessation was observed during the experiment; crosses indicate that the icicle grew past the bottom of the viewing window.

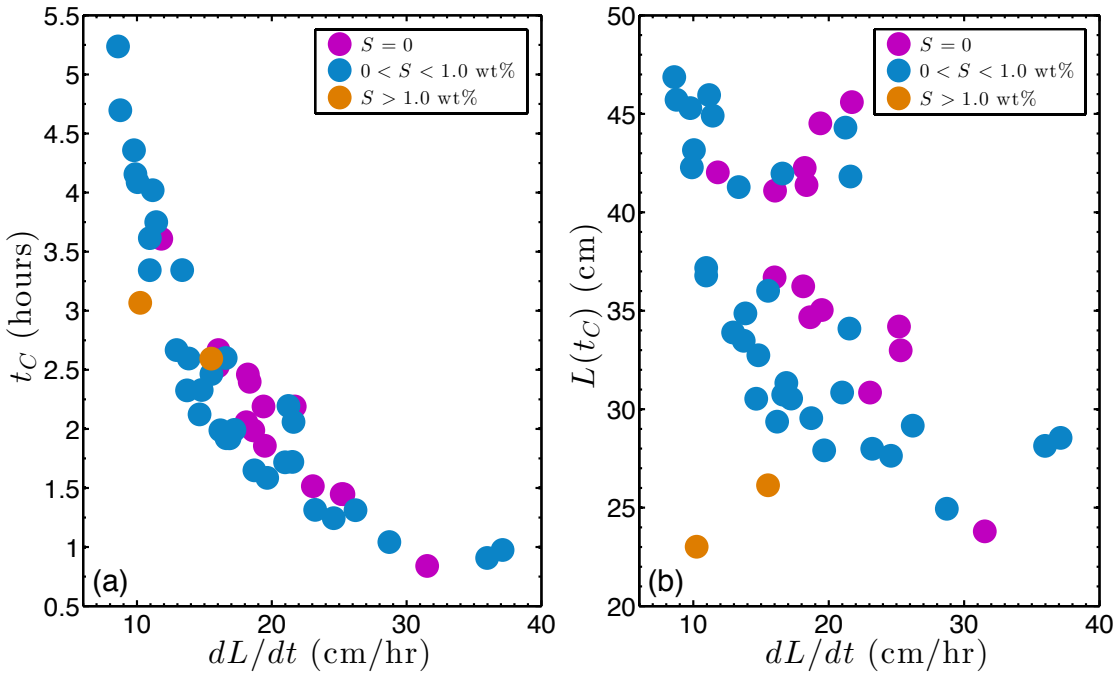

Figure 3.20: (a) Cessation time t_C and (b) the icicle length at $t = t_C$, plotted against the speed of tip growth. The legends indicate feed water salinities. The icicles here were grown under different conditions.

Chapter 4

Self-similar shape

The models of Makkonen [14], Szilder *et al.* [25], and Chung *et al.* [16], discussed in Ch. 3, provided various insights into icicle formation. In particular, their prediction that the length of an icicle grows significantly faster than its radius implied the long and slender form we've come to associate with icicles. However, these theories did not explicitly derive a mathematical expression for their overall shape. The first analysis that did so was that of Short *et al.* [26]. By considering the relevant physical mechanisms underlying icicle growth and using a strict free-boundary approach, they made the remarkable prediction that all icicles converge to a universal, self-similar shape. This prediction had previously been compared to eight icicle images found on the Internet [26]. The main objective of this chapter is to report on the first direct test of the self-similarity theory against laboratory experiments.

This chapter begins with a summary of the theory by Short *et al.* [26] and its implications (Sec. 4.1). Next, we describe our methods for comparing this theory with data, as well as observations from our preliminary, partially-controlled experiments (Sec. 4.2). These observations motivate our fully-controlled experiments, the results of which are presented in Sec. 4.3. It turns out that some icicles fit the theoretical prediction to an uncanny degree, while others are poorly described by it; thus, an important goal here is to identify the conditions under which icicles agree with or deviate from the self-similarity theory. A fraction of our lab-grown icicles exhibit shapes that deviate so far from self-similarity that they cannot be reasonably described by this theory; their

	Value		Value
κ_L	1.4×10^{-7} m^2/s	κ_A	1.9×10^{-5} m^2/s
ν_L	1.8×10^{-6} m^2/s	ν_A	1.3×10^{-5} m^2/s
g	9.8 m/s^2	β_A	3.7×10^{-3} K^{-1}

Table 4.1: Parameter values in thin water film and air boundary layer calculations; both are assumed to be at 0 °C.

non-ideal features are discussed in Sec. 4.4.

4.1 Theoretical context

In this section, we summarize the work of Short *et al.* [26], who derived a mathematical expression that predicts the global shape of a uniformly advancing icicle.

Short *et al.* assumed all of the latent heat released from the icicle growth is conducted across the thin water film; the advective heat transport down the water layer was ignored. Using the parameter values in Table 4.1, we find the thickness and surface speed of the water film (Eqs. 3.8 and 3.9) to be $h = 5.6 \times 10^{-5}$ m and $u_s = 8.5 \times 10^{-3}$ m/s for a typical icicle radius of $R = 10^{-2}$ m and a water supply rate of $Q_0 = 2 \times 10^{-8}$ m^3/s; $\theta = 0$ is assumed. The Péclet number (Table A.2) for the water film $\mathrm{Pe}_L = hu_s/\kappa_L = 3.4$, where κ_L is the thermal diffusivity of water; this indicates that advection is at least as important as conduction, and hence the assumption of negligible advection is questionable. The Reynolds number (Table A.2) for the water film $\mathrm{Re}_L = hu_s/\nu_L = 0.27$, where ν_L is the kinematic viscosity of water; this suggests its flow is laminar. In reality, both Pe_L and Re_L evolve with time, because for a given fixed Q_0, h and u_s vary with R which increases during icicle growth (Fig. 3.3); their typical time dependence is shown in Fig. 4.1.

Moreover, Short *et al.* assumed a calm growth environment. Thus, the heat transport is affected by natural convection and governed by a rising boundary layer of warm air around the icicle. This thermal boundary layer exists because the icicle surface is warmer than its surrounding air, and it rises because of its buoyancy. In modelling the thickness δ of this layer, they justified the usage of the natural convection boundary layer thickness

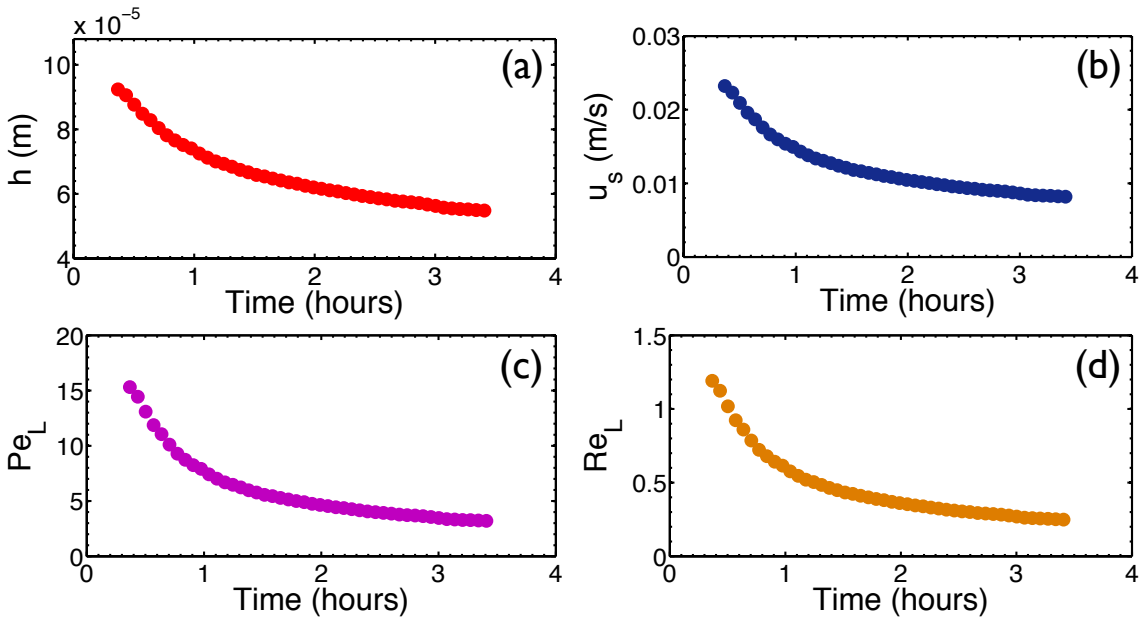

Figure 4.1: Time dependence of the (a) thickness, (b) surface speed, (c) Péclet number, and (d) Reynolds number of the thin water film on a typical lab-grown distilled water icicle. The radial growth of this icicle, measured at 5 cm below its root, was shown by the green data in Fig. 3.3(b).

for a flat, vertical, and isothermal plate [26, 50]:

$$\delta = C\ell\left(\frac{z}{\ell}\right)^{1/4}, \quad \ell = \left(\frac{\nu_A^2}{g\beta_A\Delta T_A}\right)^{1/3}, \tag{4.1}$$

where C is a dimensionless constant of order unity which is related to the Prandtl number of air, z is the vertical distance away from the tip, ν_A is the kinematic viscosity of air, g is the acceleration due to gravity, β_A is the volumetric thermal expansion coefficient of air, and ΔT_A is the difference between the surface temperature and the ambient temperature. Since this approximation is unjustifiable near the tip of the icicle, the theory is not expected to work there.

The peak speed of the warm air in the boundary layer [26, 50] is

$$u_p = \frac{2}{3}\sqrt{g\beta_A\Delta T_A z}. \tag{4.2}$$

Using the values in Table 4.1, we find $\delta = 3.1 \times 10^{-3}$ m and $u_p = 1.8 \times 10^{-1}$ m/s for

$C = 1$, $z = 0.2$ m, and $\Delta T_A = 10$ K. Thus, away from the tip of an icicle, the thermal boundary layer is typically thicker than the water film but thinner than its radius. The Reynolds number of the natural convection boundary layer $\mathrm{Re}_A = \delta u_p/\nu_A = 43$, and its Péclet number $\mathrm{Pe}_A = \delta u_p/\kappa_A = 29$, where κ_A is the thermal diffusivity of air. Therefore, compared to the thin water film, advective heat transport is more prevalent in the air boundary layer, and the flow of the warm air is more likely to be unstable. Most of the icicles in our experiments were grown under forced convection conditions, with a typical wind speed of $2 - 3$ m/s, which is much higher than u_p; the thickness of their boundary layer is likely to be smaller than that for icicles grown in still air [54].

Instead of accounting for the contributions from the various heat transfer mechanisms, as we did in Ch. 3, Short *et al.* used Fourier's law of heat conduction to approximate the heat flux across the air boundary layer:

$$J_A = \frac{\Lambda_A \Delta T_A}{\delta} = \frac{\Lambda_A \Delta T_A}{C\ell}\left(\frac{\ell}{z}\right)^{1/4}, \tag{4.3}$$

where Λ_A is the thermal conductivity of air. Then, they derived the normal growth speed of the icicle surface:

$$v_g = \frac{J_A}{L_f \rho_I} = v_c\left(\frac{\ell}{z}\right)^{1/4}, \quad v_c = \frac{\Lambda_A \Delta T_A}{L_f \rho_I C \ell}, \tag{4.4}$$

where L_f is the latent heat of fusion of water and ρ_I is the density of ice.

After enforcing in Eq. 4.4 the condition for uniformly translating shapes, i.e. $v_g = v_t \sin\theta$, where v_t is the tip growth speed and θ is as shown in Fig. 3.1, and rewriting trigonometric functions in terms of the slope of the icicle profile, they found the following ordinary differential equation for the ideal shape of icicles:

$$\frac{d\rho}{d\zeta} = \frac{1}{\sqrt{\zeta^{1/2} - 1}}, \tag{4.5}$$

where $\rho = R/a$, $\zeta = z/a$, and the common length scale factor is given by

$$a = \ell\left(\frac{v_c}{v_t}\right)^4 = \frac{g\beta_A(\Delta T_A)^5}{\nu_A^2}\left(\frac{\Lambda_A}{L_f \rho_I C v_t}\right)^4. \tag{4.6}$$

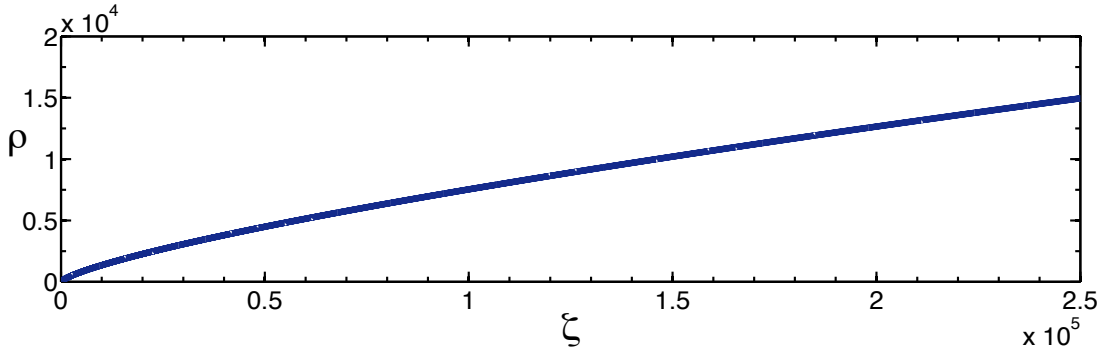

Figure 4.2: Theoretical prediction for the ideal icicle shape by Short *et al.* [26]. $\zeta \geq 1$ is the dimensionless vertical distance away from the tip; $\rho \geq 0$ is the dimensionless radius.

Eq. 4.5 can be solved exactly; its solution is

$$\rho(\zeta) = \frac{4}{3}\left(\zeta^{\frac{1}{2}} + 2\right)\sqrt{\zeta^{\frac{1}{2}} - 1}. \tag{4.7}$$

Since all the physical details were absorbed into a, Eq. 4.7 is free of any parameters; this implies there is a universality of shape amongst icicles. It is plotted in Fig. 4.2, which shows that the ideal icicle shape is slightly convex and hence distinct from that of a cone. This solution is predicted to be an attractor, i.e. all icicles should converge to this shape as they grow. For a given icicle, the value of a determines the scaling of the ideal shape that resembles its form. For large ζ, the predicted shape takes the form of a power law $\rho \sim \zeta^{3/4}$; in this sense, it is self-similar. Furthermore, Short *et al.* found that the shape of stalactites exhibits this same asymptotic power law [28, 29], even though the growth mechanisms of icicles and stalactites are vastly different; this explains the striking visual resemblance between the two. A critical assessment of the icicle shape theory by means of laboratory experiments is presented in the next three sections.

4.2 Preliminary observations

In this section, we discuss preliminary observations from our experiments on the shape of icicles. These are primarily based on data collected prior to the completion of the fully-controlled set-up described in Ch. 2. For example, in the earliest experiments, we

grew icicles from crushed ice that was packed inside a large heated funnel; thus, the input mass flux was uncontrolled. In another iteration of the apparatus, we made the feed water travel through several feet of coiled copper tubing immersed in an ice-water bath before it entered the icicle machine; this allowed us to partially control the input water temperature. In addition to wood, cotton was used as a substrate in some runs.

The theory by Short *et al.*, reviewed in Sec. 4.1, had previously been compared to eight images of natural icicles found on the Internet [26]. Here, we test it against 106 images of laboratory icicles grown from either distilled or Toronto tap water. Each picture is taken prior to cessation and features a different icicle. For consistency, all icicles analyzed here have a length of 25 ± 1 cm. Since the physical interpretation of a (Eq. 4.6) is somewhat obscure, we shall simply treat it as a theory-independent overall scale parameter in the fitting of lab-grown icicles.

Following the methods outlined in Sec. 3.3, we first detected the edge of each icicle and converted it into a profile $R(z)$. Then, using a Levenberg-Marquardt algorithm, we fit the profile to the theoretical prediction, Eq. 4.7, to extract the scaling factor a that gives the smallest reduced chi-squared. The reduced chi-squared is defined as

$$\chi^2_\nu = \frac{1}{\nu} \sum_{i=1}^{N} \frac{(\hat{R}_i - R_i)^2}{\sigma_i^2}, \tag{4.8}$$

where $\hat{R}_i$ is the fit estimate of the icicle radius, R_i is the actual icicle radius, $\sigma_i = 2$ pixels is the uncertainty associated with each measurement of R_i, N is the number of pixels corresponding to the icicle length, $\nu = N - n - 1$ is the number of degrees of freedom, and n is the number of fit parameters, which is 1 in our case.

Fig. 4.3(a) shows the best-fit a and the reduced chi-squared from fitting the 106 icicle profiles to Eq. 4.7. Since a is typically on the order of 10^{-5} to 10^{-3} cm, Eq. 4.7 reduces to its small-a limit $\rho(\zeta) = (4/3)\zeta^{3/4}$ away from the tip. In Fig. 4.4, we present data representative of the two extremes we observed; for the sake of fair comparison, we only chose from fits that gave a best-fit $a \sim \mathrm{O}(10^{-4}$ cm). Fig. 4.4(a) shows an average plot of five such icicles with the smallest χ^2_ν; Fig. 4.4(b) plots the five with the largest χ^2_ν. As seen in Fig. 4.4(a), some icicles fit the theoretical prediction to an impressive degree, at least

away from the tip where it is expected to hold. On the opposite extreme, Fig. 4.4(b) demonstrates that some icicles are poorly described by Eq. 4.7; these generally have more complex shapes that are clearly not self-similar. Most icicles exhibit a degree of agreement with the self-similarity theory that falls between these two extremes. In all cases, $\chi^2_\nu > 1$; this indicates the existence of real, systematic fluctuations of the icicle shape from the simplistic, smooth prediction shown in Fig. 4.2.

As a theory-independent model, we also tried a two-parameter fit of the unscaled icicle profile to an arbitrary power law $R = \alpha z^\beta$. Fig. 4.3(b) plots the best-fit exponents β against their corresponding reduced chi-squared. The mean χ^2_ν is 12 ± 1 in Fig. 4.3(b) and 22 ± 2 in Fig. 4.3(a). Thus, the arbitrary power law, as a purely empirical model, generally does better at describing the shape data than the full solution of the self-similarity theory. This is not surprising, since the former contains two parameters for fitting, while the latter only has one. Icicles that fit well to the power-law model scatters around $\beta = 0.5$; this suggests that the asymptotic 3/4 power law predicted by Short *et al.* [26] is not robust.

The quality of the fit to both models, as measured by χ^2_ν, has a clear dependence on the purity of the feed water. In Fig. 4.3(a), the mean χ^2_ν is 15 ± 2 for distilled water icicles and 37 ± 4 for tap water icicles. In Fig. 4.3(b), the mean χ^2_ν is 5 ± 1 for distilled water icicles and 28 ± 3 for tap water icicles. Their morphological differences are apparent from casual inspection. Fig. 4.5 shows time-lapse photographs of two icicles grown under identical conditions, except one was made from distilled water and the other from Toronto tap water. Tap water icicles tend to have bulgier upper bodies than their distilled counterparts, which are generally closer to the predicted monotonic shape. Tap water icicles also exhibit a much more prominent ripple pattern on their surface, the subject of Ch. 5. In fact, it was this observation that prompted us to conduct controlled experiments on saline water icicles. Moreover, tap water icicles are generally cloudier in appearance than distilled water icicles; this may reflect the presence of impurities in tap water, which can alter the water freezing process.

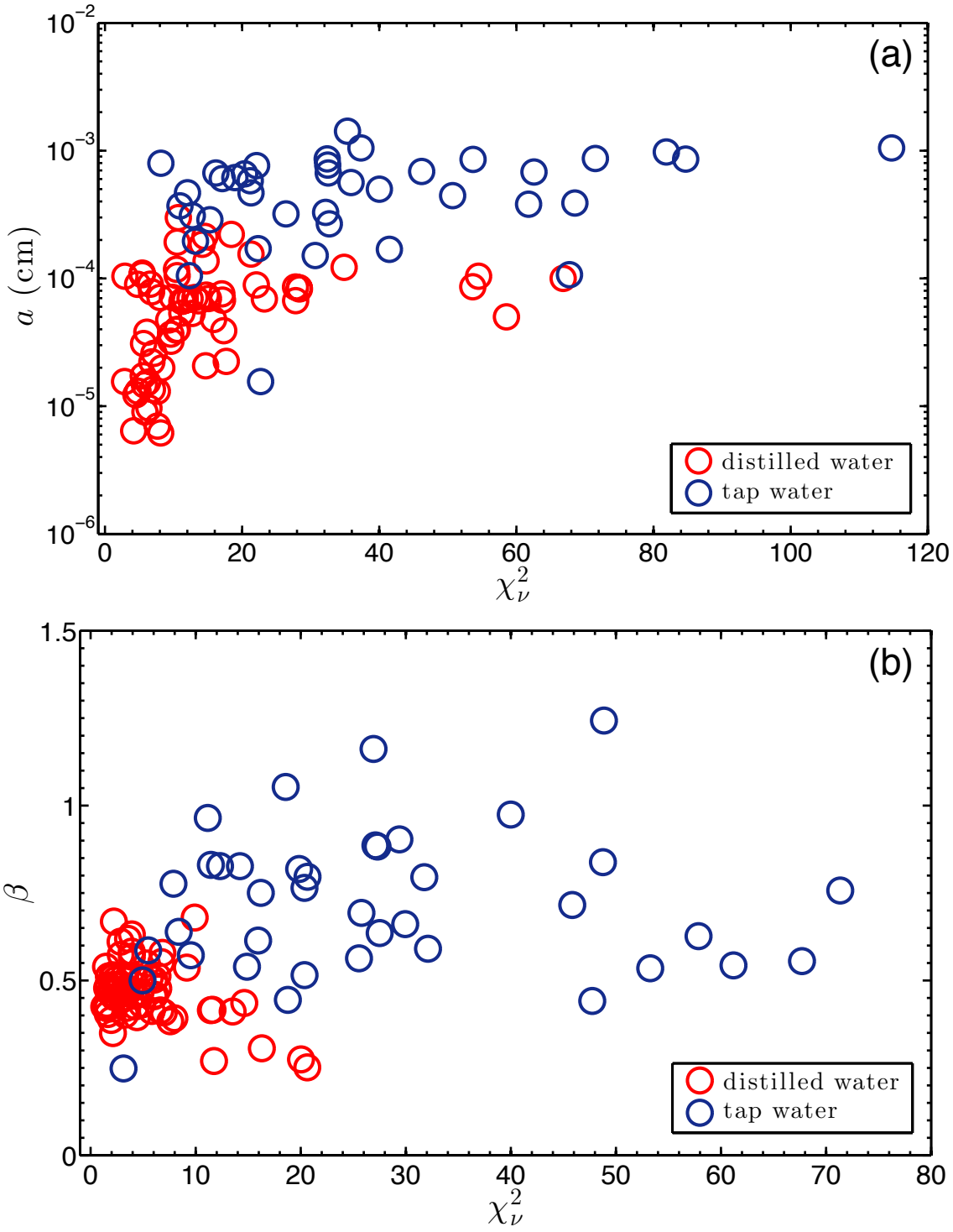

Figure 4.3: Results of fitting profiles of 106 laboratory icicles, made from either distilled or Toronto tap water, to: (a) Eq. 4.7, (b) an arbitrary power law $R = \alpha z^{\beta}$. Note the difference in the scales on the horizontal axes.

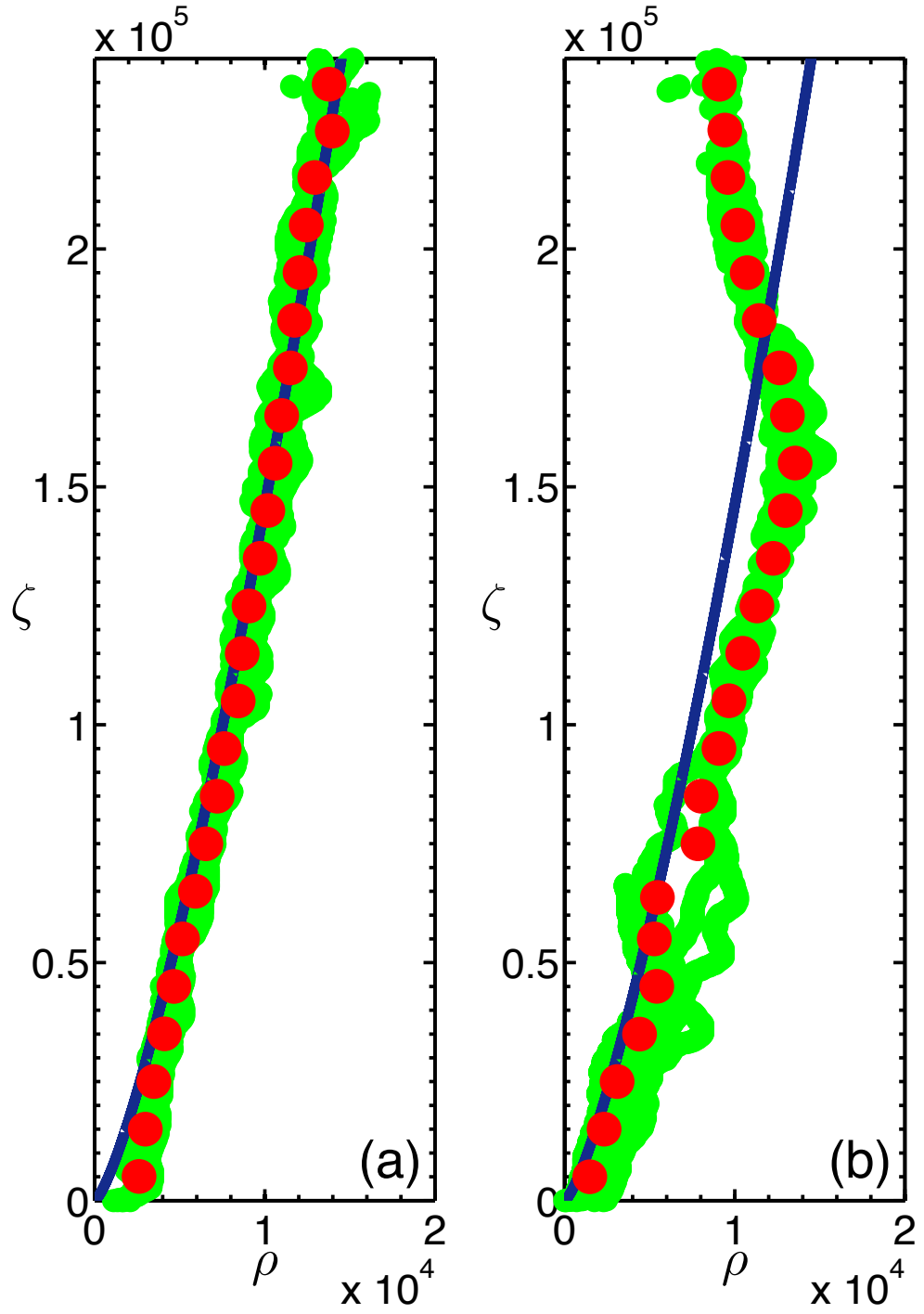

Figure 4.4: Average plots of the profiles of: (a) five icicles that fit best to the theoretical prediction, (b) five icicles that fit most poorly to the theoretical prediction. The green dots in the background are the raw data, the red dots in the foreground are the average data, and the blue curve indicates the theoretical prediction.

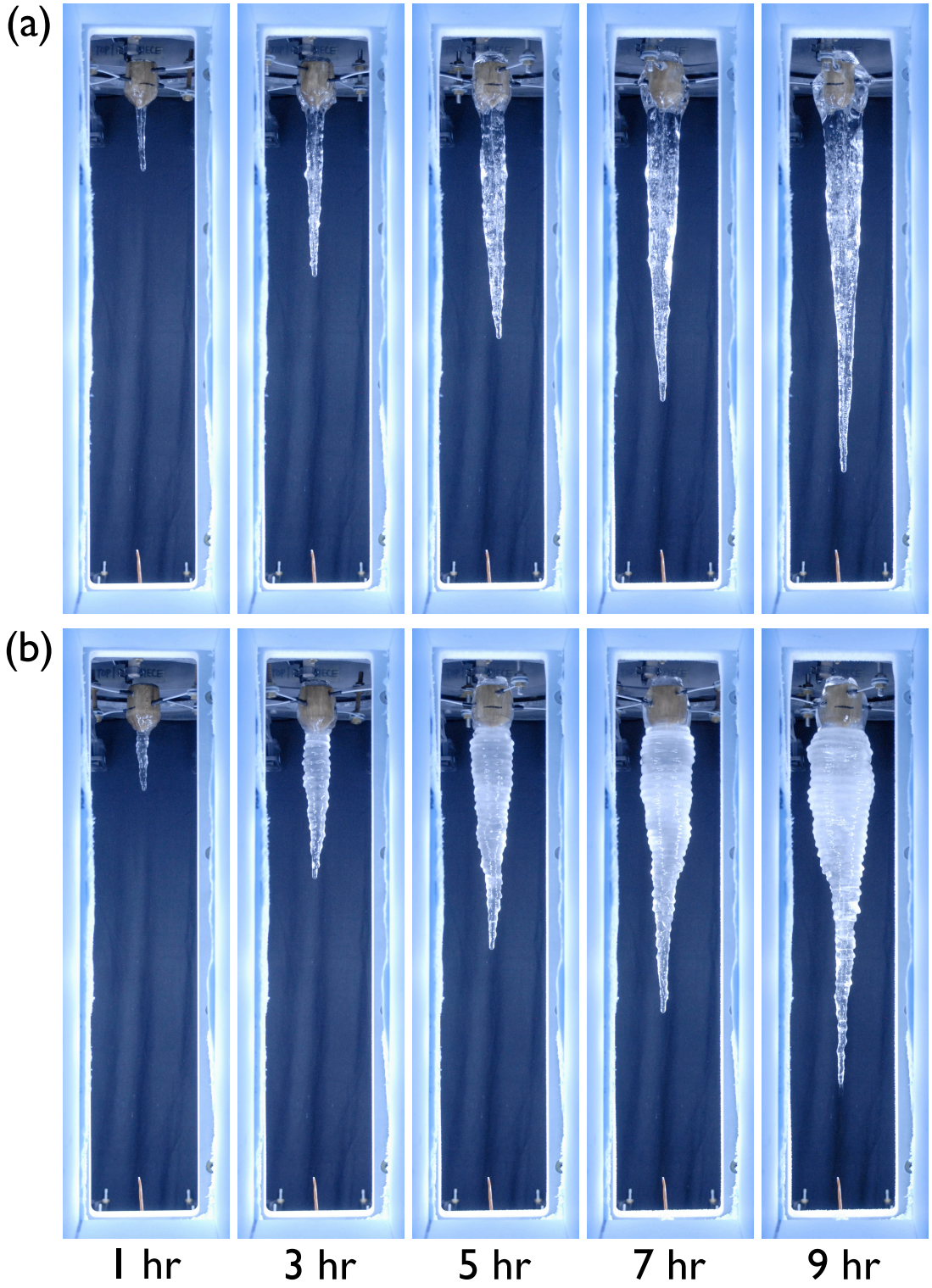

Figure 4.5: Photographic time-series of two icicles grown from different sources under otherwise identical conditions: (a) was made with distilled water; (b) was made with Toronto tap water. The temperature of the stirred air was −6.8 °C, the input mass flux was 2.6 g/min, and the input water temperature was 3.2 °C. The times shown are the times elapsed since the initiation of icicle growth.

4.3 Controlled experiments

In the previous section, observations from our preliminary, partially-controlled experiments were reported. We found that while some profiles of lab-grown icicles fit extremely well to the theoretical prediction of Short *et al.* [26], some deviated far from it. In particular, we noticed a correlation between the degree of agreement and the purity of the water supply. Moreover, for a given type of feed water, the reduced chi-squared from the fit spanned a wide range (Fig. 4.3(a)); this suggests there are other factors that affect how 'platonic' the icicle shape is. In this section, we dig deeper to investigate the time evolution of the icicle shape, its dependence on the impurity level of the feed water, and how it is affected by various extrinsic factors. The results here are based on time-series data collected from our fully-controlled experiments, done using the apparatus and methods described in Ch. 2.

As before, we performed edge detection on each icicle image to extract the profile $R(z)$, which was then fit to Eq. 4.7 via a least-squares analysis to determine the best-fit scaling factor a. Fig. 4.6(a)-(b) show typical pre-cessation time-series of the best-fit a and the reduced chi-squared from fitting profiles of distilled water icicles. $a(t)$ begins with an initial transient during which the predicted icicle shape is fit to a frozen droplet or a short ice tube; it is only after this period that a becomes relevant in the present context. After the transient, a maintains a relatively constant value, as one would expect, since every parameter in Eq. 4.6 is constant or approximately so prior to cessation. For uniformly advancing icicles, the reduced chi-squared from the fit does not vary much before cessation either. However, after cessation, the shapes of distilled water icicles deviate increasingly from the prediction of the self-similarity theory (Fig. 4.6(c)). For saline water icicles, this increasing deviation may begin well before cessation (Fig. 4.6(d)).

To examine the degree of agreement between theory and experiment under different conditions, we again picked out data corresponding to growing icicles with a length of 25 ± 1 cm. Within the parameter space we traversed, the quality of fit shows no systematic dependence on the ambient temperature (Fig. 4.7(a)), input water temperature (Fig. 4.7(c)), or surrounding air flux (Fig. 4.7(d)). It does, however, show a clear depen-

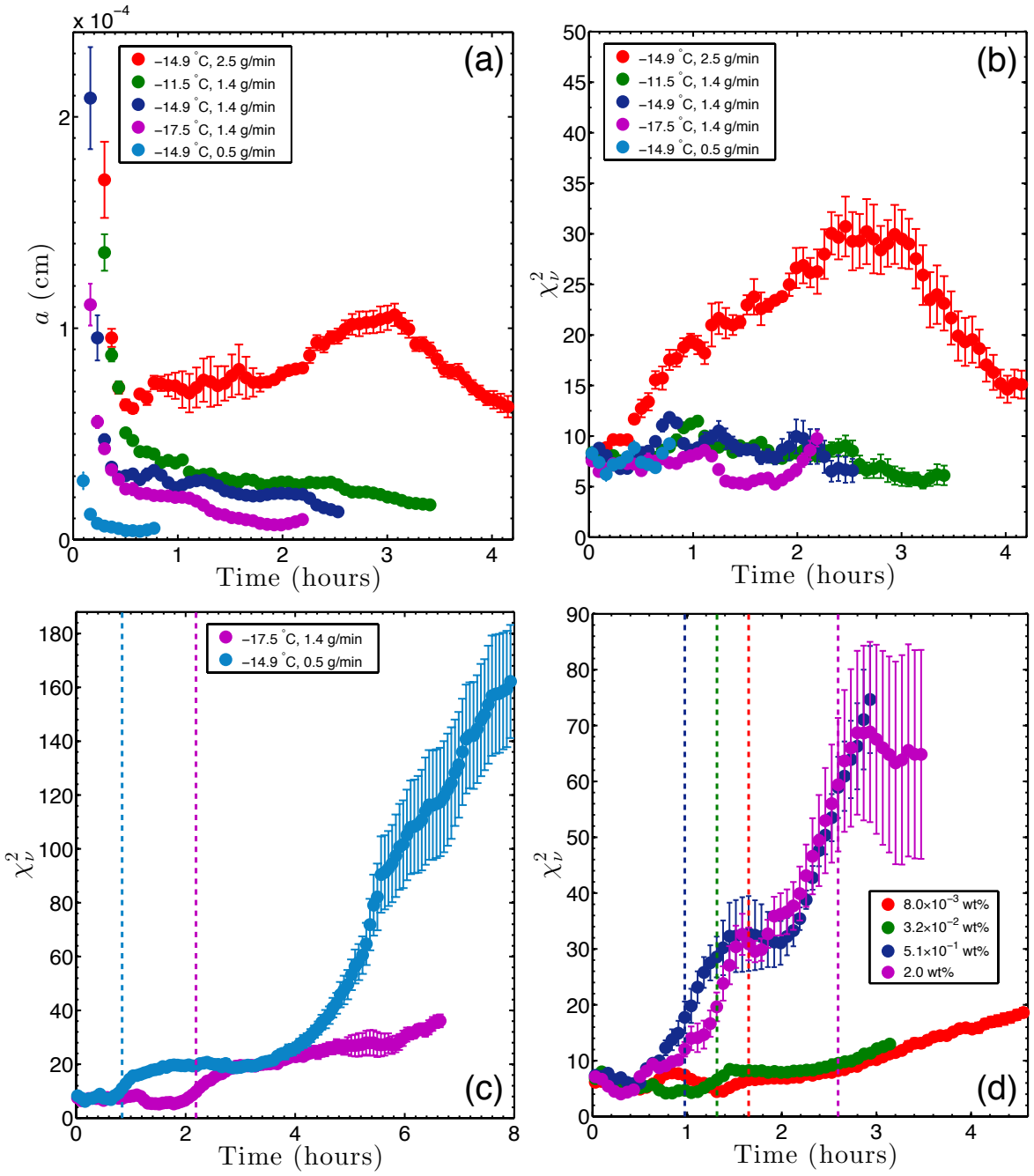

Figure 4.6: Time evolution of the (a) best-fit a and (b)-(d) χ^2_ν from the icicle shape fit. (a)-(c) are from fitting distilled water icicles: the colour-coded circles correspond to the same set of experiments; the legends show the ambient wall temperature and the water supply rate for each run; in all experiments, the input water temperature was 3.0 °C, and the surrounding air flux due to each fan was 0.95 m^3/min. (d) is from fitting saline water icicles: the legend shows the feed water salinity for each run; in all experiments, the ambient wall temperature was −15.0 °C, the water supply rate was 1.3 g/min, the input water temperature was 2.2 °C, and the surrounding air flux due to each fan was 1.05 m^3/min. (a)-(b) show pre-cessation data only. (c)-(d) include post-cessation data; each vertical dashed line marks the time of cessation for the time-series of the same colour. The error bars indicate the standard errors from averaging over each rotation.

	Value		**Value**
g	9.8 m/s^2	Λ_A	2.43×10^{-2} W/(m·K)
β_A	3.7×10^{-3} K^{-1}	L_f	3.34×10^5 J/kg
ν_A	1.3×10^{-5} m^2/s	ρ_I	0.917×10^3 kg/m^3

Table 4.2: Parameter values in shape scaling factor calculations.

dence on the input mass flux — the faster the water is supplied, the further the resultant icicle deviates from the theoretically predicted shape (Fig. 4.7(b)). The reduced chi-squared from the fit also rises above the norm for the highest feed water salinities, above 1 wt% (Fig. 4.8). This is qualitatively consistent with our earlier observation that tap water icicles generally had less 'platonic' shapes than distilled water icicles, though the impurity level in our tap water was only $\sim 10^{-2}$ wt% (Table 2.1). Fig. 4.9 shows visually how the icicle morphology changes with the water supply rate and the feed water salinity. As these parameters are increased, the shape deviates from not only self-similarity, but also axisymmetry.

Next, we compare the best-fit parameter a_{fit} with the theoretical prediction a_{theory}. The latter was calculated from Eq. 4.6, using the parameter values in Table 4.2, $C = 1$, and the measured ΔT_A and v_t for each run. Fig. 4.10 shows data for 106 distilled and saline water icicles grown in our controlled experiments under various conditions. Because a becomes more irrelevant as the icicle profile deviates further from the self-similarity theory, 9 icicles with $\chi^2_\nu > 30$ are excluded in this figure. While a_{fit} and a_{theory} are positively correlated, most theoretical values for the scaling factor are 2 to 3 orders of magnitude less than their actual values (Fig. 4.10(a)). Since the unspecified constant of order unity C in Eq. 4.6 is raised to the 4th power, setting $C = 0.2$ would bring a_{fit} and a_{theory} into agreement.

Finally, we determine how a depends on icicle growth speeds in our experiments. Eq. 4.6, from the theory of Short *et al.* [26], suggests there is a power-law relationship between a and the ratio of the lateral growth speed to the tip growth speed, i.e. $a = d(v_g/v_t)^p$, where d is a characteristic length scale and p is an exponent. Taking the log on both sides, we get $\log(a) = \log(d) + p\log(v_g/v_t)$. In Fig. 4.10(b), $\log(a_{\text{fit}})$ is plotted

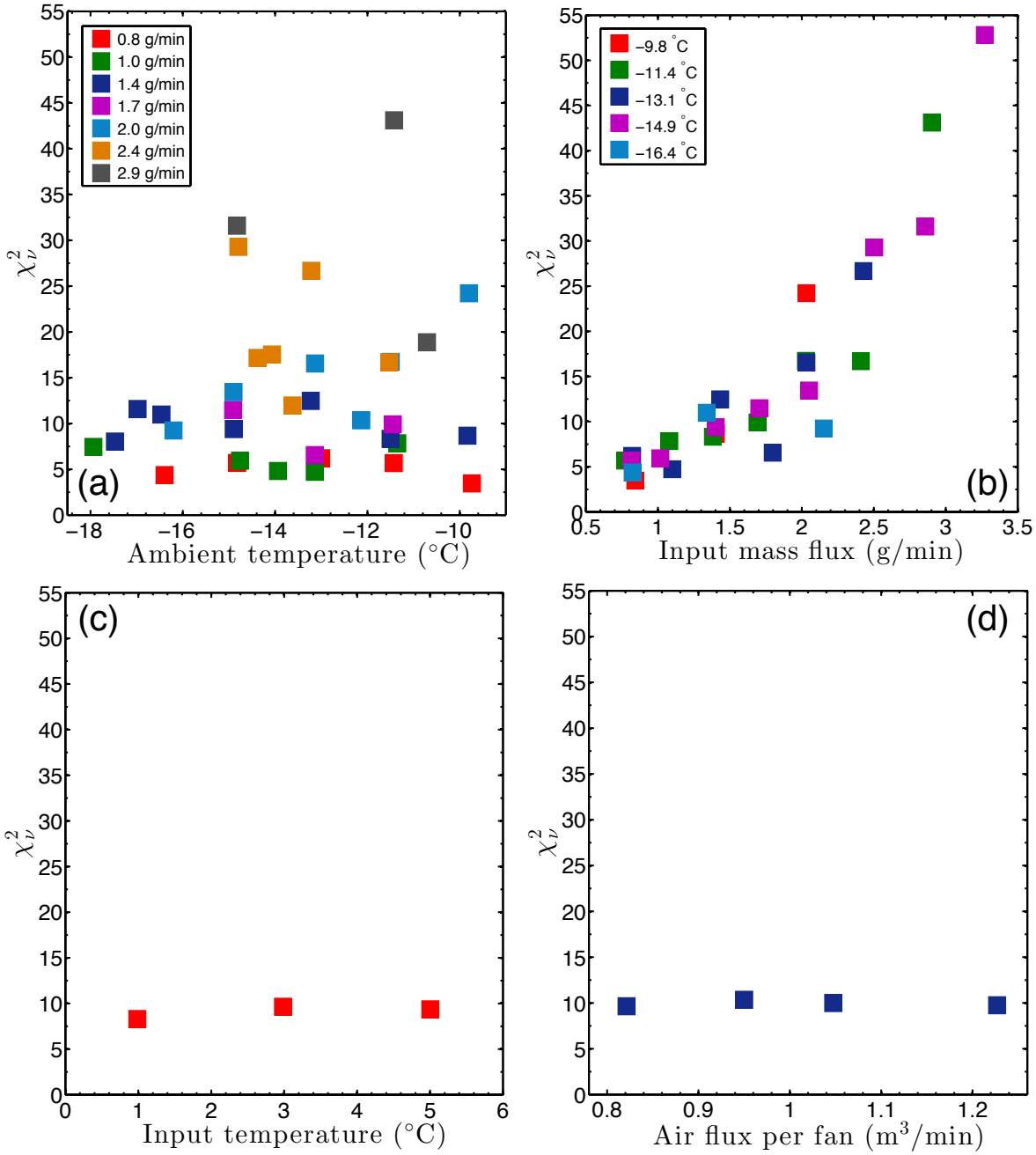

Figure 4.7: Deviation from the ideal icicle shape *vs.* extrinsic conditions. All results are from fitting distilled water icicles. The fixed variables in each panel are: (a) water supply rate (as shown in the legend), input water temperature (3.0 °C for all experiments), and air flux per fan (0.95 m^3/min for all experiments); (b) ambient wall temperature (as shown in the legend), input water temperature (3.0 °C for all experiments), and air flux per fan (0.95 m^3/min for all experiments); (c) ambient wall temperature (−12.1 °C for all experiments), water supply rate (2.0 g/min for all experiments), and air flux per fan (0.82 m^3/min for all experiments); (d) ambient wall temperature (−12.1 °C for all experiments), water supply rate (2.0 g/min for all experiments), and input water temperature (3.0 °C for all experiments). Each colour corresponds to one set of experiments with the same values of the fixed variables.

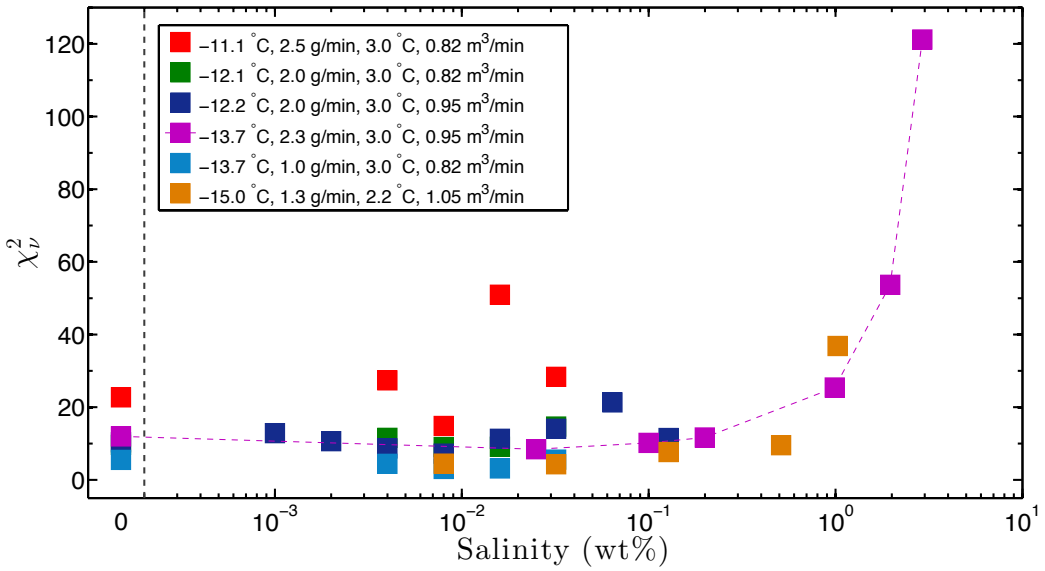

Figure 4.8: Deviation from the ideal icicle shape *vs.* feed water salinity. The fixed variables are: ambient wall temperature, water supply rate, input water temperature, and surrounding air flux due to each fan. Each colour corresponds to one set of experiments with the same values of the fixed variables. The legend shows the values of the fixed variables for each set of experiments. The vertical dashed line is a scale break, to the right of which salinity is plotted on a log scale.

against $\log(v_g/v_t)$, where a_{fit} is in centimetres, and v_g and v_t are taken to be the measured radial and tip growth speeds for each run. Indeed, a linear relationship is found, which is a strong test for the existence of a power law. The best-fit line through this data has a slope of 2.4 and a y-intercept of -0.95. Thus, the exponent $p = 2.4$, and the characteristic length $d = 1.1 \times 10^{-3}$ m, which is roughly the thickness of the thermal boundary layer around the icicle, calculated in Sec. 4.1. In contrast, Eq. 4.6 gives $p = 4$ and $d = z$, the vertical distance away from the tip. This disagreement between theory and experiment is further evidence that the scaling model of Short *et al.* [26] is not robust.

4.4 Non-ideal features

A fraction of our lab-grown icicles exhibited non-ideal features which were sufficiently pronounced that their shapes could not be reasonably described by the self-similarity theory.

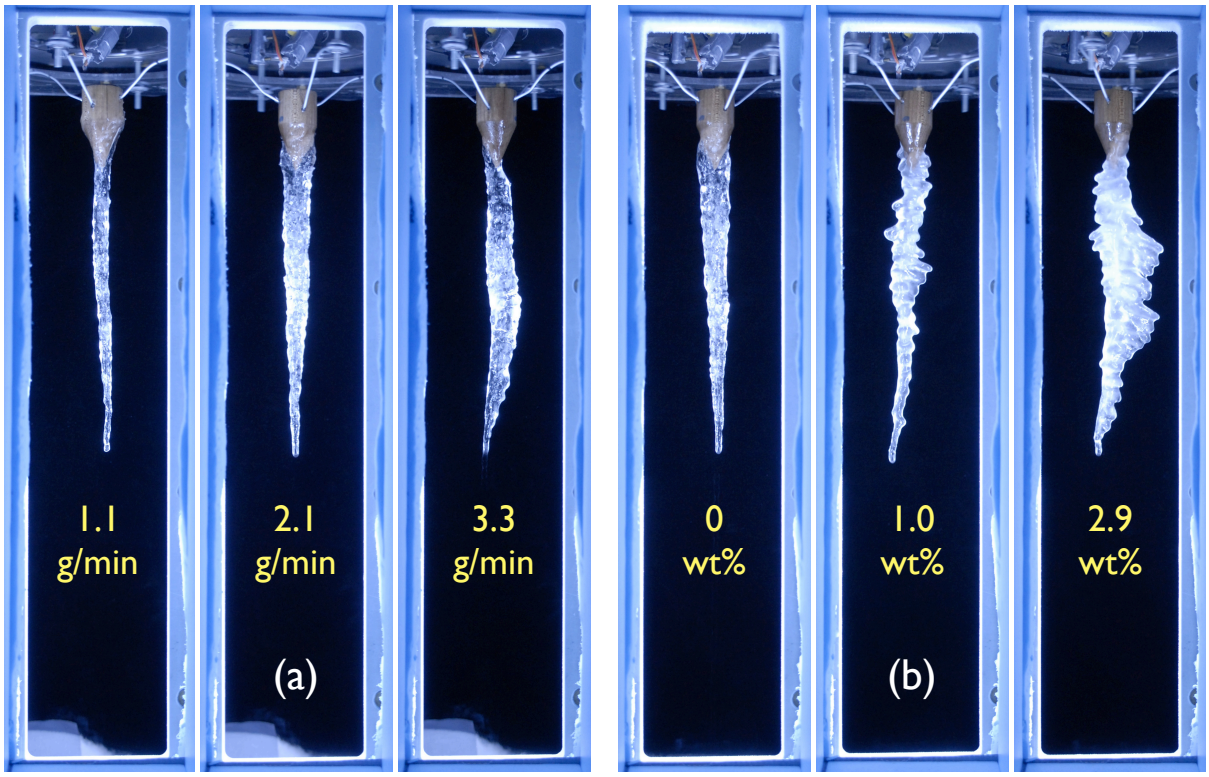

Figure 4.9: Icicle morphology *vs.* (a) water supply rate and (b) feed water salinity. The icicles in (a) were made from distilled water; the ambient wall temperature was −14.9 °C. For the icicles in (b), the ambient wall temperature was −13.7 °C, and the water supply rate was 2.3 g/min. In all experiments, the input water temperature was 3.0 °C, and the surrounding air flux due to each fan was 0.95 m^3/min.

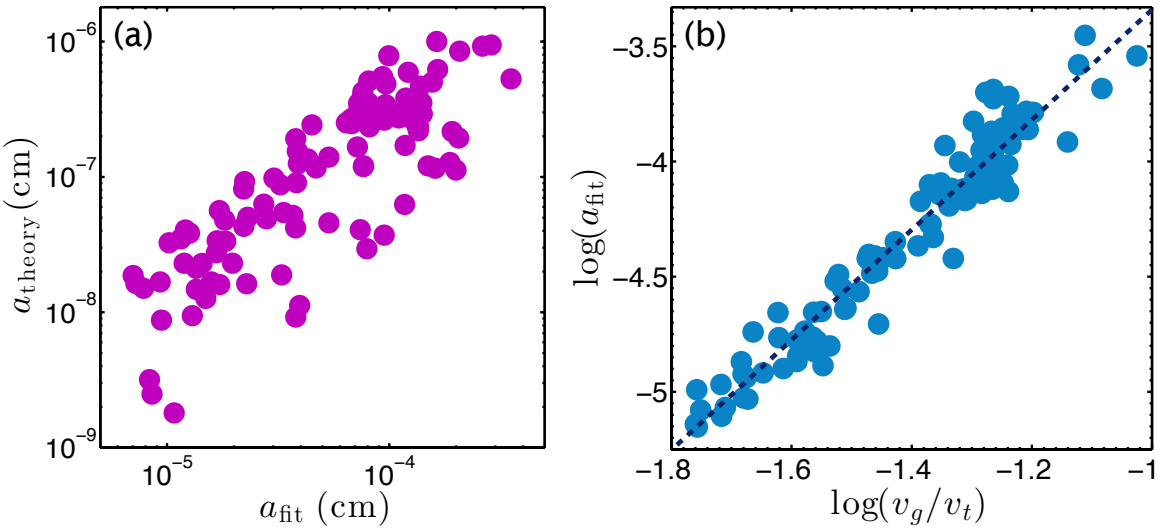

Figure 4.10: Experimental *vs.* theoretical values of the shape scaling factor. In (b), $a_{\rm fit}$ is in cm, and the dashed line is the best-fit line.

For example, icicles can twist (Fig. 4.11(a)) due to a vigorous, repetitive flow of the surrounding air. These are distinct from icicles that bend (Fig. 4.11(b)), another type of deviation from axisymmetry. Bent icicles are caused by irregular, non-axisymmetric water distribution or wind effects. We found that icicles tend to bend towards the side on which the feed water flows down. Past experiments by Maeno *et al.* [30, 31] showed that icicles bend towards the leeward direction, and the angle of deviation from the vertical increases with the speed of the wind. Bending and twisting were frequently observed in early iterations of our experiments, which had a non-rotating icicle support and strong, asymmetric air-stirring. These effects were minimized in the final design of the apparatus, described in Ch. 2, by placing the fans in a symmetric configuration and limiting their speed, as well as rotating the support and positioning the feed water nozzle slightly off-axis from it to encourage even water distribution.

Thin, needle-like spikes were sometimes seen to extend from the icicle surface in random directions, but only after the cessation of its growth. As discussed in Sec. 3.6, the thin water film on the icicle surface begins to freeze from the bottom up after cessation (Fig. 3.16). If any water is trapped under ice, the pressure from its expansion as it freezes can push it out through small gaps in the ice; once the water is ejected, it may freeze rapidly to form a spike [30, 31]. The spike circled in Fig. 4.11(c) is about 1 cm long and 1 mm wide. To allow icicles with such spikes to be included in the data analysis, we added a de-spiking operation to our edge-tracing algorithm: the horizontal edge coordinate at a given height was ignored if it deviated more than 3 mm, i.e. about 16 pixels, from that identified in the row one pixel above it.

An unexpected but not uncommon non-ideal feature of our lab-grown icicles was multiple tips (Fig. 4.11(d)-(e)). It is the result of a branching process, which begins with the formation of a small protrusion on the surface of an icicle, usually within a couple of centimetres above the tip and at an angle between 0 and 90° from the downward axis. Once the protrusion becomes a secondary source of pendant drops falling from the icicle, an icicle with multiple tips will form. Each of the tips continues to grow as they share the incoming water supply. Fig. 4.11(f) shows the typical evolution for the initiation of a multi-tipped icicle.

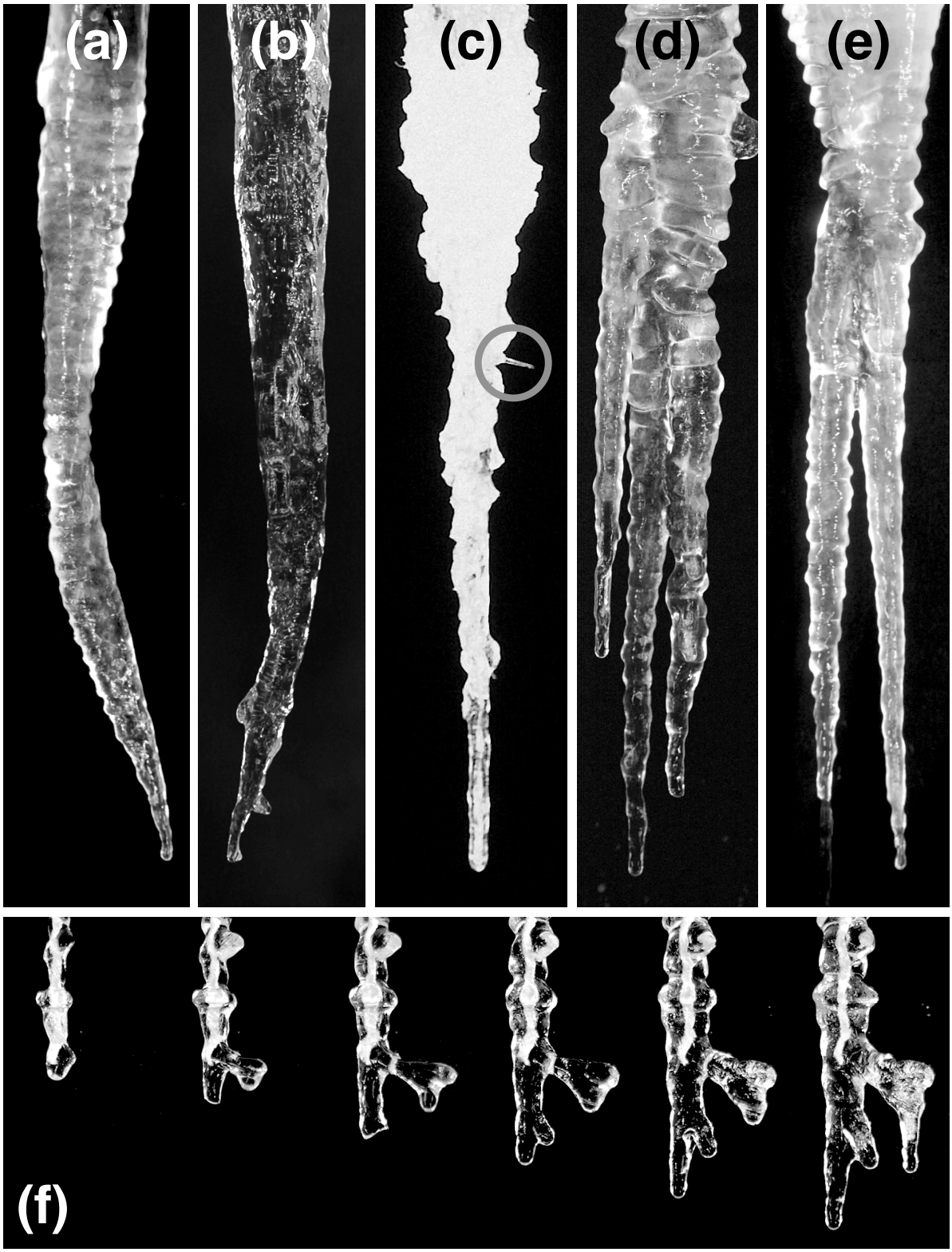

Figure 4.11: Non-ideal features of lab-grown icicles: (a) is a twisted icicle; (b) is a bent icicle; (c) shows an icicle with a thin spike extending from its surface; (d)-(e) are multi-tipped icicles; (f) shows time-series photographs of the initiation of a multi-tipped icicle grown on a piece of string (time interval: 10 min).

Of the 250 icicles we grew under various conditions, 56 had multiple tips. The presence or absence of air motion around the growing icicle was strongly correlated with the probability that branches will develop. Of the 22 runs conducted with the air-circulating fans off, multiple tips were observed in 15 runs (i.e. 68 %); of the 228 icicles grown when the air was stirred, multiple tips were observed in 41 runs (i.e. 18 %). Considering only the runs for which the fans were turned on, the addition of impurities to the feed water increased the likelihood of branching. In windy conditions, only 3 of the 73 distilled water icicles (i.e. 4 %) grew multiple tips, while 38 of the 155 impure water icicles (i.e. 25 %) grew multiple tips. Multiple tips formed on 71 % of the impure water icicles grown in still air. As will be discussed in Ch. 5, the presence of impurities in the feed water can encourage the formation of protrusions on the icicle surface and hence increase the probability of branching. A theoretical explanation for the correlation between the branching of icicles and their surrounding air motion remains to be formulated.

This concludes the chapter on the global shape of icicles, in which we tested the self-similarity theory of Short *et al.* [26] against experimental data. Icicles grown in still air had a high probability of forming multiple tips; this contradicts the natural convection assumption of the theory. Even under forced convection conditions, the profiles of most laboratory icicles deviated significantly from the theoretically predicted shape. The degree of deviation increased with the input rate and impurity level of the feed water. The emergence of ripples, which also contributed to deviation from the self-similar shape, is the subject of the next chapter.

Chapter 5

Rippling instability

The second law of thermodynamics dictates that the entropy of an isolated system never decreases [55, 56]. Yet, from the periodic wind-blown sand ripples in deserts, to the complex, intricate patterns of snowflakes, to the spots on leopards and the stripes on zebras, self-organizing systems that evolve towards order are ubiquitous in Nature [57–60]. It is not that the second law is violated, but these pattern-forming systems are not isolated. Energy flow in and out of a system allows it to lower its entropy [55, 56]. An icicle, too, is an open system. During the non-equilibrium growth of icicles, water is continually supplied to their roots and dripped off from their tips, and latent heat is transferred from the icicle to its surrounding air and drip-off water. The emergence of "Michelin Man"-like ripples on the surface of icicles (Fig. 1.1(b)) is an example of pattern formation and the focus of this chapter.

Icicle ripples are due to a morphological instability that is not contained in the growth models outlined in Ch. 3 or the self-similarity theory discussed in Ch. 4. However, they have been investigated by linear stability theory [33–39] and laboratory experiments [38,40]. All past ripple measurements were made on either natural icicles [9,30,40] or laboratory icicles grown from an unspecified water source [38, 40]. In their growth experiments on distilled water icicles, Maeno *et al.* [30] mentioned it was "difficult" to produce ripply ones. In their growth experiments on marine icicles, Chung *et al.* [16] commented on the "pronounced ribs" being a characteristic that distinguished saline water icicles from pure water ones. Here, we report on our experimental study of icicle rip-

ples, which is the largest and most controlled one to date, and the first to systematically explore the role of added ionic impurities in the instability.

This chapter has three sections. In Sec. 5.1, we explain how we analyze our data on icicle ripples and discuss preliminary observations from our partially-controlled experiments. These observations motivate our fully-controlled experiments, the results of which are presented in Sec. 5.2. In Sec. 5.3, we review existing theoretical analyses of icicle ripples and compare our data with their predictions. We find that the ripple pattern commonly seen on natural icicles is rarely observed on lab-grown icicles made from distilled water. Contrary to theoretical expectations, the addition of non-ionic surfactant to the feed water, which reduces its surface tension, does not produce growing ripples. Instead, growing ripples emerge on icicles made from water with a sufficient amount of dissolved ionic impurities. Based on our experimental findings, we propose fundamental ways in which existing theories on the rippling instability of icicles should be modified.

5.1 Preliminary observations

In this section, we discuss observations of icicle ripples that were made during our preliminary experiments on the morphology of icicles, conducted prior to the completion of the fully-controlled set-up described in Ch. 2. In Sec. 4.2, we noticed that compared to distilled water icicles, tap water icicles exhibited a much more prominent ripple pattern on their surface (Fig. 4.5). A particularly good sample of such ripples was found on a long finger of ice that fortuitously formed when the drain of the refrigerated box froze. A cylindrical finger grew from the bottom upward and bridged the whole height of the apparatus. The rotation of the icicle support was turned off. As the tap water continued to flow down the exterior of the finger, an extensive pattern of ripples was formed. Fig. 5.1 shows photographic time-series of the ice finger.

To visualize the evolution of the ripples more clearly, we applied the image processing algorithm outlined in Sec. 3.3 to the time-series photographs, and we filtered the $x(y)$ data (Fig. 3.2(c)) for each edge to get the ripple positions $x_{\mathrm{rip}}(y)$. The filtering consisted of subtracting a background shape, which was obtained by smoothing $x(y)$ using a moving

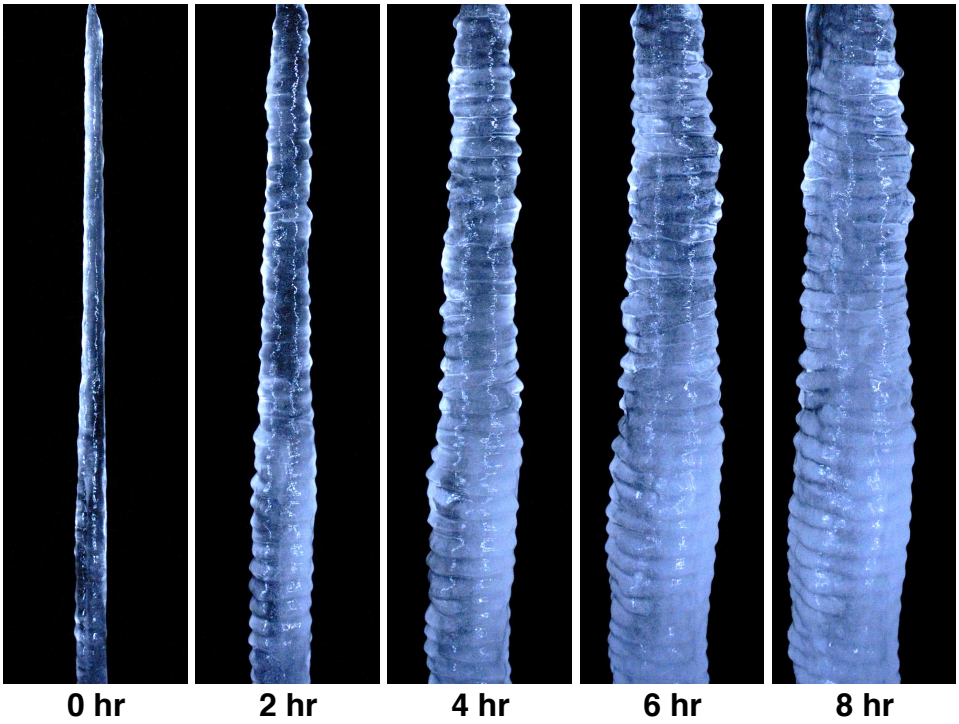

Figure 5.1: Photographic time-series of a tap water ice finger, 33 cm long. The surrounding air was gently stirred by fans and had a temperature of −10.4 °C.

average with a span of $y = 1$ cm. The filter de-emphasized topographical features, such as the bulges in Fig. 4.5(b), that had longer length scales than typical ripples, which have been shown previously [9, 30, 38, 40] to have wavelengths near 1 cm. This choice of de-trending filter is also consistent with the wavelengths of all the prominent ripple patterns observed on the lab-grown icicles in the present study. Fig. 5.2 shows a space-time plot of $x_{\mathrm{rip}}(y)$ for the left edge of the ice finger in Fig. 5.1. Like natural icicles [9,30,40], these ripples had a wavelength of approximately 1 cm. They climbed the ice at a speed of millimetres per hour during growth, in qualitative agreement with the prediction by Ueno *et al.* [34–39]. The upward motion was sometimes locally interrupted by the appearance of new ripples, ripple mergers, and other dynamics.

Next, we applied the same ripple extraction operations to growing icicles. Fig. 5.3 shows the $x(y)$ and $x_{\mathrm{rip}}(y)$ for the left edges of two lab-grown icicles, one made from distilled water and the other from tap water. To characterize their ripples, we took the Fourier transform of the spatial series $x_{\mathrm{rip}}(y)$ for the top 10 cm of the left and

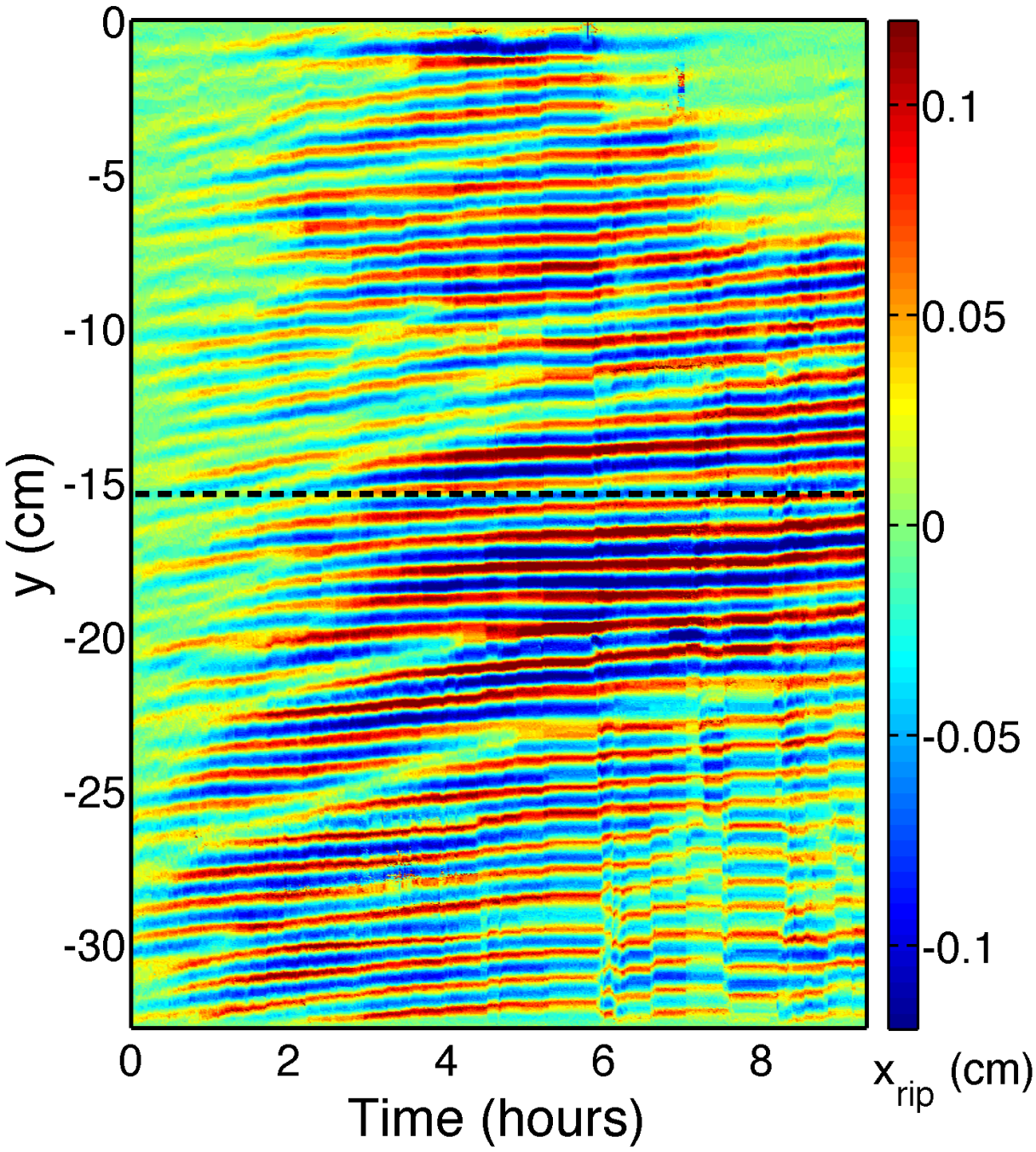

Figure 5.2: Space-time plot of the ripples along the left edge of the ice finger in Fig. 5.1. x_{rip}, indicated by the colour, is plotted as a function of y and time, where y is 0 at the top of the finger and decreases towards the bottom. The dashed line is a horizontal reference and shows that the centimetre-scale ripples moved slightly upward during growth.

right edges, spliced together peak-to-peak. The rightmost plots in Fig. 5.3 show the resulting power spectra. We defined the ripple amplitude A as the value of the maximum amplitude in the spectrum, with a small offset subtracted. The offset was determined from fitting a Lorentzian function plus a positive constant parameter to the spectral data through the point of the maximum amplitude. We defined the ripple wavelength λ as that corresponding to the point of the maximum amplitude; its error was given by the half-width at half maximum of the Lorentzian fit. This analysis gives the amplitude and wavelength of the most dominant Fourier mode of the ripple pattern. Isolated bumps on the icicle surface with a length scale comparable to that of ripples may contribute to the power of the peak. Since distilled water icicles are not perfectly smooth, they still have a broad but weak Fourier spectrum after de-trending.

We considered only ripples in the uppermost 10 cm, because ripples farther down had had less time to grow and may grow under more impure conditions due to the exclusion of impurities by ice formation higher up. As mentioned in Sec. 3.3, the resolution of our digital images was typically around 0.018 cm per pixel; thus, to detect the edge of one side of a 10 cm segment of the icicle required about 550 measurements. Since we determined the ripple amplitude and wavelength using both the left and right edges, the ripple analysis of a single image was based on about 1100 edge detection measurements. The entire algorithm for the extraction and analysis of ripples had been tested on simulated icicle images with a resolution comparable to that of actual data; two examples of these tests are shown in Fig. 5.4. The algorithm yielded the correct known ripple amplitudes and wavelengths of the simulated icicles. The image resolution was not a limiting factor for the ripple measurement.

We also tested the algorithm on simulated data of an icicle with a random noise (Fig. 5.5). Again, the de-trending filter took out topographical features with length scales greater than 1 cm. Even though no ripples were present on this icicle, the Fourier spectrum of its de-trended edge data exhibited a peak with an amplitude of nearly half a pixel close to $\lambda = 1$ cm; this was due to random deviations from the background shape of the icicle. Taking such systematic fluctuations into consideration, a reasonable floor for resolving the ripple amplitude is approximately 1 pixel. Therefore, in the subsequent dis-

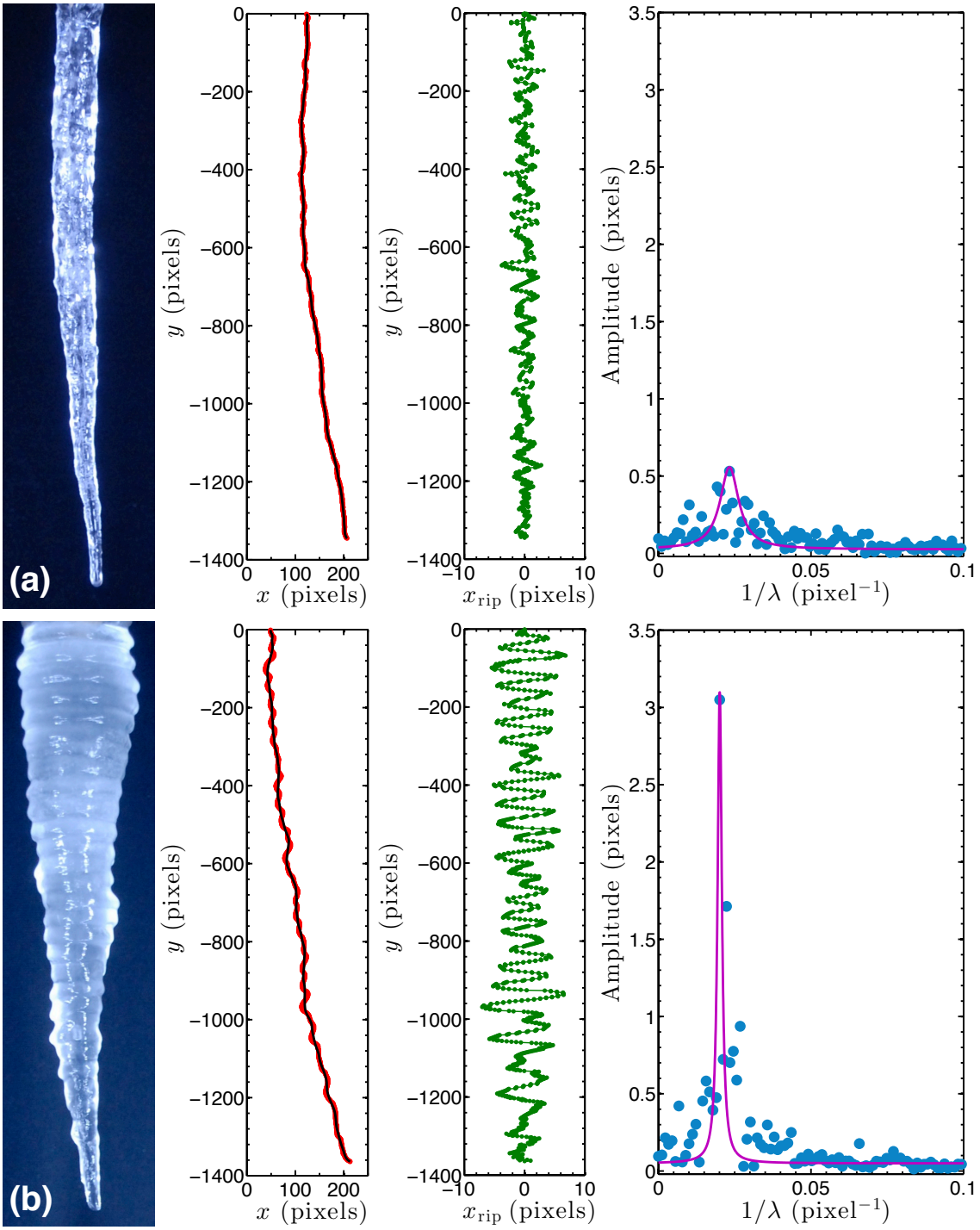

Figure 5.3: Ripple extraction and analysis of actual icicle data: (a) is a distilled water icicle; (b) is a tap water icicle. From left to right: the icicle image; the detected left edge (red) and its background shape (black); the ripple coordinates for the left edge (green); the Fourier spectrum of the ripple coordinates for the top 10 cm of the left and right edges, spliced together peak-to-peak (cyan). The magenta curve in the rightmost plot is a Lorentzian fit through the point of the maximum amplitude. Results of the analysis: (a) $A = 0.5$ pixels, $\lambda = 43 \pm 7$ pixels; (b) $A = 3.0$ pixels, $\lambda = 50 \pm 2$ pixels.

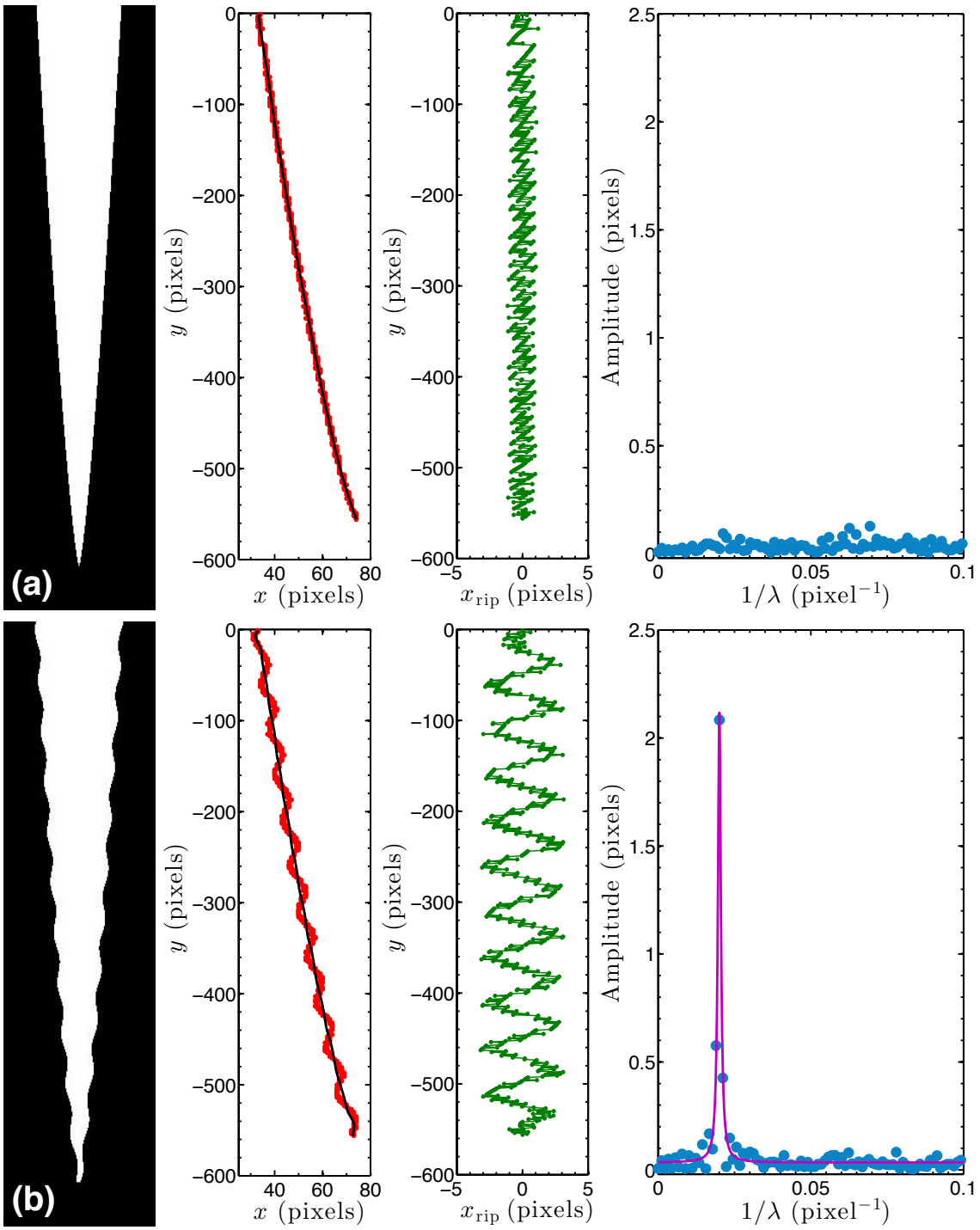

Figure 5.4: Ripple extraction and analysis of simulated icicle data. Each simulated icicle has a length of 556 pixels, i.e. 10 cm with our typical image resolution of 0.018 cm/pixel. (a) is Eq. 4.7 with $a = 10^{-4}$ cm; (b) is (a) plus a sine wave with an amplitude of 2 pixels, a wavelength of 50 pixels, and a random phase. From left to right: the icicle image; the detected left edge (red) and its background shape (black); the ripple coordinates for the left edge (green); the Fourier spectrum of the ripple coordinates for the left and right edges, spliced together peak-to-peak (cyan). The magenta curve in the rightmost plot of (b) is a Lorentzian fit through the point of the maximum amplitude; the analysis accurately gives $A = 2.0$ pixels and $\lambda = 50 \pm 1$ pixels.

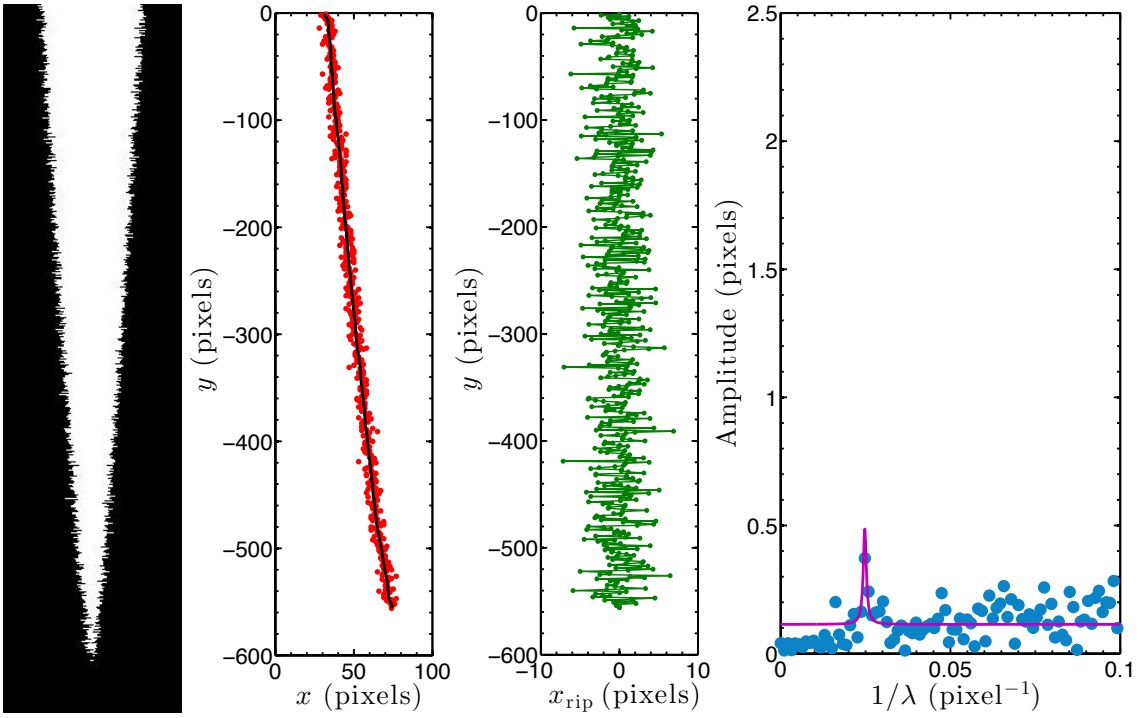

Figure 5.5: Ripple extraction and analysis of simulated icicle data with a random noise. Its shape is Fig. 5.4(a) plus normally-distributed random fluctuations, with a mean of 0 and a variance of 2 pixels, along the length of the icicle; it has no ripples.

cussion, we refer to measurable ripples as those with an amplitude greater than 0.02 cm. We are mainly interested in ripple patterns that have amplitudes significantly above this detection limit.

Fig. 5.6 shows the results of the ripple analysis performed on images of 106 laboratory icicles, grown from either distilled or tap water under various conditions. The measured wavelength was typically close to 1 cm, regardless of feed water type. The wavelength of the lowest-amplitude data tended to deviate from 1 cm, because the point of the maximum amplitude in the Fourier spectrum was close to the noise floor. The wavelength of higher-amplitude data could also exceed 1 cm, if the filtered icicle topography still contained features that had longer length scales and were more prominent than ripples. In agreement with direct observation (Fig. 4.5), distilled water icicles had no or barely measurable ripples. If ripples were detected on distilled water icicles, they generally had much smaller amplitudes than the ripples on tap water icicles. In Fig. 5.6, the

mean of the amplitude measurements is 0.014 ± 0.004 cm for distilled water icicles and 0.032 ± 0.014 cm for tap water icicles.

According to Ueno *et al.* [34–39], surface tension effects at the liquid-air interface, neglected in the self-similar shape theory [26], play an important role in the rippling instability of icicles. Their theory, which will be reviewed in Sec. 5.3, predicts that ripples grow faster on icicles made from feed water with lower surface tensions. As discussed in Sec. 2.3, we measured the surface tension of our distilled and tap water using the capillary tube method. The distilled water had a surface tension of 0.0718 ± 0.0003 N/m, while the tap water had a surface tension of 0.0709 ± 0.0003 N/m. Therefore, our direct observation that tap water icicles exhibit more prominent ripples than distilled water icicles is not qualitatively inconsistent with the theory of Ueno *et al.* However, the difference between the surface tension of distilled and tap water seems too small to account for this observation.

We also measured the compositions and conductivities of our water samples. The impurity level of the tap water was much higher than that of the distilled water (Table 2.1). Furthermore, we collected and analyzed melted snow that eventually produced ripply natural icicles. Its conductivity was 30 μS/cm. The metals with the highest concentrations were calcium (2.42 mg/L) and sodium (1.83 mg/L), and the anion with the highest concentration was chloride (3.56 mg/L). Overall, the melted snow had a higher impurity level than distilled water but was purer than Toronto tap water (Table 2.1). Therefore, it is possible that the amount of dissolved ionic impurities in the feed water is linked to the ripple amplification on icicles. Another potential trigger of the rippling instability is dissolved gases, which are presumably abundant in both tap water and melted snow. In the next section, we systematically investigate how surface tension, dissolved ionic impurities, and dissolved gases are correlated with the growth of icicle ripples.

5.2 Controlled experiments

In the previous section, observations from our preliminary, partially-controlled experiments were described. The main finding was that distilled water icicles had no or barely

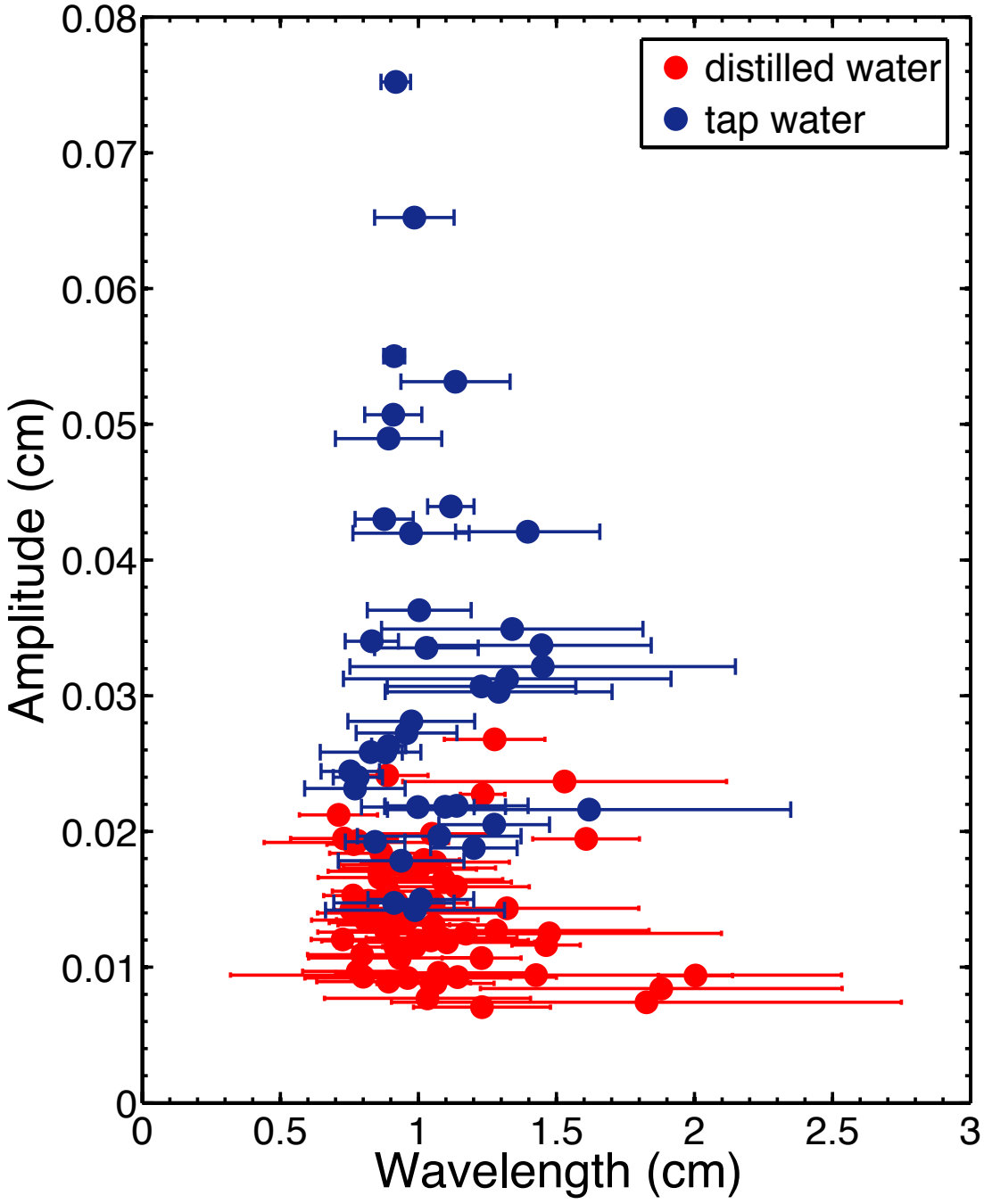

Figure 5.6: Results of the ripple analysis for 106 laboratory icicles, made from either distilled or Toronto tap water under various conditions.

measurable ripples, while most tap water icicles had prominent ripples with amplitudes considerably above their resolution limit. The theory of Ueno *et al.* [34–39] claims that the ripple growth is related to surface tension effects. However, it is also possible that the rippling instability is dependent on the amount of dissolved ionic impurities or gases in the feed water. In this section, we report results from our fully-controlled experiments, in which we systematically studied the dependence of the characteristics of icicle ripples on feed water properties, as well as other control parameters. Comparison with existing theories will be made in Sec. 5.3.

First, we focus on comparing icicles made from feed water with different compositions, grown under otherwise identical conditions: an ambient wall temperature of -12.3 ± 0.2 °C, a water supply rate of 2.0 g/min, an input water temperature of 3.0 ± 0.3 °C, and a volumetric air flux of 0.95 ± 0.03 m^3/min per fan. Fig. 5.7 displays three such icicles made from distilled water plus varying amounts of NaCl. Even from direct inspection, there are notable differences between them. The distilled water icicle is close to the self-similar shape discussed in Ch. 4 and has a relatively smooth surface. When a sufficient amount of salt is added to the water supply, clear ripples emerge on the surface of the icicle, and its overall form deviates from self-similarity and possibly also axisymmetry. As the feed water salinity is increased, the shape of the resultant icicle becomes more distorted, and its ripples become less sinusoidal.

Fig. 5.8 shows space-time plots of the ripple topography for the right edges of these three icicles; the evolution of $x_{\mathrm{rip}}(y)$ is plotted for a fixed rotational position. While some small topographical features are found on the distilled water icicle, the two saline water icicles exhibit a much more pronounced and extensive pattern of ripples, which appear in a patchy way and sometimes grow quickly to a saturated amplitude. The largest features on the saltiest icicle grow to a few millimetres in amplitude. Slow upward ripple motion, which was previously observed on the ice finger (Fig. 5.2), can be seen in parts of the ripple patches.

Fig. 5.9 shows the time evolution of the ripple amplitude and wavelength for icicles made from feed water with varying salinity. These were obtained for each image using the same methods as described in Sec. 5.1. Here, time zero corresponds to the time

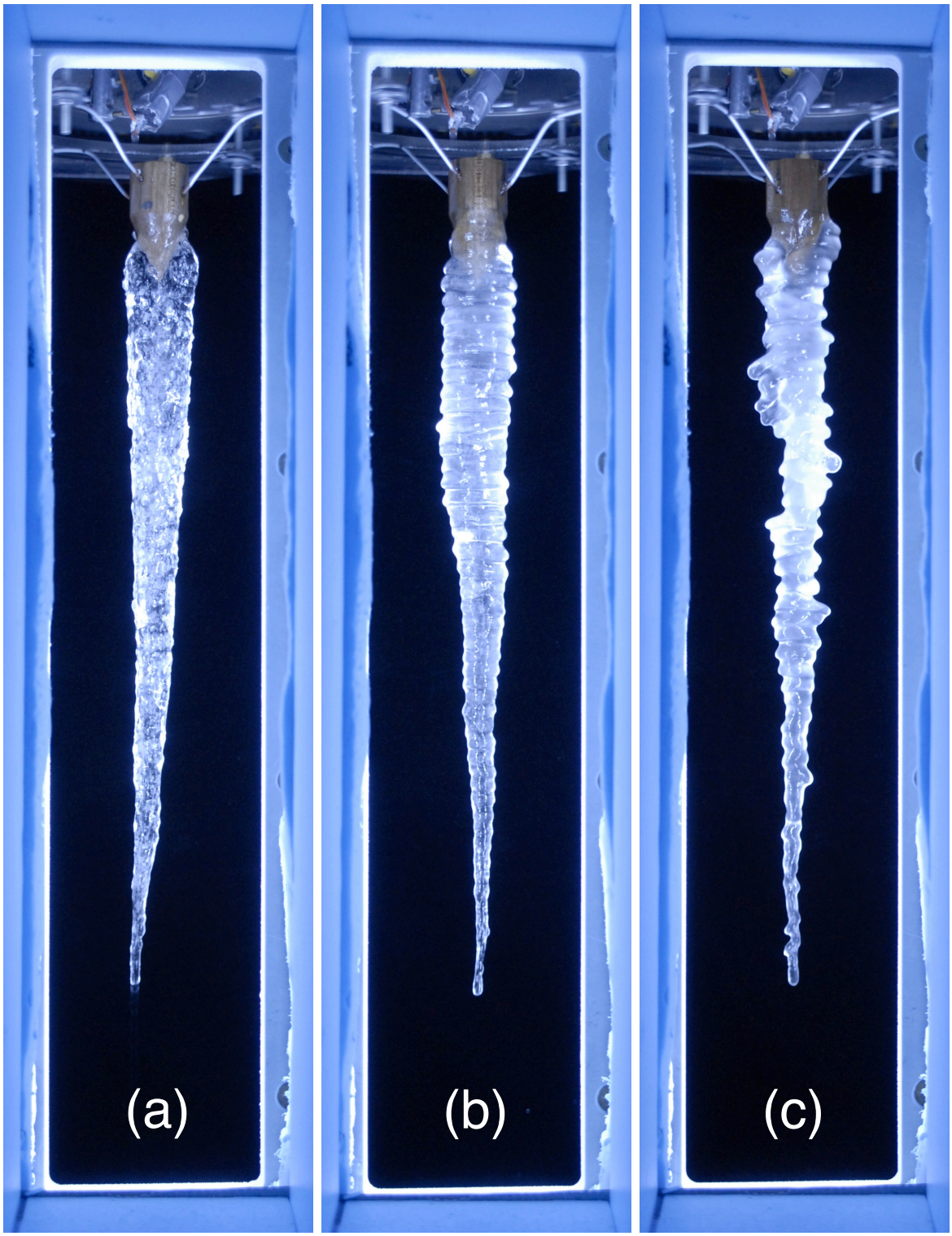

Figure 5.7: Images of three icicles grown under identical conditions: an ambient wall temperature of -12.3 °C, a water supply rate of 2.0 g/min, an input water temperature of 3.0 °C, and a volumetric air flux of 0.95 m^3/min per fan. (a) was made with distilled water; (b) was made with distilled water plus $(8.0 \pm 0.2) \times 10^{-3}$ wt% NaCl; (c) was made with distilled water plus $(1.28 \pm 0.02) \times 10^{-1}$ wt% NaCl.

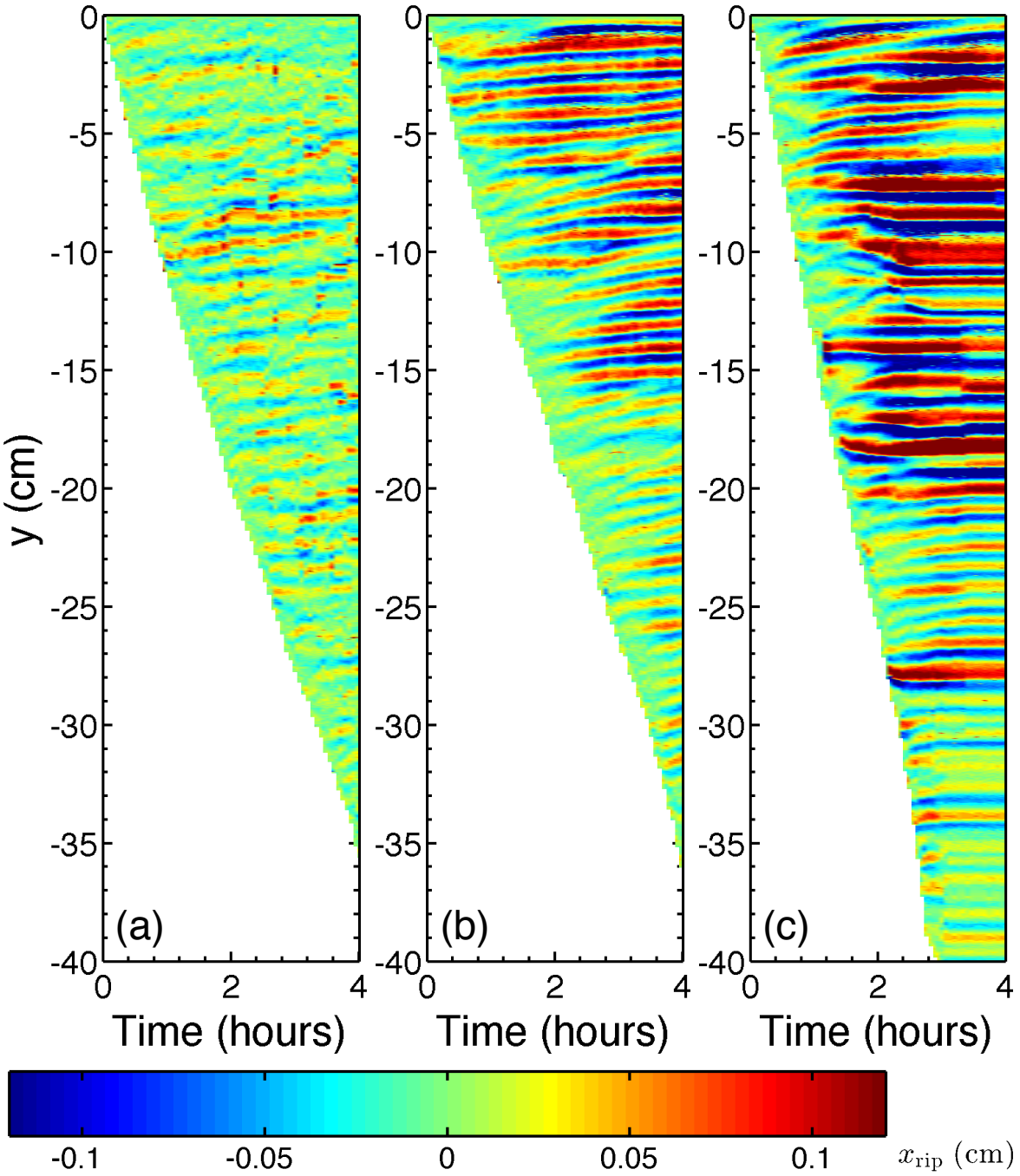

Figure 5.8: Space-time plots showing the evolution of the ripple topography, viewed from one fixed rotational position, for the right edges of the three icicles shown in Fig. 5.7. x_{rip}, indicated by the colour, is plotted as a function of y and time, where y is 0 at the top of the icicle and decreases towards the bottom. The border of the white region follows the downward growth of the icicle tip.

when the icicle reached 10 cm in length, and the data has been averaged over each half-rotation, which consists of 4 unique views; thus, each data point is based on about 4400 edge detection measurements. The amplitudes in Fig. 5.9(a) are smaller than typical amplitudes within the ripple patches in Fig. 5.8, because the Fourier analysis included regions of the icicle with small or no ripples. The error bars, estimated from the standard errors of the averaging sample, are larger for saltier icicles; this reflects the progressive loss of axisymmetry as the feed water salinity was increased.

As seen in Fig. 5.9(a), throughout the growth of the distilled water icicle with no added salt, the amplitude of its residual topographic features that survived the de-trending filter remained below the resolution limit. In contrast, icicles made from sufficiently saline water exhibited clear ripples, whose amplitudes increased to values significantly above the resolution limit before saturating. While measurable ripples were not found on the distilled water icicle, they became apparent at a remarkably low feed water salinity of 2.0×10^{-3} wt%, i.e. only 20 mg of salt per litre of water. The ripples on saltier icicles grew faster to higher amplitudes. Some ripples were observed to decay after their amplitudes had peaked or plateaued; an example of a saline water icicle whose ripples grew then decayed is shown in Fig. 5.10. The error-weighted mean of the ripple wavelengths for the saline water icicles in Fig. 5.9(a) is plotted as a function of time in Fig. 5.9(b); its time average is 0.985 ± 0.004 cm. Even while the ripples were growing, they maintained an approximately constant wavelength; this implies that the ripple wavelength is independent of the ripple amplitude.

To compare the ripples on icicles grown under diverse conditions, we calculated their growth speed dA/dt and time-averaged wavelength $\bar{\lambda}$. To obtain the former, we performed a linear fit within the linear growth regime of a smoothed $A(t)$, defined to be from $t = 0$ to the time at which its slope decreased by more than 50 %; $\bar{\lambda}$ was found for the same regime. The results of modelling the initial rise in $A(t)$ as an exponential growth will be presented in Sec. 5.3. In Fig. 5.11(a), dA/dt is plotted as a function of the feed water salinity for several sets of conditions. As the salinity was increased from zero, ripples grew more rapidly; the increase in dA/dt was approximately logarithmic, which was extremely weak. Like the tip and radial growth speeds (Fig. 3.13), the growth speed of the ripples

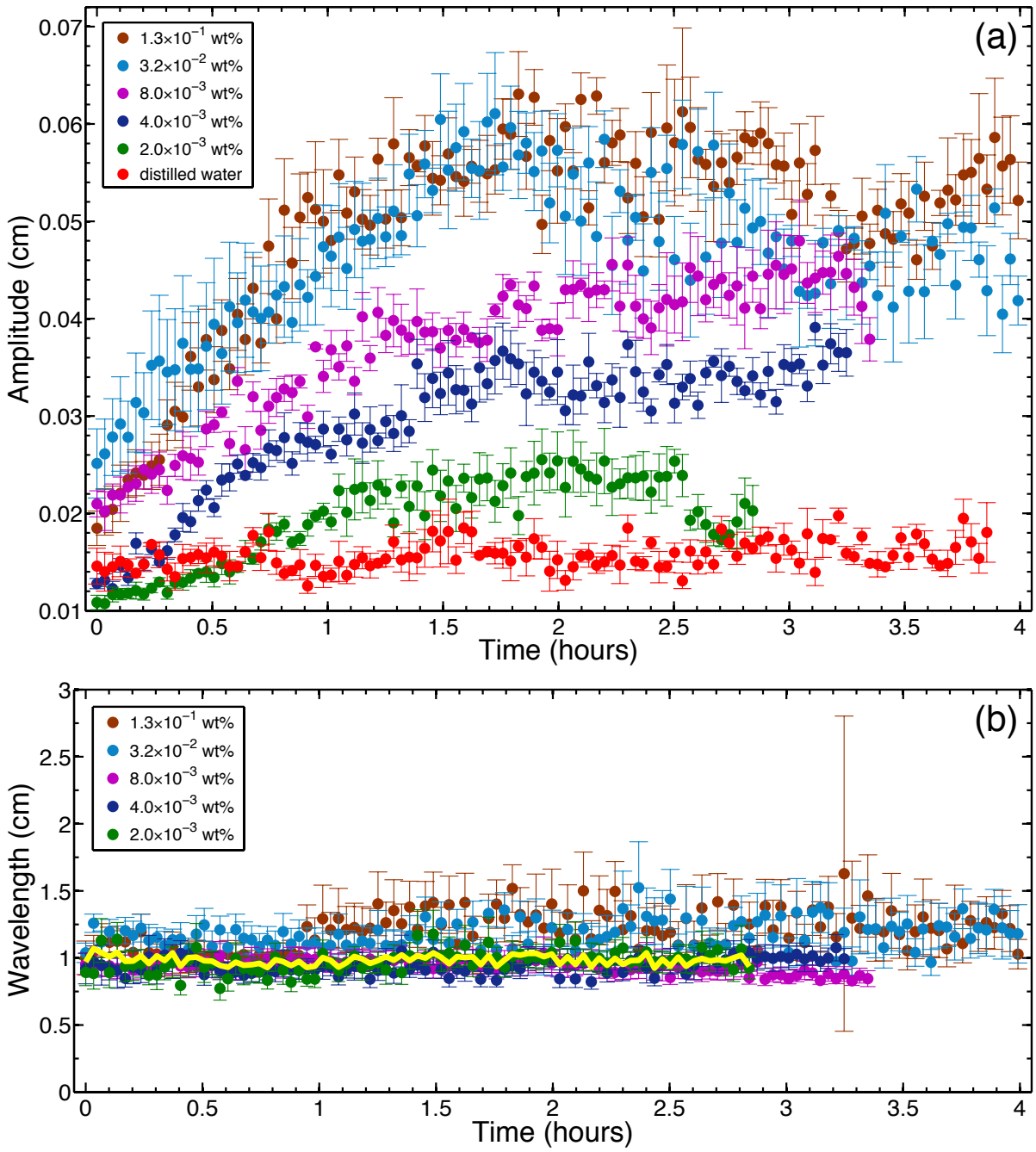

Figure 5.9: Time-series of the (a) amplitude and (b) wavelength of the ripples on icicles made from feed water of various salinities. The colour-coded circles in the two panels correspond to the same set of experiments. The legends show the feed water salinity for each run. In all experiments, the ambient wall temperature was −12.3 °C, the water supply rate was 2.0 g/min, the input water temperature was 3.0 °C, and the surrounding air flux due to each fan was 0.95 m^3/min. Time zero corresponds to the time when the icicle reached 10 cm in length. The error bars in (a) indicate the standard errors from averaging over each half-rotation. The errors in (b) were estimated using the half widths at half-maximum of the best Lorentzian fits to the Fourier spectra of the ripple coordinates (Fig. 5.3). The yellow line in (b) shows the error-weighted mean of the wavelength data as a function of time.

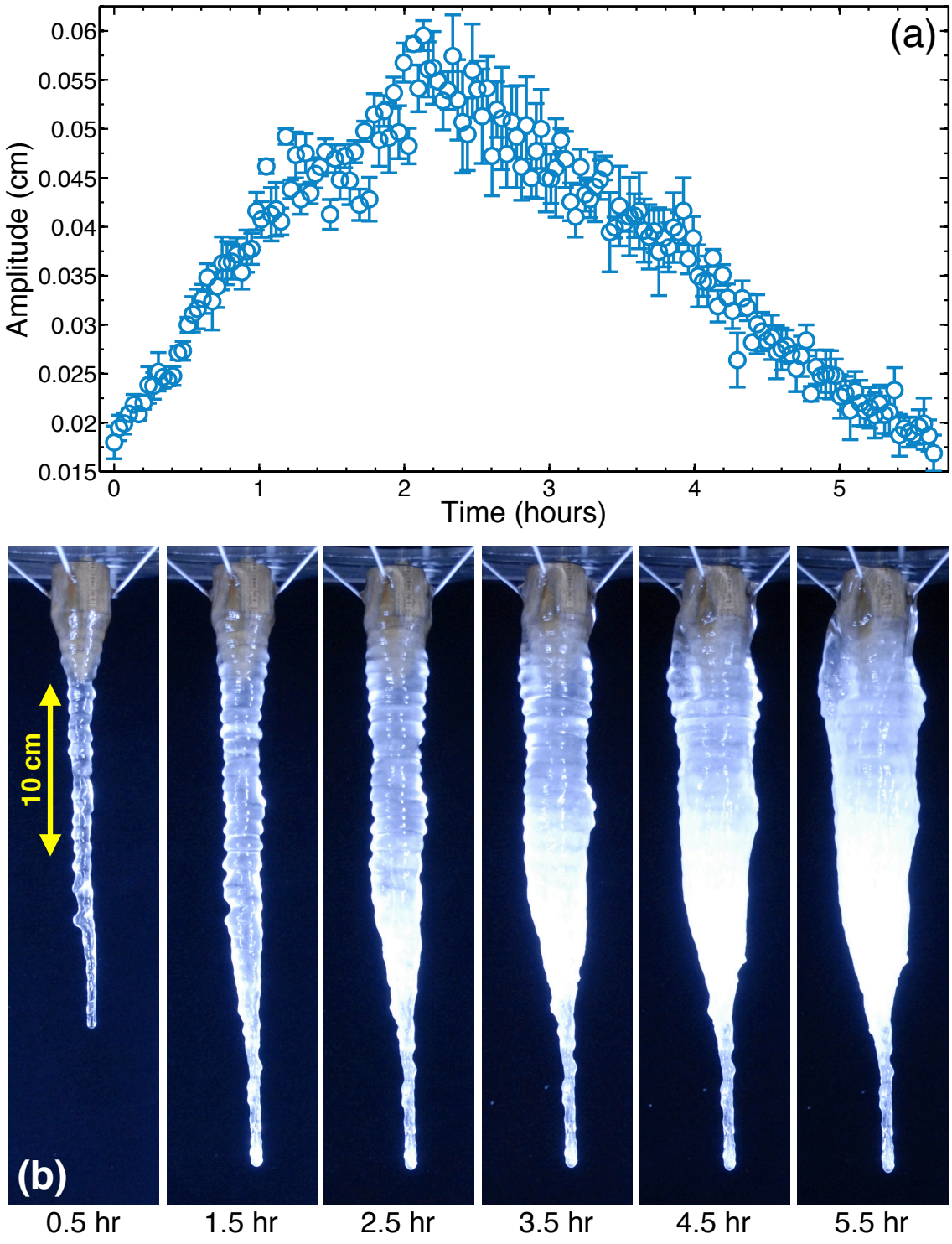

Figure 5.10: Ripple growth and decay on a saline water icicle: (a) amplitude time-series, (b) photographic time-series. The ambient wall temperature was -13.6 °C, the water supply rate was 1.0 g/min, the input water temperature was 3.0 °C, the surrounding air flux due to each fan was 0.82 m^3/min, and the feed water salinity was 3.2×10^{-2} wt%. Time zero corresponds to the time when the icicle reached 10 cm in length. The error bars in (a) show the standard errors from averaging over each half-rotation. The tip growth of this icicle ceased at $t = 1.1$ hr, well before its ripples began to decay.

decreased and became more scattered above 1 wt%. On the other hand, $\bar{\lambda}$ remained robustly independent of the feed water salinity, as shown in Fig. 5.11(b), though the most prominent features in the filtered topography of the saltiest icicles all had wavelengths that exceeded 1 cm. The global mean of $\bar{\lambda}$ in Fig. 5.11(b) is 1.04 ± 0.01 cm.

To quantitatively characterize the ripple motion on an icicle for a fixed rotational position, we followed the peaks of three randomly selected ripples in time, starting when the icicle reached 10 cm in length, and calculated a velocity v_{rip} by averaging the slopes of the best-fit lines through the peak position time-series. The magnitude of v_{rip} gives a characteristic ripple traveling speed, and its sign indicates the dominant direction of motion. Two applications of this procedure are illustrated in Fig. 5.12.

In Fig. 5.13, v_{rip} is plotted as a function of the feed water salinity for several sets of conditions. Here, the data has been averaged over each rotation, which consists of 8 unique views, so each point is based on 24 velocity measurements; the error bars show the standard errors of the mean. Below about 0.05 wt%, ripples climbed the icicle consistently at speeds of millimetres per hour (e.g. Figs. 5.8(b) and 5.12(a)), like the ripples on the tap water ice finger shown in Fig. 5.2. Above 0.05 wt%, uniform upward ripple motion was less frequently observed, as the ripple dynamics became more complex (e.g. Figs. 5.8(c) and 5.12(b)). Some ripples moved nonlinearly, and different ripples on the same icicle may travel in opposite directions, as in Fig. 5.12(b); this could result in a negative v_{rip} with a large uncertainty.

Given the sensitive dependence of the ripple dynamics on dissolved impurities, it is natural to examine the effect of dissolved gases. All of the water used in our experiments had been exposed to air and presumably contained some concentration of dissolved oxygen and other gases. Thus, we grew icicles from distilled water that had air bubbled through it for 12 hours, which may therefore be assumed to be saturated, or possibly supersaturated, with dissolved gases. Fig. 5.14(a) shows a typical time-series of their ripple amplitude. Icicles made from deliberately aerated distilled water were indistinguishable from those made using our standard distilled water; in particular, no measurable ripples were found in either case. We conclude from this that dissolved gases alone are insufficient to trigger the rippling instability.

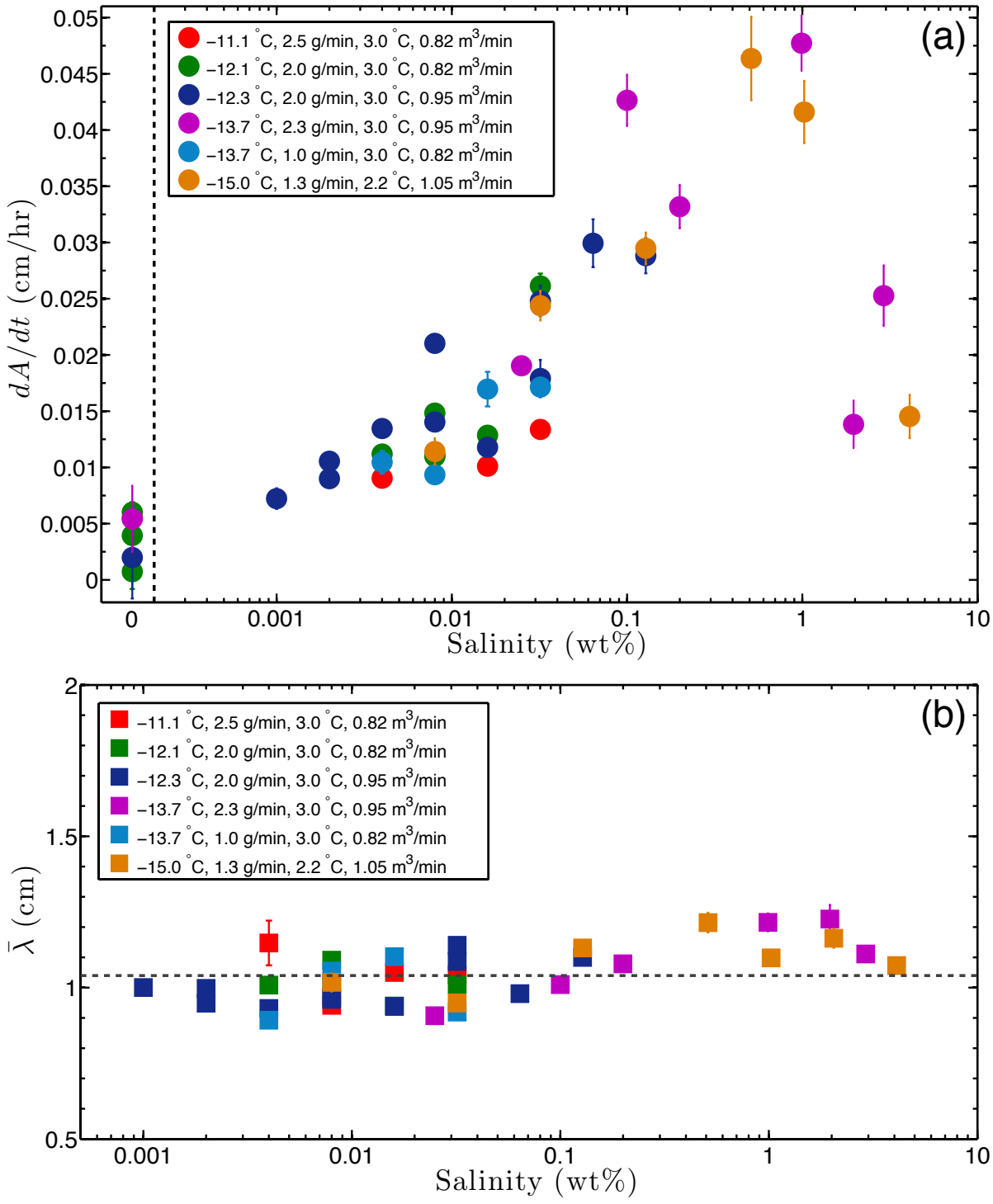

Figure 5.11: (a) Growth speeds and (b) time-averaged wavelengths of icicle ripples *vs.* feed water salinity. The fixed variables are: ambient wall temperature, water supply rate, input water temperature, and surrounding air flux due to each fan. Each colour corresponds to one set of experiments with the same values of the fixed variables. The legends show the values of the fixed variables for each set of experiments. The vertical dashed line in (a) is a scale break, to the right of which salinity is plotted on a log scale. The horizontal dashed line in (b) indicates the global mean of $\bar{\lambda}$.

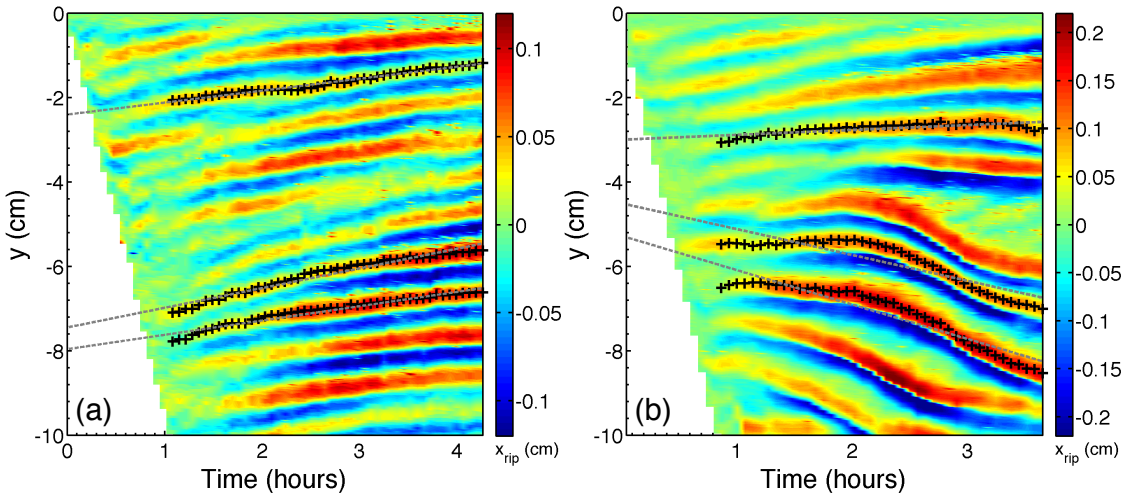

Figure 5.12: Each space-time plot shows the evolution of the ripple topography, viewed from one fixed rotational position, for the top 10 cm of the right edge of a saline water icicle. The feed water salinity was 4.0×10^{-3} wt% for (a) and 6.4×10^{-2} wt% for (b). The crosses follow the peaks of 3 randomly selected ripples in time, starting when the icicle reached 10 cm in length. The dashed lines are best linear fits through the crosses; the mean of their slopes gives a characteristic ripple traveling velocity v_{rip}. The magnitude of v_{rip} is the characteristic ripple traveling speed; the sign of v_{rip} indicates the dominant direction of motion: positive means upward, and negative means downward.

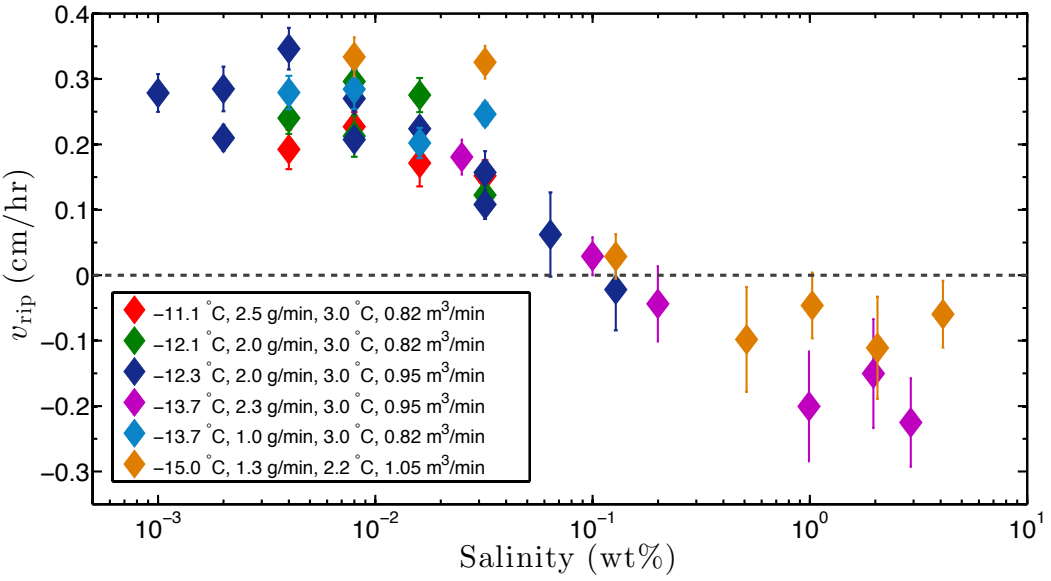

Figure 5.13: Ripple traveling velocities *vs.* feed water salinity. The fixed variables are: ambient wall temperature, water supply rate, input water temperature, and surrounding air flux due to each fan. Each colour corresponds to one set of experiments with the same values of the fixed variables. The legend shows the values of the fixed variables for each set of experiments. The dashed line marks $v_{\text{rip}} = 0$.

As mentioned earlier, some existing theories on icicle ripples [34–39] predict that the water-air surface tension is an important parameter for the instability. To test this, we used the non-ionic surfactant Triton X-100 to vary the surface tension of the feed water. As shown in Table 2.1, Triton X-100 has a negligible effect on the conductivity of the solution. Icicles were grown from distilled water mixed with sufficient Triton X-100 to reduce its surface tension by more than 45 % (Fig. 2.5(a)). Fig. 5.14(a) shows a typical time-series of their ripple amplitude. Again, these icicles exhibited no measurable ripples, like the icicles made from distilled water with no added surfactant. Thus, reduced surface tension alone does not cause ripples to grow. When Triton X-100 was added to a saline water source that produced ripply icicles, the ripples on the resultant icicles decayed at an earlier time (Fig. 5.14(b)).

Next, we compare the ripples on salty icicles made from water of the same salinity but under different conditions. As shown in Figs. 5.15 and 5.16, neither their growth speed nor their traveling velocity is obviously dependent on the ambient temperature, water supply rate, input water temperature, or surrounding air flux. Therefore, we assert that the feed water salinity is the most significant control parameter in the growth and motion of icicle ripples. The ripple wavelength, which was previously found to be independent of the feed water salinity (Fig. 5.11(b)), is not systematically correlated with extrinsic growth conditions either (Fig. 5.17). The global means of the data in Figs. 5.15, 5.16, and 5.17 are $dA/dt = 0.018 \pm 0.001$ cm/hr, $v_{\rm rip} = 0.23 \pm 0.03$ cm/hr, and $\bar{\lambda} = 1.01 \pm 0.01$ cm.

Finally, in Fig. 5.18, we plot the ripple growth speeds of 102 salty icicles, made from water of various salinities and under different conditions, against their radial growth speeds, which were calculated using the methods described in Sec. 3.3. A positive correlation is found, i.e. the ripples on faster-growing icicles tend to grow faster too. A linear fit through the data gives $dA/dt = m \times (dR_0/dt) + b$, where $m = (7.8 \pm 0.5) \times 10^{-2}$ and $b = (-2.3 \pm 0.3) \times 10^{-2}$ cm/hr. This line does not pass through the origin, which suggests that there may be a threshold for the radial growth speed below which ripples do not grow; this threshold would be $dR_0/dt = 0.30 \pm 0.04$ cm/hr.

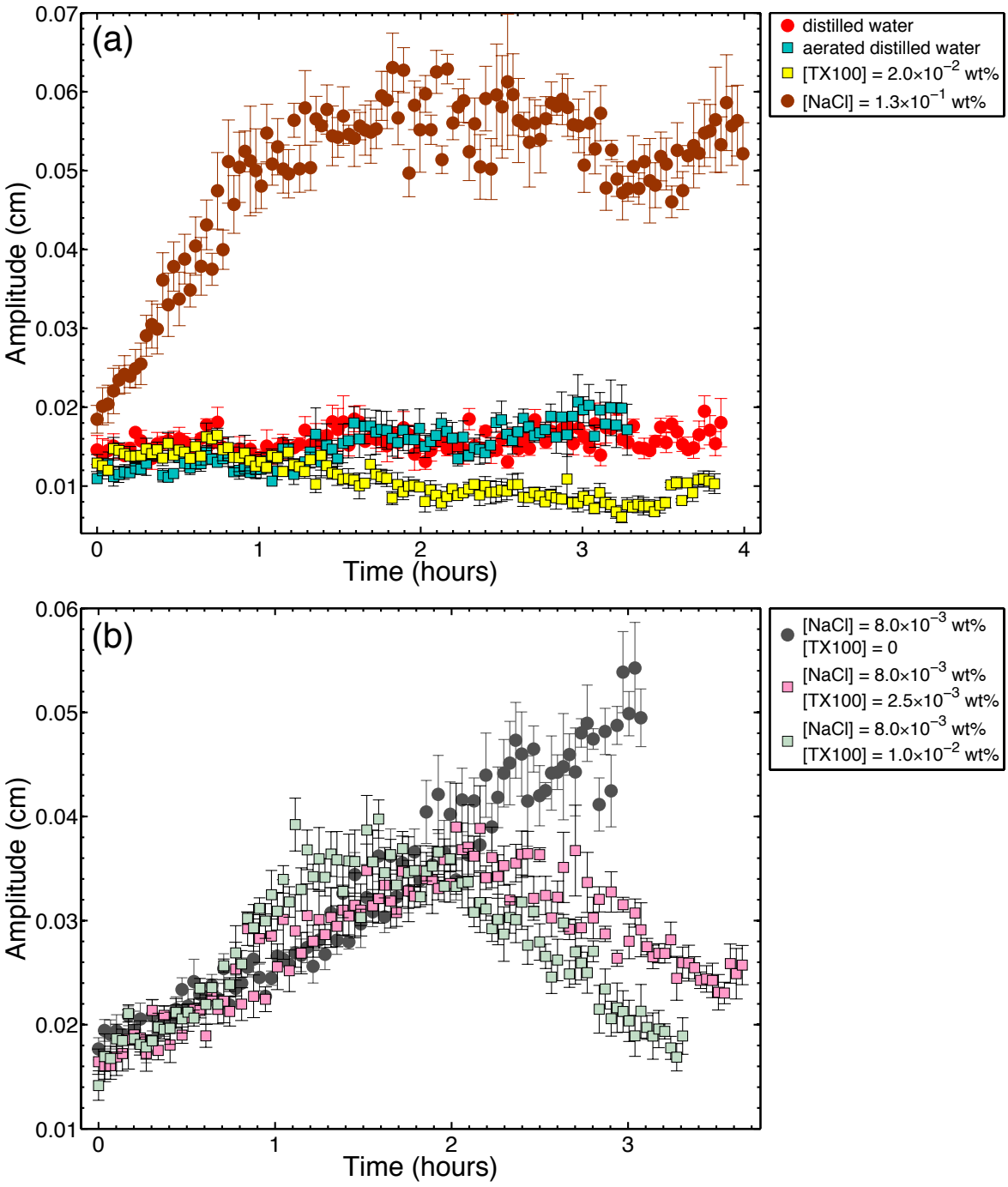

Figure 5.14: Time-series of the amplitude of the ripples on icicles made from various solutions. The legends indicate the water source of each icicle; the NaCl and Triton X-100 were dissolved in distilled water. For all experiments in (a), the ambient wall temperature was −12.3 °C, the water supply rate was 2.0 g/min, the input water temperature was 3.0 °C, and the surrounding air flux due to each fan was 0.95 m^3/min. For all experiments in (b), the ambient wall temperature was −12.1 °C, the water supply rate was 2.0 g/min, the input water temperature was 3.0 °C, and the surrounding air flux due to each fan was 0.82 m^3/min. Time zero corresponds to the time when the icicle reached 10 cm in length. The error bars indicate the standard errors from averaging over each half-rotation.

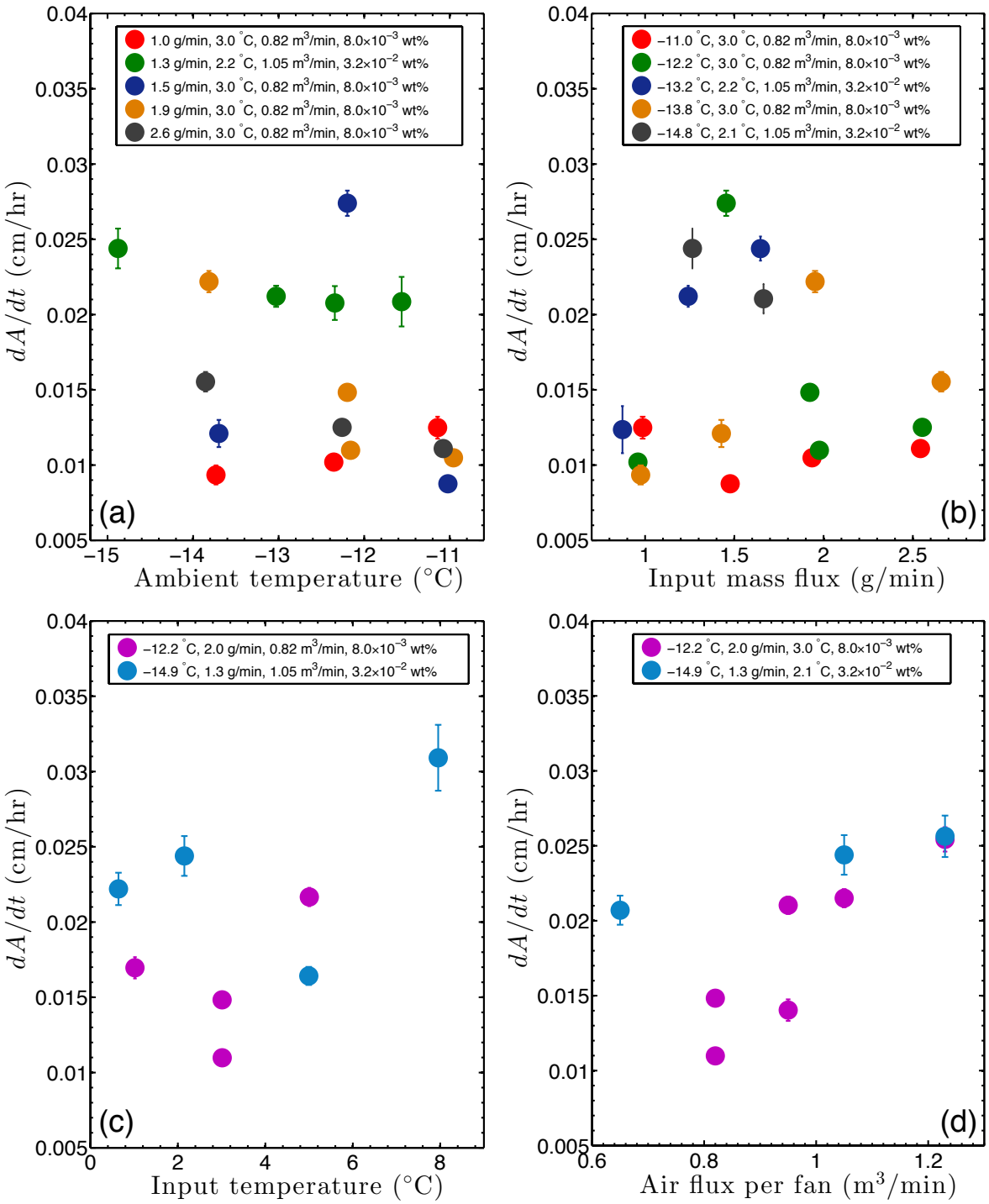

Figure 5.15: Ripple growth speeds of saline water icicles *vs.* extrinsic conditions. The fixed variables in each panel are: (a) water supply rate, input water temperature, air flux per fan, and feed water salinity; (b) ambient wall temperature, input water temperature, air flux per fan, and feed water salinity; (c) ambient wall temperature, water supply rate, air flux per fan, and feed water salinity; (d) ambient wall temperature, water supply rate, input water temperature, and feed water salinity. Each colour corresponds to one set of experiments with the same values of the fixed variables. The legends show the values of the fixed variables for each set of experiments.

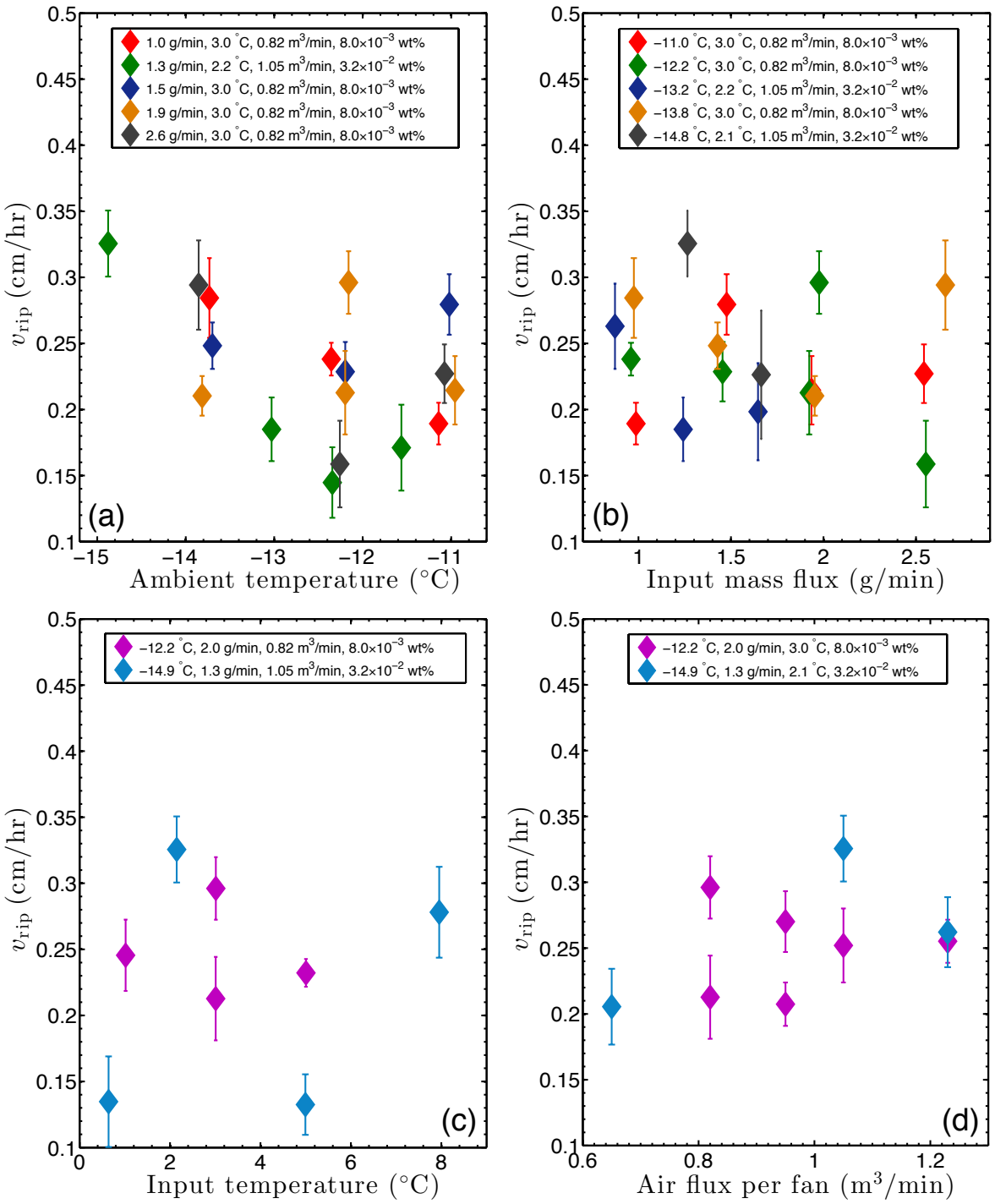

Figure 5.16: Ripple traveling velocities of saline water icicles *vs.* extrinsic conditions. The fixed variables in each panel are: (a) water supply rate, input water temperature, air flux per fan, and feed water salinity; (b) ambient wall temperature, input water temperature, air flux per fan, and feed water salinity; (c) ambient wall temperature, water supply rate, air flux per fan, and feed water salinity; (d) ambient wall temperature, water supply rate, input water temperature, and feed water salinity. Each colour corresponds to one set of experiments with the same values of the fixed variables. The legends show the values of the fixed variables for each set of experiments.

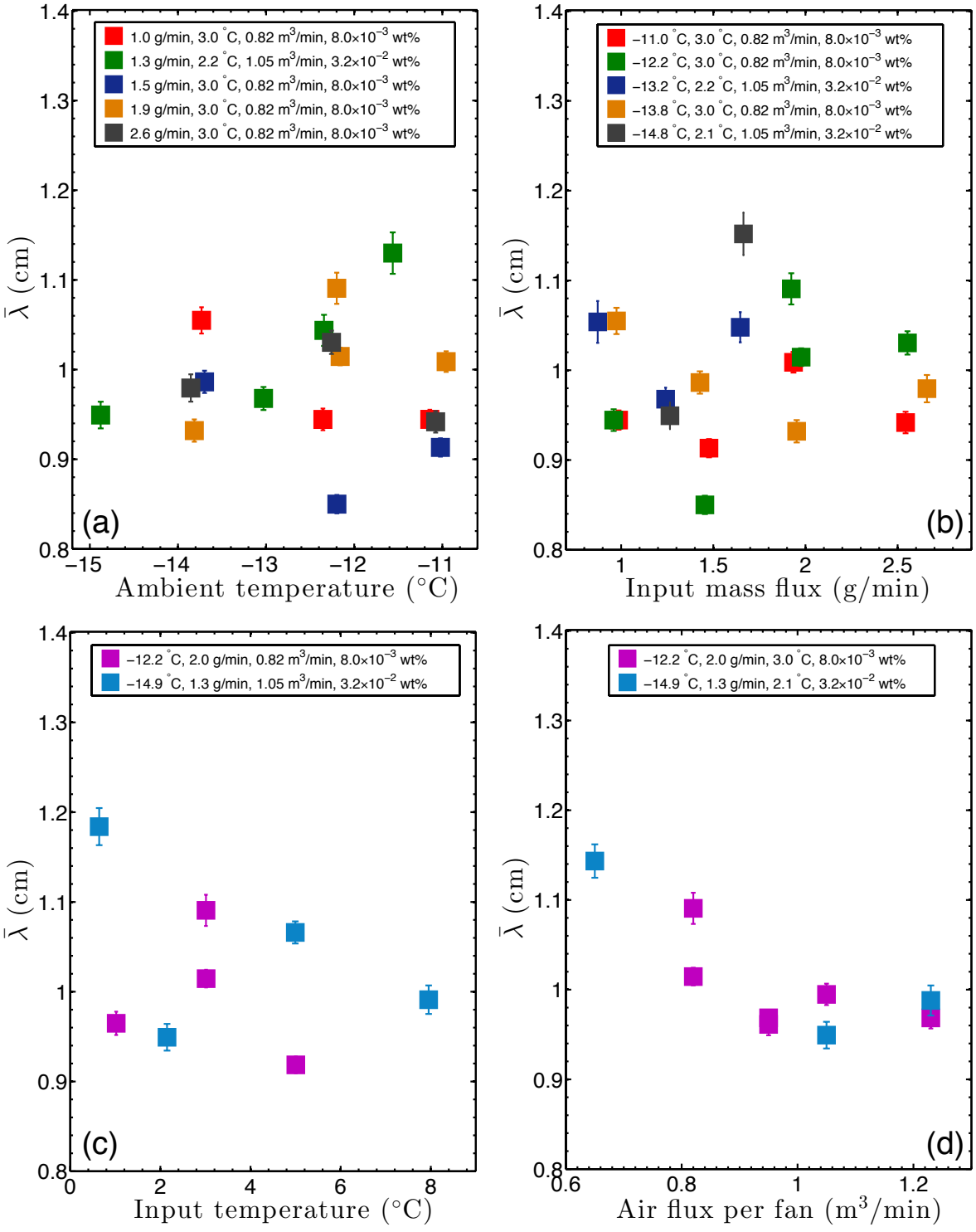

Figure 5.17: Ripple wavelengths of saline water icicles *vs.* extrinsic conditions. The fixed variables in each panel are: (a) water supply rate, input water temperature, air flux per fan, and feed water salinity; (b) ambient wall temperature, input water temperature, air flux per fan, and feed water salinity; (c) ambient wall temperature, water supply rate, air flux per fan, and feed water salinity; (d) ambient wall temperature, water supply rate, input water temperature, and feed water salinity. Each colour corresponds to one set of experiments with the same values of the fixed variables. The legends show the values of the fixed variables for each set of experiments.

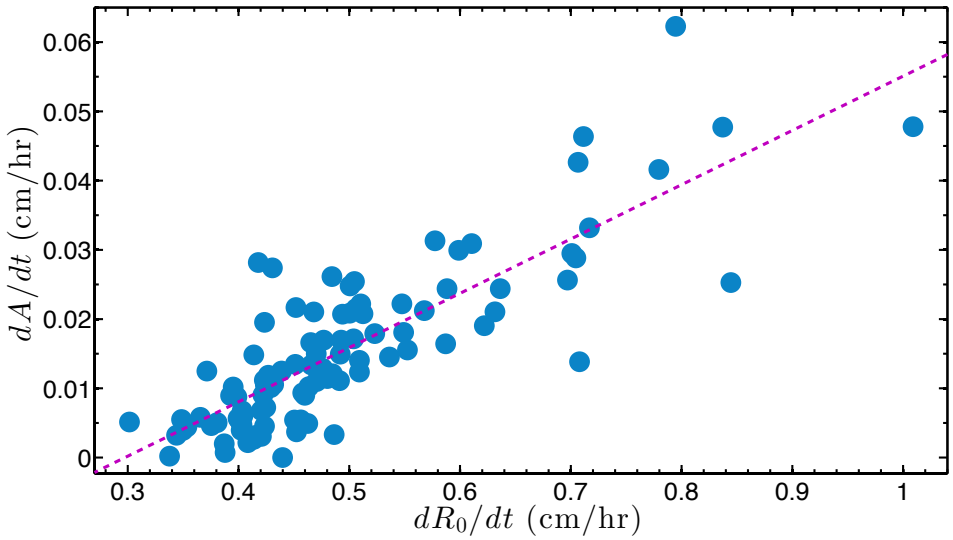

Figure 5.18: Ripple *vs.* radial growth speeds for 102 icicles made from water of various salinities and under different conditions. The magenta line is the best linear fit.

5.3 Theoretical discussion

In this section, we review existing theories on the rippling instability of icicles and discuss how our experimental observations contradict their predictions. Based on the inconsistencies, we identify fundamental problems with the theories and suggest ways in which they may be resolved.

The first attempt to explain the formation of icicle ripples via a quantitative theory is by Ogawa *et al.* [33], who performed a linear stability analysis of ice growth under a water film that is flowing down a semi-infinite inclined ice ramp. The base state for the flow of the water film is the parabolic profile derived in Sec. 3.1, i.e. Eq. 3.6, and its thermal base state is a linear temperature gradient across the film. Ogawa *et al.* calculated the responses of the flow and temperature fields to an infinitesimal, sinusoidal topographic perturbation, with a variable wavenumber k, of the ice-water interface. These responses can in turn react back on the perturbation itself.

Two important approximations were made. The long-wavelength approximation retained up to the first order of the dimensionless wavenumber $\mu = kh$, where h is the thickness of the water film. This is a valid approximation, because for typical values of the ripple wavelength $\lambda = 2\pi/k = 1$ cm and water film thickness $h = 5.6 \times 10^{-5}$ m

(Sec. 4.1), $\mu = 0.035$ which is small. The quasi-static approximation neglected the time dependence of the perturbed flow and temperature fields, and is also justified because their time scales are much shorter than the slowly evolving ice topography.

The Stefan condition, which relates the growth of ice to the heat flux across its surface, was used to determine the amplification rate and traveling velocity of the perturbation, each as a function of k. Ogawa *et al.* [33] find that perturbations with a wide range of wavenumbers have positive amplification rates and hence are linearly unstable. The wavelength of the most unstable mode, i.e. the mode with the highest amplification rate, emerges as a result of two competing effects: heat transport in the air encourages protrusions at the ice-water interface to grow faster, while heat transport in the flowing water film smoothes out temperature gradients at the ice-water interface, thus inhibiting the instability. The motion of all unstable modes, including the most unstable mode, is predicted to be downward.

Ueno *et al.* [34–39] carried out a similar linear stability analysis, but with some differences. One of the boundary conditions for the amplitude of the perturbed stream function, governed by an Orr-Sommerfeld equation, contains a term $(\mu^3 \mathrm{Re}/\mathrm{We})\xi_\mathrm{k}$ [36], where ξ_k is the amplitude of the perturbed water-air interface, and Re and We are the Reynolds and Weber numbers, defined in Table A.2. Since this is a third-order term in μ, Ogawa *et al.* [33] neglected it on the basis of the long-wavelength approximation. However, as pointed out by Ueno *et al.* [34–39], this term is *not* negligible, because the Weber number is very small, which indicates that surface tension effects may be important. Under typical conditions, we find $\mathrm{Re} = 0.27$ and $\mathrm{We} = 5.6 \times 10^{-5}$ for the thin water film, and thus $\mu^3 \mathrm{Re}/\mathrm{We} = 0.21$, which is indeed higher than $\mathrm{O}(\mu)$.

By keeping the term with the Weber number, Ueno *et al.* [34–39], in effect, took into account the role of the surface tension, which acts on the water-air interface as a restoring force and influences its shape, in the instability at the ice-water interface. Conversely, the wavenumber of the disturbed ice-water interface affects the magnitude of the restoring force term and hence the shape of the water-air interface. For instance, if the surface tension effect is sufficiently large, the water-air interface tends to be flat against the disturbed ice-water interface, and this contributes to the stabilization of the ice-water

interface. This is in contrast with the theory of Ogawa *et al.* [33], which erroneously neglected the term involving the surface tension and assumed the two perturbed interfaces always have the same amplitude. Consequently, surface tension appears as a parameter in the predictions of Ueno *et al.* [34–39] for the amplification rate, wavelength, and traveling velocity of the ripples, but not in the predictions of Ogawa *et al.* [33]. Other differences exist between the two theories, such as the choice of thermal boundary conditions, which will be discussed later in this section.

Both of these theories [33–39] predict growing ripples on pure water icicles. More precisely, since these theories are linear, the ripple growth is predicted to be exponential. No ripple growth, exponential or otherwise, is found on pure water icicles in our experiments (Fig. 5.9(a)). No theory has considered the effect of impurities and thus been able to predict the salt concentration dependence of the ripple growth shown in Fig. 5.11(a). Moreover, the theory of Ueno *et al.* [34–39] does not correctly account for the effect of surface tension, with or without added salt or surfactant.

In Ref. [36], Ueno's predicted dispersion relation between the amplification rate σ_r of the perturbation and its wavenumber k is given explicitly:

$$\sigma_r(k) = \bar{v}_g k - \frac{1}{12}\left(\frac{\mathrm{Pe}_h \gamma h}{\rho_L g}\right)\bar{v}_g k^4, \tag{5.1}$$

where $\bar{v}_g$ is the mean growth speed of the icicle surface, Pe_h is the Péclet number for heat transport in the liquid film as defined in Sec. 4.1, γ is the surface tension at the liquid-air interface, h is the liquid film thickness given by Eq. 3.8, ρ_L is is the liquid density, and g is the acceleration due to gravity. From Eq. 5.1, the wavenumber k_c of the most unstable mode and its amplification rate can be derived:

$$k_c = \left(\frac{3\rho_L g}{\mathrm{Pe}_h \gamma h}\right)^{1/3}, \quad \sigma_r(k_c) = \frac{3}{4}\bar{v}_g k_c \sim \gamma^{-1/3}. \tag{5.2}$$

An increase in the surface tension is thus predicted to result in a weak decrease in the ripple amplification rate.

The effect of added salt on the surface tension is much too small and of the wrong

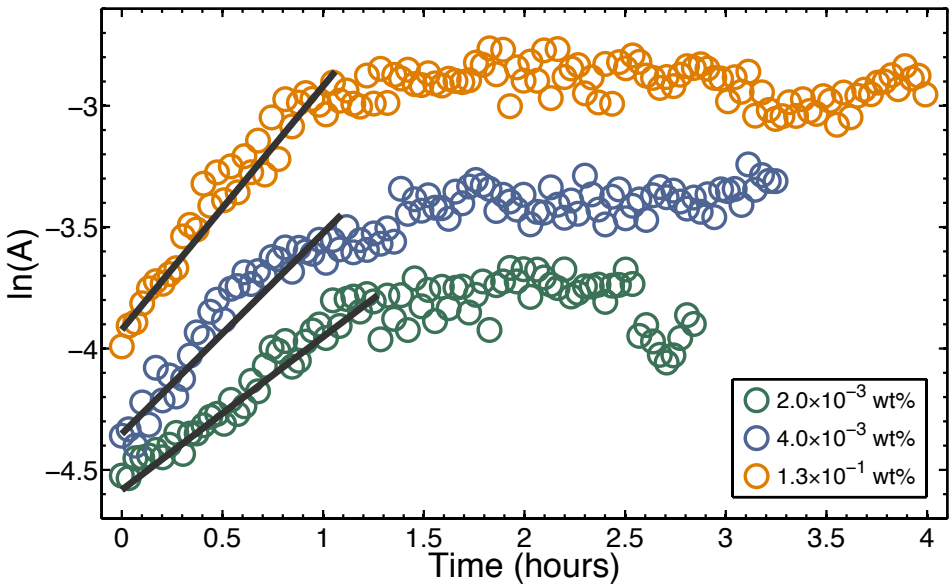

Figure 5.19: The natural log of the ripple amplitude for 3 saline water icicles, grown under identical conditions, is plotted as a function of time. Each grey line is a best-fit line to the part of the amplitude time-series that can be reasonably modelled as an exponential growth. The slope of the best-fit line gives an estimate for the ripple amplification rate.

sign to account for the amplification of the ripples. In Fig. 5.19, the natural log of the ripple amplitude for 3 saline water icicles is plotted as a function of time. In this plot, exponentially growing ripples are characterized by a straight line with a positive slope; this slope gives an estimate for the rate at which the ripples amplify. While the initial evolution of the ripple amplitude in Fig. 5.19 can be reasonably described by an exponential growth, this ceases to be the case after about an hour. The cessation of the exponential amplitude growth is caused by nonlinear effects and thus not predicted or explained by any linear theory.

To measure the amplification rate of the ripples during their exponential growth, we performed a linear fit to the $\ln(A)$ time-series between $t = 0$ and the time at which its slope decreased by more than 50 %. It is important to note that the ripple amplification rate σ_r is a different quantity than the ripple growth speed dA/dt defined in Sec. 5.2. The former is found from an exponential fit to $A(t)$ and has a unit of [1/time]; the latter is obtained from a linear fit to $A(t)$ and has a unit of [length/time]. Nevertheless, they are obviously related and are, in fact, positively correlated, as shown in Fig. 5.20(a).

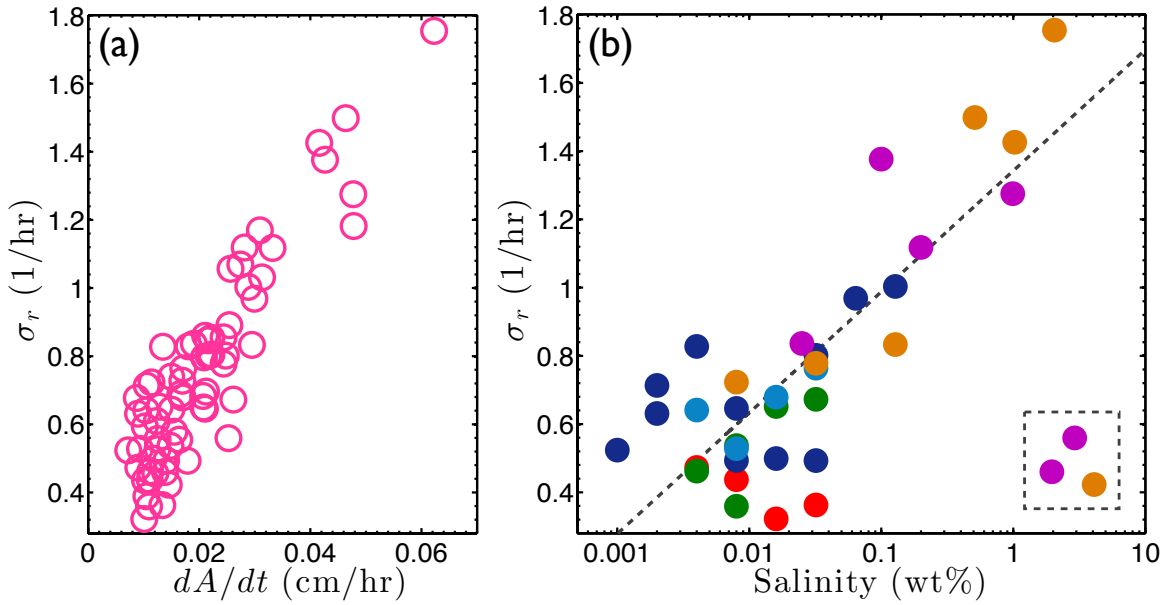

Figure 5.20: (a) Ripple amplification rate *vs.* ripple growth speed for 69 icicles made from saline water of various concentrations under different conditions. (b) Ripple amplification rate *vs.* feed water salinity: each colour corresponds to one set of experiments with the same values of the fixed variables, which are as shown in the legend of Fig. 5.11(a); the dashed line is the best linear fit to the data points, barring those in the dashed box.

Over the range of salt concentrations in Fig. 5.20(b), the surface tension increases by 0.4 % [46], while the measured amplification rate increases by a factor of 5. The addition of surfactant, which greatly lowers the water-air surface tension, produces no measurable ripples (Fig. 5.14(a)) and hence no increase in their amplification rate. These observations contradict the $\gamma^{-1/3}$ dependence of Eq. 5.2.

Next, we compare the ripple amplification rates, wavelengths, and traveling velocities predicted by Ogawa *et al.* [33] and Ueno [36] directly against the measured values from our saline icicle experiments. The results are shown in Figs. 5.21, 5.22(a), and 5.22(b) respectively. The predictions of both Ogawa *et al.* and Ueno depend on the following parameters: the water supply rate W_0, the radial growth speed dR/dt of the icicle, the acceleration due to gravity g, and the density ρ_L, thermal diffusivity κ_L, and kinematic viscosity ν_L of the feed water. Ueno's predictions additionally depend on the surface tension γ, as well as the thermal conductivities of ice Λ_I and water Λ_L. To calculate the predictions, which are made for pure water icicles, we use the values of W_0 and dR_0/dt

	Value		**Value**
W_0	2.0 g/min	ρ_L	1.00×10^3 kg/m^3
dR_0/dt	0.51 cm/hr	κ_L	1.36×10^{-7} m^2/s
S	8.0×10^{-3} wt%	ν_L	1.79×10^{-6} m^2/s
g	9.8 m/s^2	γ	7.56×10^{-2} N/m
Λ_I	2.22 W/(m·K)	Λ_L	0.57 W/(m·K)

Table 5.1: Typical parameter values in the calculation of the theoretical predictions by Ogawa *et al.* [33] and Ueno [36]. The values of ρ_L, κ_L, ν_L, γ, and Λ_L, which vary with the salinity S of the water, are estimated at 0 °C using Ref. [46].

from our experiments, and the salinity-dependent values of ρ_L, κ_L, ν_L, γ, and Λ_L from Ref. [46]. The values of these parameters under typical experimental conditions are given in Table 5.1.

The predicted values of the ripple wavelength λ (Fig. 5.22(a)) are smaller than our measurements in nearly all cases. Nevertheless, both theories predict λ better than a naive, direct application of the Mullins-Sekerka theory [61, 62], which is commonly used to explain morphological instabilities that arise at solidification fronts. In the Mullins-Sekerka theory for a pure substance such as water, the wavelength of the most unstable mode emerges from a competition between the Laplace instability and the Gibbs-Thomson effect. The Laplace instability is a destabilization mechanism that enhances thermal diffusion at the parts of the solid-liquid interface that protrude into the liquid, which is supercooled, and the Gibbs-Thomson effect is a depression of the melting temperature that varies with the curvature of the interface. The curvature of the ripples on icicles are too small for the Gibbs-Thomson effect to be significant [26, 33, 36]. Moreover, the Mullins-Sekerka theory assumes the liquid is semi-infinite, whereas the water layer on the icicle is *thin*, much more so than its typical radius. Under typical experimental conditions, the Mullins-Sekerka theory predicts a wavelength of $\lambda_{\mathrm{MS}} = 0.006$ cm, which is substantially smaller than the typical ripple wavelength observed on laboratory icicles.

The predictions of Ogawa *et al.* [33] and Ueno [36] for the ripple amplification rate σ_r (Fig. 5.21) are higher than and not of the same order of magnitude as the values estimated from our data. While the theories do capture the observed positive correlation

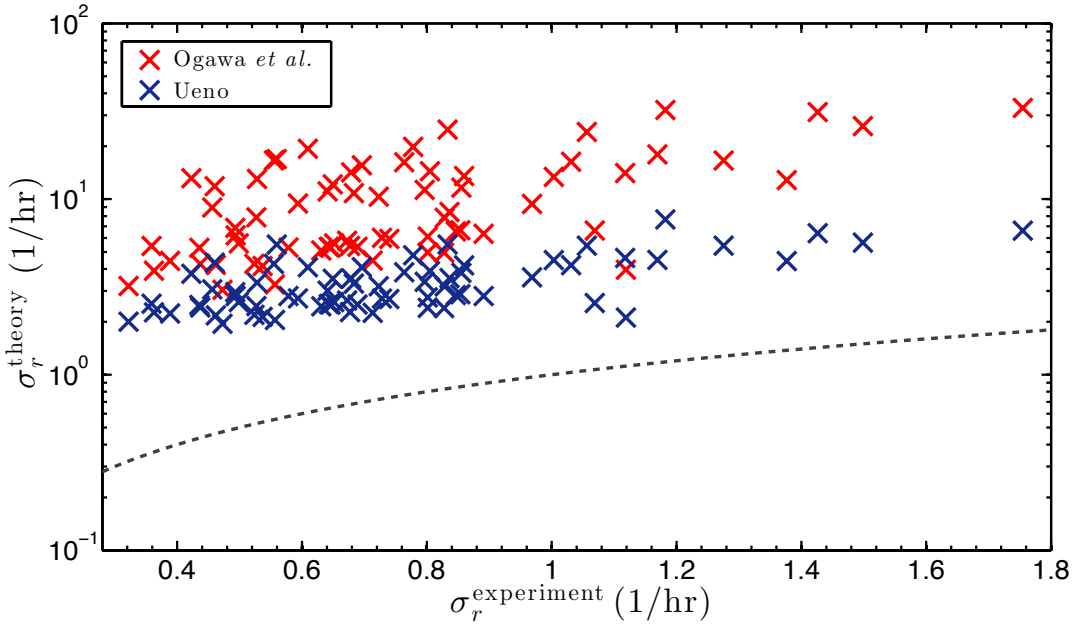

Figure 5.21: Theoretical predictions by Ogawa *et al.* [33] and Ueno [36] *vs.* experimental data for the ripple amplification rate of 69 icicles made from saline water of various concentrations under different conditions. The dashed curve represents perfect agreement between theory and experiment.

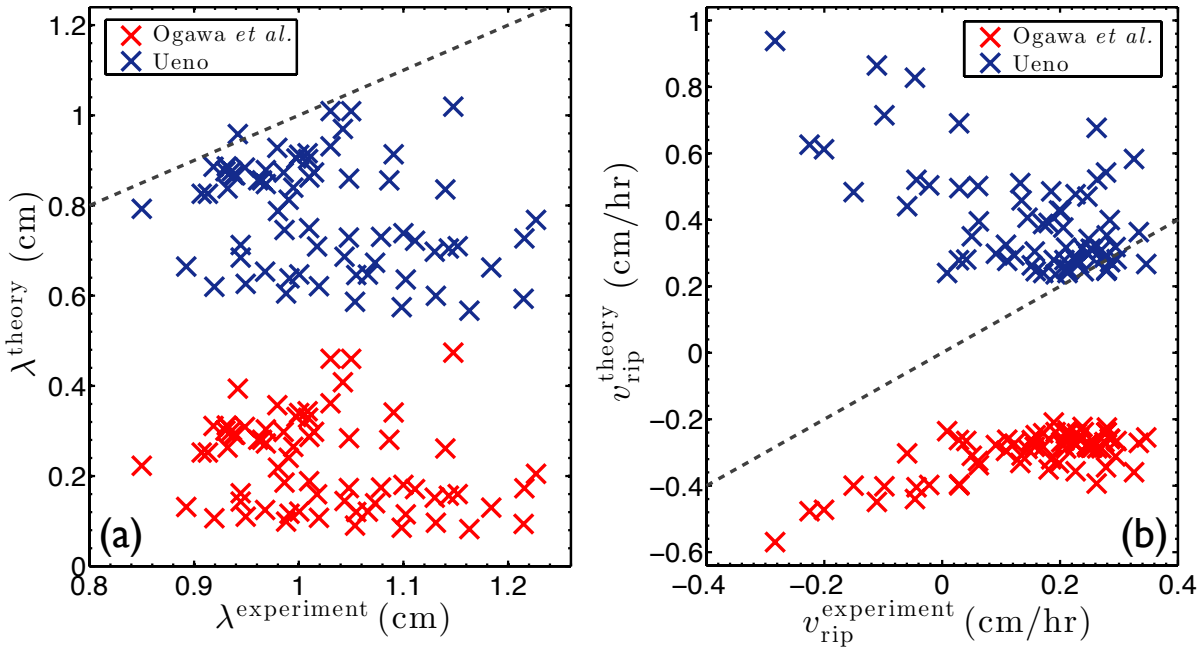

Figure 5.22: Theoretical predictions by Ogawa *et al.* [33] and Ueno [36] *vs.* experimental data for the ripple (a) wavelength and (b) traveling velocity of the same 69 icicles as in Fig. 5.21. The dashed lines represent perfect agreement between theory and experiment.

between the growth of icicles and their ripples, they do not predict our experimentally determined, or any, dependence of σ_r on the feed water salinity. Deviation between theory and experiment is again found, in most cases, for the ripple traveling velocity v_{rip} (Fig. 5.22(b)). Ueno [36] predicts that icicle ripples always climb upward, while Ogawa *et al.* [33] predict the opposite direction of motion. In reality, as seen in Fig. 5.13, icicle ripples can travel both up or down, depending on the feed water salinity, which is not accounted for in either theory.

A theory of the rippling instability that is consistent with all the experimental facts must, at the very least, include the advection and diffusion of both heat and salt in the water film. This would introduce a second Péclet number Pe_s for salt, in addition to the previously defined Pe_h for heat. These dimensionless numbers indicate the relative importance of the diffusion and advection of heat and salt in the water film. Pe_s is given by hu_s/D, where $D = 1.6 \times 10^{-9}$ m^2/s is the diffusion coefficient of NaCl in water [63], and is about 300 for typical values of the water film thickness h and surface speed u_s, which were calculated in Sec. 4.1. Thus, the salt transport in the water film is dominated by advection, with the salt behaving almost as a non-diffusing passive tracer. In Sec. 4.1, we found $\text{Pe}_h = hu_s/\kappa_L = 3.4$ under typical conditions; $\text{Pe}_s \gg \text{Pe}_h$ reflects the fact that salt diffuses much more slowly than heat.

While some physical insight can be obtained from such dimensional arguments, it is not straightforward to generalize the existing ripple theories to include the effect of salt. The main difficulty lies in the boundary conditions. The boundaries of the water film are its two surfaces — one is contact with ice, and the other with air. The salt is excluded as the ice grows, and its concentration field is advected and diffused by the flowing water film. Unlike heat, salt cannot escape into the surrounding air. Salt also has no direct effect on the temperature in the interior of the water film, or at the water-air interface. The only place it can have a direct physical effect is at the ice-water interface, where the presence of salt reduces the freezing temperature via equilibrium freezing point depression and possibly kinetic effects.

The theory of Ueno *et al.* [34–39] does not impose a boundary condition on the temperature at the ice-water interface. Instead, two thermal boundary conditions are

imposed at the water-air interface. The first is the continuity of heat flux, i.e. the derivative of the temperature field; this is required by the conservation of energy. The second, which sets the temperature of the water-air interface at a fixed value, amounts to an ad hoc 'closure' assumption. With these two conditions prescribed at the water-air interface, no further boundary condition is needed for the temperature at the ice-water interface. As a result, there is no boundary condition available that can be linked to the salt concentration.

Ueno *et al.* [38] have shown that if, within their theoretical framework, the second thermal boundary condition is moved to the ice-water interface, where it would seem natural to set the temperature equal to the freezing point, the resulting amplification rate $\sigma_r(k)$ diverges as $k \to \infty$. This divergence is caused by the lack of a physical mechanism at the ice-water interface to provide a cut-off for small-wavelength disturbances. The 'closure' assumption by Ueno *et al.* [34–39], in effect, evades this by employing the surface tension at the opposite, water-air interface to cut off small-wavelength disturbances and prevent the divergence of $\sigma_r(k)$. However, under this assumption, there is no simple way to include a coupling of the salt concentration and temperature at the ice-water interface to account for the effect of salt. Imposing physically realistic boundary conditions will be essential to the formulation of a successful ripple theory.

Furthermore, in the theory of Ueno *et al.* [34–39], the ice is simply treated as a solid with a nonzero thermal diffusivity. However, as alluded to in Sec. 3.2, the ice-water interface is unstable to the formation of dendrites when freezing proceeds into a supercooled water layer. This is, in fact, an example of the aforementioned Mullins-Sekerka instability [61, 62], and the λ_{MS} calculated earlier gives an estimate for the spacing of the dendrites. Ice that grows dendritically at small scales may not merely be a passive solid. A significant fraction of liquid water can be trapped between the advancing dendrites (Fig. 3.14(b)), resulting in ice that is not solid but "spongy" [7, 14, 47, 48]. In the presence of salt, the "spongy ice" becomes an even more complex "mushy layer," in which both heat and salt may be transported by the porous medium-like flow of its liquid phase [7,64–66]. While it is known that very small amounts of impurities can have important effects on freezing at the small scale, such as in premelting phenomena [67,68],

the stability of a mushy layer under a thin, flowing water film has not been well-studied. A deeper understanding of this may explain our observed effect of impurities on the formation of icicle ripples.

Chapter 6

Conclusion

A comprehensive experimental study on the growth and form of icicles has been presented in this thesis. In this chapter, we summarize the work and discuss some future directions.

We designed and constructed a table-top apparatus for growing laboratory icicles with unprecedented control. Icicles were grown below a sharpened wooden support suspended inside an insulated, refrigerated box. The support was slowly rotated to encourage axisymmetry and to allow all sides of the icicle to be imaged. The ambient temperature was controlled by a commercial bath, which circulated antifreeze through the walls of the box. The water supply was delivered by a peristaltic pump to a temperature-controlled nozzle, which was placed slightly off-axis from the rotating support to promote even water distribution. The air could be stirred by fans in the box. Using this apparatus, we grew 250 icicles under a broad range of conditions. A variety of feed water was used, including distilled water, tap water, and solutions with different concentrations of NaCl, an ionic salt, and Triton X-100, a non-ionic surfactant. The growing icicles were imaged by a digital camera, and image analysis was used to probe the icicle morphology. The icicle mass was estimated from the difference between the masses of the input and drip-off water, which were measured by electronic balances.

In Ch. 3, we reported the most extensive study ever conducted on the growth of laboratory icicles. We found that as the icicle length and radius grew under a given set of conditions, the fraction of the feed water that was consumed by the icicle also increased with time, while the amount of unfrozen water that dripped off its tip decreased with time.

The tip and radial growth speeds, as well as the rate at which the feed water consumption increased, were inversely correlated with the ambient temperature. The growth rates of both the icicle length and the water consumption decreased with increasing input mass flux. While the radial growth speed also decreased with increasing input mass flux above 2 g/min, it increased with the input mass flux below this threshold — this observation is not in agreement with past work [13, 14, 17, 25], which found either a much smaller or no correlation between the radial growth speed and the water supply rate.

Using a heat balance model, adapted from Refs. [14, 18, 25], we calculated the heat transfer coefficients for our laboratory icicles. We determined that the dominant heat transfer mechanism controlling their growth was advection-diffusion in the air; the contributions due to evaporation and radiation were also significant but secondary. If the ambient temperature or water supply rate was sufficiently high, icicles could not be formed. If the ambient temperature or water supply rate was sufficiently low, the tip growth of the icicle advanced only for a short period of time before it ceased. Both the time of cessation and the icicle length at that time were inversely correlated with the speed of tip growth prior to cessation. After cessation, all of the incoming water froze onto the sides of the icicle before reaching the tip. The radial growth at a given height could also come to a halt if all of the water was consumed before making its way there; the closer to the tip, the earlier this occurred.

Adding salt to the feed water changed the growth speeds and cessation behaviours of the resultant icicles. For feed water salinities above 1 wt%, the icicle growth speeds decreased with increasing salinity. Below 1 wt%, however, the icicle grew more quickly when more salt was added to the water. The salinity of the drip-off water from a saline icicle increased during its growth. With salt present in the feed water, the tip of the resultant icicle made a more gradual transition from linear growth to cessation, and cessation occurred under conditions of ambient temperature and input mass flux for which distilled water icicles continued to grow. Contrary to the prediction of Chung *et al.* [16], our lab-grown saline icicles ceased to elongate long before their tip temperature reached the ambient temperature. Unlike distilled water icicles, drip-off continued after cessation for icicles made from sufficiently saline water.

A recent theory [26] suggests that icicles converge to a universal, self-similar shape. In Ch. 4, we performed the first direct test of this theory against experiments. While some profiles of lab-grown icicles fit remarkably well to the theoretically predicted shape, many others deviated significantly from it. The degree of deviation was not correlated with temperature. Rather, it was dependent on the input rate and impurity level of the feed water, and the air motion around the icicle. The faster the water was supplied, the further the resultant icicle deviated from self-similarity and axisymmetry. For a sufficiently low water supply rate, the most 'platonic' icicles were grown from distilled water with the air gently stirred; however, after cessation, their shape also deviated from the theory, increasingly so with time. Icicles grown in strong wind conditions were often bent or twisted, while icicles grown in still air often formed multiple tips; the latter observation contradicts the natural convection assumption of the theory [26]. Icicles made from tap and saline water, too, were more likely to grow multiple tips, as well as lateral topographical features such as bulges, wings, and ripples, all of which contributed to deviation from the self-similar shape. We conclude that the self-similarity theory [26] is only partially successful, at best, in predicting the shape of icicles.

Icicle ripples are an example of pattern formation. In Ch. 5, we presented the first experimental study on the relationship between their dynamics and water purity. Existing linear stability analyses [33–39] predict exponentially growing ripples on distilled water icicles; these were not observed. Instead, when small amounts of salt were added to the feed water, the resultant icicles exhibited clear, sinusoidal-like ripples. Using Fourier methods to extract and analyze the ripples, we found measurable ripple growth at a remarkably low salinity of 0.002 wt%. The ripples on saltier icicles grew faster to higher amplitudes. The ripple growth speed increased very weakly with the feed water salinity; this dependence is not predicted by existing theories [33–39]. While the initial evolution of the ripples could be reasonably described by an exponential growth, this ceased to be the case once their amplitude had saturated. The ripples may decay after their amplitude had peaked or plateaued. The amplitude saturation and decay are nonlinear phenomena and thus not predicted by any linear theory [33–39].

Dissolved gases alone did not cause ripples to form without salt also being present.

Dissolving surfactant in distilled water to greatly reduce its surface tension did not produce ripples. On the other hand, adding a pinch of salt, which increased the surface tension slightly, led to faster ripple growth. These observations contradict the theory of Ueno *et al.* [34–39], which predicts that an increase in the surface tension results in a weak decrease in the ripple amplification rate. While the ripples on faster-growing saline icicles generally grew faster, we found no obvious correlation between the ripple dynamics and extrinsic growth conditions. The ripples always maintained an approximately constant wavelength of 1 cm, even when they were growing. The wavelength was also robustly independent of the feed water salinity. Below a salinity of 0.05 wt%, the ripples climbed up the icicle consistently at speeds of millimetres per hour. Above 0.05 wt%, ripples on the same icicle often travelled in opposite directions, and the motion was often nonlinear. Collectively, these experimental results point to the crucial importance of ionic impurities in the rippling instability of icicles.

No existing theory of the rippling instability [33–39] accounts for the effect of ionic impurities. A theory that is consistent with all the experimental facts must include the advection and diffusion of both heat *and* salt in the water film. It is not trivial to generalize the existing theories to include the effect of salt. The temperature at the ice-water interface is presumably equal to the freezing point of water, which is depressed by the presence of salt. However, when this boundary condition is imposed, there is no cut-off for small-wavelength disturbances, and the ripple amplification rate diverges as the wavelength approaches zero. Moreover, 'wet' ice growth under supercooled water is subject to the Mullins-Sekerka instability. While our data indicates that a significant fraction of water is trapped in the resulting dendritic ice matrix, no ripple theory [33–39] has considered the heat and salt transport in this "mushy layer" between the ice and the water. Doing so, with physically accurate boundary conditions, may explain our observed effect of ionic impurities on the ripple dynamics.

A complete theory of icicle morphology would incorporate not only ripple formation, but also tip growth and shape. Such a model may answer further questions raised by our experiments, such as under what conditions saline icicles undergo cessation, why there is a positive correlation between their various growth speeds and the feed water salinity,

and why icicles are more likely to develop multiple tips if they grow in still air.

As shown in this thesis, icicle formation is influenced by many physical parameters. Experimentally, more of the parameter space can be explored. In particular, icicles can be grown from an even wider variety of solutions that exhibit different thermodynamic properties. For instance, the freezing kinetics can be changed by using different types of salt. Most of the icicles we made from solutions containing both salt *and* surfactant grew multiple tips early on. Based on the data that could be analyzed, we determined that the surfactant caused the ripples on saline icicles to decay at an earlier time. More experiments should be conducted, possibly on ramps or long cylindrical substrates, to study in more detail the coupled effect of ionic impurities and surface tension. In addition to morphological analysis, measuring the evolving composition of the solid phase of the icicle and its drip-off water will likely reveal further insights into the mechanism of the rippling instability.

Icicles are arguably the simplest natural manifestation of the general phenomenon of 'wet' ice growth, where water from the atmosphere or the sea is delivered by some combination of gravity, wind-driven flow, and spray [69, 70]. Mitigating the hazards of ice build-up on aircrafts, ships, power lines, and other structures is an important branch of engineering [1–3]. Even otherwise innocent icicles amount to unwanted reverse lightning rods if they form on high-voltage equipment [71]. The study of icicles may elucidate some aspects of ice morphology and stability that are relevant to practical ice accretion problems, and vice versa.

Furthermore, there is an intriguing similarity between icicles and stalactites. Like icicles, stalactites are covered with a thin flowing liquid film during their growth, and have been hypothesized to converge to a universal, self-similar shape [28,29]. More remarkably, the shapes of icicles and stalactites are predicted to exhibit the same asymptotic power law [26], even though stalactites are formed by a much different process involving CO_2 dissolution and $CaCO_3$ precipitation. The crenulations on stalactites [32] also bear a close resemblance to the ripples on icicles. Whether there exists some universal mechanism linking these two deceptively simple examples of natural pattern formation remains an interesting open question.

Appendix A

Nomenclature

Table A.1: Physical quantities associated with icicle formation.

	Physical quantity	**Unit**
R	Icicle radius	m
L	Icicle length	m
z	Vertical distance away from the tip	m
h	Thickness of the liquid film	m
δ	Thickness of the air boundary layer	m
R_p	Radius of the pendant drop	m
δ_T	Crystal thickness at the tip	m
a	See Eq. 4.6	m
A	Ripple amplitude	m
λ	Ripple wavelength	m
A_p	Surface area of the pendant drop	m^2
A_w	Surface area of the icicle walls	m^2
M_S	Mass of water supplied	kg
M_I	Mass of icicle	kg
M_D	Mass of water dripped off	kg
T_{LA}	Temperature at the liquid-air interface	K
T_A	Ambient air temperature	K
ΔT_A	$T_{LA} - T_A$	K
T_m	Freezing point of water	K

Continued on next page ...

Table A.1 – continued from previous page

	Physical quantity	**Unit**
ΔT_p	Temperature change in the pendant drop	K
v_g	Growth speed normal to the icicle surface	m/s
v_t	Growth speed of the icicle tip	m/s
v_{rip}	Ripple traveling speed	m/s
W_0	Mass flux of water arriving at the root	kg/s
W_T	Mass flux of water arriving at the tip	kg/s
dM_T/dt	Mass growth rate of ice at the tip	kg/s
dM/dt	Mass growth rate of ice at the walls	kg/s
Q_0	Volumetric flux of water arriving at the root	m^3/s
dV_T/dt	Volumetric growth rate of ice at the tip	m^3/s
dV/dt	Volumetric growth rate of ice at the walls	m^3/s
J	Heat flux	$\mathrm{J}/(\mathrm{m}^2{\cdot}\mathrm{s})$
ρ	R/a	–
ζ	z/a	–
$\mathcal{R}_{\mathcal{M}}$	$(dM_I/dt)/(dM_S/dt)$	–
σ_r	Ripple amplification rate	1/s
k_c	Ripple wavenumber	1/m
S	Salinity of liquid	–
ρ_L	Density of liquid	kg/m^3
ν_L	Kinematic viscosity of liquid	m^2/s
κ_L	Thermal diffusivity of liquid	m^2/s
Λ_L	Thermal conductivity of liquid	$\mathrm{W}/(\mathrm{m}{\cdot}\mathrm{K})$
$\mathcal{M}_L$	Molar mass of liquid	kg/mol
L_f	Latent heat of fusion	J/kg
L_v	Latent heat of vaporization	J/kg
c_L	Specific heat of liquid	$\mathrm{J}/(\mathrm{kg}{\cdot}\mathrm{K})$
ρ_{sat}	Saturated vapour density (pure water)	kg/m^3
ρ_{sat}^S	Saturated vapour density (saline water)	kg/m^3
P	Liquid pressure	N/m^2
u_s	Surface speed of the liquid film	m/s
γ	Surface tension at the liquid-air interface	N/m
D	Diffusivity of salt in the liquid	m^2/s
ρ_A	Density of air	kg/m^3
ν_A	Kinematic viscosity of air	m^2/s

Continued on next page ...

Table A.1 – continued from previous page

	Physical quantity	**Unit**
κ_A	Thermal diffusivity of air	m^2/s
Λ_A	Thermal conductivity of air	W/(m·K)
c_A	Specific heat of air	J/(kg·K)
β_A	Volumetric thermal expansion coefficient of air	K^{-1}
H	Convective heat transfer coefficient	$W/(m^2 \cdot K)$
H_v	Evaporative heat transfer coefficient	W·m/kg
$\mathcal{R}_\mathcal{H}$	Relative humidity	%
P_0	Atmospheric pressure	N/m^2
u_A	Wind speed	m/s
u_p	Peak flow speed in the air boundary layer	m/s
f_L	Liquid fraction of the growing ice surface	–
ρ_I	Density of ice	kg/m^3
$\tilde{\rho}_I$	$f_L\rho_L + (1 - f_L)\rho_I$	kg/m^3
Λ_I	Thermal conductivity of ice	W/(m·K)
g	Acceleration due to gravity	m/s^2
σ_B	Stefan-Boltzmann constant	$W/(m^2 \cdot K^4)$
$\mathcal{R}$	Gas constant	J/(mol·K)

In the table of dimensionless numbers below: L is a characteristic length (in m), H is the convective heat transfer coefficient (in $W/(m^2 \cdot K)$), Λ is the fluid thermal conductivity (in W/(m·K)), g is the gravitational acceleration (in m/s^2), β is the volumetric thermal expansion coefficient (in 1/K), T_s and T_b are the surface and bulk temperatures (in K), ν is the fluid kinematic viscosity (in m^2/s), U is a characteristic speed (in m/s), κ is the fluid thermal diffusivity (in m^2/s), D is the mass diffusion coefficient (in m^2/s), ρ is the fluid density (in kg/m^3), and γ is the fluid surface tension (in N/m).

Table A.2: Dimensionless numbers associated with icicle formation.

	Definition
Nusselt number	$\mathrm{Nu} = LH/\Lambda$
Grashof number	$\mathrm{Gr} = g\beta(T_s - T_b)L^3/\nu^2$
Reynolds number	$\mathrm{Re} = LU/\nu$
Prandtl number	$\mathrm{Pr} = \nu/\kappa$
Péclet number for heat transport	$\mathrm{Pe}_h = LU/\kappa$
Péclet number for mass transport	$\mathrm{Pe}_m = LU/D$
Weber number	$\mathrm{We} = \rho LU^2/\gamma$

Appendix B

Contributions

The following peer-reviewed publications are based on the content in this thesis:

- A. S. Chen and S. W. Morris. Experiments on the morphology of icicles. *Phys. Rev. E*, 83(026307), 2011.
- A. S. Chen and S. W. Morris. On the origin and evolution of icicle ripples. *New J. Phys.*, 15(103012), 2013.

I have also presented parts of this work at the following conferences:

- GRC on oscillations and dynamic instabilities in chemical systems, 2008 (poster)
- Dynamics days US, 2009 (talk)
- GRC on nonlinear science, 2009 (poster)
- AGU Fall meeting, 2009 (poster)
- CAP congress, 2010 (talk)
- Nonlinear dynamics and fluid instabilities in the 21st century, 2011 (poster)
- APS DFD meeting, 2011 (talk)
- CAP congress, 2012 (talk)
- Dynamics days US, 2013 (talk)
- Flows and patterns conference, 2013 (poster)

References

[1] G. Poots. *Ice and Snow Accretion on Structures*. Research Studies Press, 1996.

[2] M. Farzaneh (ed.). *Atmospheric Icing of Power Networks*. Springer, 2008.

[3] R. W. Gent, N. P. Dart, and J. T. Cansdale. Aircraft icing. *Phil. Trans. R. Soc. A*, 358(1776):2873–2911, 2000.

[4] F. P. Incropera, D. P. DeWitt, T. L. Bergman, A. S. Lavine. *Introduction to Heat Transfer*. Wiley, 2007.

[5] G. S. H. Lock. *The Growth and Decay of Ice*. Cambridge, 1990.

[6] S. H. Davis. *Theory of Solidification*. Cambridge, 2001.

[7] G. K. Batchelor, H. K. Moffat, and M. G. Worster (ed.). *Perspectives in Fluid Mechanics*. Cambridge, 2002.

[8] D. J. Acheson. *Elementary Fluid Dynamics*. Oxford, 1990.

[9] H. Hatakeyama and S. Nemoto. A note on the formation of horizontal stripes on icicles. *Geophys. Mag.*, 28:479–484, 1958.

[10] R. A. Laudise and R. L. Barns. Are icicles single crystals? *J. Cryst. Growth*, 46:379–386, 1979.

[11] C. A. Knight. Icicles as crystallization phenomena. *J. Cryst. Growth*, 49:193–198, 1980.

[12] I. W. Geer. The not-so-ordinary icicle. *Weatherwise*, 34(6):257–259, 1981.

[13] N. Maeno and T. Takahashi. Studies on icicles I: general aspects of the structure and growth of an icicle. *Low Temp. Sci. Ser. A*, 43:125–138, 1984.

[14] L. Makkonen. A model of icicle growth. *J. Glaciol.*, 34(116):64–70, 1988.

[15] J. Walker. Icicles ensheathe a number of puzzles: just how does the water freeze? *Sci. Am.*, 258:114–117, 1988.

[16] K. K. Chung and E. P. Lozowski. On the growth of marine icicles. *Atmosphere-Ocean*, 28(4):393–408, 1990.

[17] N. Maeno, L. Makkonen, K. Nishimura, K. Kosugi, and T. Takahashi. Growth rates of icicles. *J. Glaciol.*, 40(135):319–326, 1994.

[18] J. A. Neufeld, R. E. Goldstein, and M. G. Worster. On the mechanisms of icicle evolution. *J. Fluid Mech.*, 647:287–308, 2010.

[19] F. Leydolt. Beiträge zur kenntniss der krystallform und der bildungsart des eises. *Sitzungsberichte*, 7:477–487, 1851.

[20] A. Bertin. Sur la structure optique de la glace. *Annales de chimie et de physique*, 5(13):283–288, 1878.

[21] J. McConnel and D. Kidd. On the plasticity of glacier and other ice. *Proc. Roy. Soc. London*, 44:331–367, 1888.

[22] H. Hess. *Die gletscher*. Braunschweig, 1904.

[23] U. Yoshida and S. Tsuboi. Examination of ice-crystals by x-rays. *Mem. Coll. Sci. Kyoto Imp. Univ. Ser. A*, 12:203–207, 1929.

[24] N. E. Dorsey. *Properties of Ordinary Water-Substance*. Reinhold, 1940.

[25] K. Szilder and E. P. Lozowski. An analytical model of icicle growth. *Ann. Glaciol.*, 19:141–145, 1994.

[26] M. B. Short, J. C. Baygents, and R. E. Goldstein. A free-boundary theory for the shape of the ideal dripping icicle. *Phys. Fluids*, 18(083101), 2006.

[27] K. Johnson and E. P. Lozowski. The simulation of experimental freshwater icicle growth with a simple numerical model. In *IAHR Proceedings of the 9th International Symposium on Ice*, pages 393–408, Sapporo, Japan, August 1988.

[28] M. B. Short, J. C. Baygents, J. W. Beck, D. A. Stone, R. S. Toomey III, and R. E. Goldstein. Stalactite growth as a free-boundary problem: a geometric law and its platonic ideal. *Phys. Rev. Lett.*, 94(018501), 2005.

[29] M. B. Short, J. C. Baygents, and R. E. Goldstein. Stalactite growth as a free-boundary problem. *Phys. Fluids*, 17(083101), 2005.

[30] N. Maeno and T. Takahashi. Studies on icicles II: wave-forms, spikes and bent icicles. *Low Temp. Sci. Ser. A*, 43:139–147, 1984.

[31] N. Maeno, L. Makkonen, and T. Takahashi. Bent icicles and spikes. *Ann. Glaciol.*, 19:138–140, 1994.

[32] C. Camporeale and L. Ridolfi. Hydrodynamic-driven stability analysis of morphological patterns on stalactites and implications for cave paleoflow reconstructions. *Phys. Rev. Lett.*, 108(238501), 2012.

[33] N. Ogawa and Y. Furukawa. Surface instability of icicles. *Phys. Rev. E*, 66(041202), 2002.

[34] K. Ueno. Pattern formation in crystal growth under parabolic shear flow. *Phys. Rev. E*, 68(021603), 2003.

[35] K. Ueno. Pattern formation in crystal growth under parabolic shear flow II. *Phys. Rev. E*, 69(051604), 2004.

[36] K. Ueno. Characteristics of the wavelength of ripples on icicles. *Phys. Fluids*, 19(093602), 2007.

[37] K. Ueno and M. Farzaneh. Morphological instability of the solid-liquid interface in crystal growth under supercooled liquid film flow and natural convection airflow. *Phys. Fluids*, 22(017102), 2010.

[38] K. Ueno, M. Farzaneh, S. Yamaguchi, and H. Tsuji. Numerical and experimental verification of a theoretical model of ripple formation in ice growth under supercooled water film flow. *Fluid Dyn. Res.*, 42(025508), 2010.

[39] K. Ueno and M. Farzaneh. Linear stability analysis of ice growth under supercooled water film driven by a laminar airflow. *Phys. Fluids*, 23(042103), 2011.

[40] S. Matsuda. Experimental study on the wavy pattern of icicle's surface. Master's thesis, Hokkaido University, 1997.

[41] ASTM International. Standard Specification for Reagent Water (D1193-06). `http://www.astm.org/Standards/D1193.htm`, 2011.

[42] J. Goodwin. *Colloids and Interfaces with Surfactants and Polymers*. Wiley, 2009.

[43] J. G. Göbel and G. R. Joppien. Dynamic interfacial tensions of aqueous Triton X-100 solutions in contact with air, cyclohexane, n-heptane, and n-hexadecane. *J. Colloid Interface Sci.*, 191:30–37, 1997.

[44] S. Phongikaroon, R. Hoffmaster, K. P. Judd, G. B. Smith, and R. A. Handler. Effect of temperature on the surface tension of soluble and insoluble surfactants of hydrodynamical importance. *J. Chem. Eng. Data*, 50:1602–1607, 2005.

[45] The Dow Chemical Company. Dow Perf Materials & Basic Chem Answer Center: Triton X-100 Surfactant Surface Tension. `https://dow-answer.custhelp.com/app/answers/detail/a_id/1666/~/triton-xp100-surfactant-surface-tension`, 2009.

[46] M. H. Sharqawy, J. H. Lienhard V, and S. M. Zubair. Thermophysical properties of seawater: a review of existing correlations and data. *Desalin. Water Treat.*, 16:354–380, 2010.

[47] L. Makkonen. Salinity and growth rate of ice formed by sea spray. *Cold Reg. Sci. Technol.*, 14:163–171, 1987.

[48] L. Makkonen. Solid fraction in dendritic solidification of a liquid. *Appl. Phys. Lett.*, 96(091910), 2010.

[49] E. M. Sparrow and A. J. Stretton. Natural convection from variously oriented cubes and from other bodies of unity aspect ratio. *Int. J. Heat Mass Transfer*, 28(4):741–752, 1985.

[50] H. Schlichting and K. Gersten. *Boundary Layer Theory*. Springer, 2000.

[51] J. G. Knudsen and D. L. Katz. *Fluid Dynamics and Heat Transfer*. McGraw-Hill, 1958.

[52] W. B. Hillig and D. Turnbull. Theory of crystal growth in undercooled pure liquids. *J. Chem. Phys.*, 24(4):914, 1956.

[53] J. S. Wettlaufer, M. G. Worster, and H. E. Huppert. Natural convection during solidification of an alloy from above with application to the evolution of sea ice. *J. Fluid Mech.*, 304:291–316, 1997.

[54] H. Kaplan. *Practical Applications of Infrared Thermal Sensing and Imaging Equipment*. SPIE, 2007.

[55] R. D. Knight. *Physics for Scientists and Engineers*. Pearson, 2004.

[56] C. B. P. Finn. *Thermal Physics*. Chapman & Hall, 1993.

[57] P. Ball. *The Self-Made Tapestry: Pattern Formation in Nature*. Oxford, 1999.

[58] M. C. Cross and P. C. Hohenberg. Pattern formation outside of equilibrium. *Rev. Mod. Phys.*, 65(3):851–1112, 1993.

[59] M. Cross and H. Greenside. *Pattern Formation and Dynamics in Nonequilibrium Systems*. Cambridge, 2009.

[60] R. Hoyle. *Pattern Formation: An Introduction to Methods*. Cambridge, 2006.

[61] W. W. Mullins and R. F. Sekerka. Morphological stability of a particle growing by diffusion or heat flow. *J. Appl. Phys.*, 34(2):323–329, 1963.

[62] J. S. Langer. Instabilities and pattern formation in crystal growth. *Rev. Mod. Phys.*, 52(1):1–28, 1980.

[63] R. Riquelme, I. Lira, C. Pérez-López, J. A. Rayas, and R. Rodríguez-Vera. Interferometric measurement of a diffusion coefficient: comparison of two methods and uncertainty analysis. *J. Phys. D: Appl. Phys.*, 40:2769–2776, 2007.

[64] D. L. Feltham and M. G. Worster. Flow-induced morphological instability of a mushy layer. *J. Fluid Mech.*, 391:337–357, 1999.

[65] J. A. Neufeld and J. S. Wettlaufer. Shear-enhanced convection in a mushy layer. *J. Fluid Mech.*, 612:339–361, 2008.

[66] J. A. Neufeld and J. S. Wettlaufer. An experimental study of shear-enhanced convection in a mushy layer. *J. Fluid Mech.*, 612:363–385, 2008.

[67] J. G. Dash, A. W. Rempel, and J. S. Wettlaufer. The physics of premelted ice and its geophysical consequences. *Rev. Mod. Phys.*, 78:695–741, 2006.

[68] J. S. Wettlaufer and M. G. Worster. Premelting dynamics. *Annu. Rev. Fluid Mech.*, 38:427–452, 2006.

[69] L. Makkonen. Models for the growth of rime, glaze, icicles and wet snow on structures. *Phil. Trans. R. Soc. A*, 358:2913–2939, 2000.

[70] E. P. Lozowski, K. Szilder, and L. Makkonen. Computer simulation of marine ice accretion. *Phil. Trans. R. Soc. A*, 358:2811–2845, 2000.

[71] I. Fofana, M. Farzaneh, H. Hemmatjou, and C. Volat. Study of discharge in air from the tip of an icicle. *IEEE Trans. Dielectr. Electr. Insul.*, 15(3):730–740, 2008.